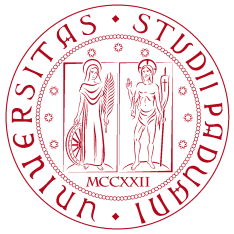

UNIVERSITÀ
DEGLI STUDI
DI PADOVA

UNIVERSITY OF PADOVA

DEPARTMENT OF INFORMATION ENGINEERING

Ph.D. Course in Information Engineering
Information and Communication Science and Technologies Curriculum
XXXVI series

Next Generation Multiple Access Techniques for Wireless Communications

Ph.D. Candidate
Alberto Rech

Ph.D. Supervisor
Professor Stefano Tomasin

Ph.D. Co-Supervisor
Professor Lorenzo Vangelista

Ph.D. Coordinator
Professor Fabio Vandin

Academic Year
2022–2023

With deep gratitude to everyone who supported me technically and emotionally during this challenging journey.

Abstract

The wireless networks evolution is marked by diverse and complex use cases. Key categories like massive machine-type communications (mMTC) and ultra-reliable low-latency communications (URLLC) present unique challenges in the internet-of-things (IoT) ecosystem. Concurrently, enhanced mobile broadband (eMBB) applications demand high data rates, especially in densely populated areas. These varying requirements underscore the need for specialized multiple access schemes tailored to each use case. The thesis explores various approaches to address these challenges. Firstly, two uplink orthogonal multiple access (OMA) solutions are discussed. A semi-grant-free scheme wherein the scheduling is optimized based on the partial knowledge of the user activation is proposed. Then, the study extends to correlated packet generations, developing a distributed learning-based scheduler, which outperforms existing state-of-the-art correlation-based schemes in scenarios with moderate traffic correlation and intensity. Secondly, for downlink OMA, the thesis considers a millimeter wave scenario wherein an intelligent reflecting surface (IRS) with practical (re)configuration constraints is used to mitigate the strong channel attenuation. Heuristic scheduling techniques for downlink time-division multiple-access (TDMA) and orthogonal frequency-division multiple access (OFDMA) are proposed and their performance is deeply discussed. Finally, the last part of the thesis focuses on non-orthogonal multiple access (NOMA) within the context of unsourced random access (URA). Novel tensor-based approaches for random access are presented, showing significant improvements in energy efficiency and fading robustness compared to state-of-the-art URA solutions.

Contents

Listing of acronyms

3GPP 3rd Generation Partnership Project

5G fifth-generation

6G sixth-generation

AI activation information

AMP approximate message passing

AWGN additive white Gaussian noise

B5G beyond-5G

BS base station

CDMA code-division multiple access

CP cyclic prefix

CPD canonical polyadic decomposition

CRA compressive random access

CRC cyclic redundancy check

CS compressed sensing

CSI channel state information

CWC capacity-weighted clustering

DA deterministic assignment

dLoS deterministic line-of-sight

DoF degrees of freedom

DT data transmission

ECCDF empirical complementary cumulative distribution function

ECDF empirical cumulative distribution function

eMBB enhanced mobile broadband

FDMA frequency division multiple access

FEC forward error correction

FIFO first in-first out

FPGA field programmable gate array

FSA framed slotted-ALOHA

GA genetic algorithm

GB grant-based

GF grant-free

GFEO greedy frame efficiency optimizer

GMAX greedy maximum-rate scheduler

HC hierarchical clustering

HMM hidden Markov model

IAB integrated access and backhaul

ICWC inverse capacity-weighted clustering

IoT internet-of-things

IRS intelligent reflecting surface

KM K-means

KMed K-medoids

LLR log-likelihood ratio

LMMSE linear minimum mean squared error

LoS line-of-sight

LRI linear-reward-inaction

LSFC large-scale fading coefficient

LTE long-term evolution

MAP maximum a posteriori probability

MDP Markov decision process

MIMO multiple input-multiple output

MINLP mixed integer non-linear programming

ML maximum likelihood

MMPC min-max pairwise correlation

mMTC massive machine-type communications

MMV multiple measurement vector

mmWave millimeter wave

MRA massive random access

MRC maximum-ratio combining

MTC machine-type communications

NLoS non-line-of-sight

NOMA non-orthogonal multiple access

NOPICE noisy pilot channel estimation

NR new radio

OFDM orthogonal frequency-division multiplexing

OFDMA orthogonal frequency-division multiple access

OMA orthogonal multiple access

OSCBC one-shot capacity-based clustering

PAM partition around medoids

PDF probability density function

PIA partial information acquisition

PIMA partial-information multiple access

pLoS probabilistic line-of-sight

PO-MDP partially observable-Markov decision process

QAM quadrature amplitude modulation

RB resource block

ReB reservation beacon

RFID radio-frequency identification

RL reinforcement learning

RSMA rate-splitting multiple access

S-GFEO simplified GFEO

SALOHA slotted ALOHA

SB scheduling beacon

SCL successive cancellation list

SCMA sparse-code multiple access

SIC successive interference cancellation

SIMO single input-multiple output

SISO single input-single output

SNR signal-to-noise ratio

SVD singular value decomposition

TBM tensor-based modulation

TBMC tensor-based plus coherent modulation

TDMA time-division multiple-access

THz Terahertz

TTI transmission time interval

UE user equipment

ULA uniform linear array

UMi urban macro-cell

UOSCBC unconstrained OSCBC

UPA uniform planar array

URA unsourced random access

URLLC ultra-reliable low-latency communications

usd unit symbol duration

Notation

- Scalars are denoted by italic lowercase letters;
- Column vectors and matrices are denoted by boldface lowercase and uppercase letters, respectively;
- $[\boldsymbol{A}]_{k\ell}$ denotes the scalar value in the k-th row and ℓ-th column of matrix $\boldsymbol{A}$, while $[\boldsymbol{a}]_k$ denotes the k-th element of vector $\boldsymbol{a}$;
- Sets are denoted by calligraphic uppercase letters, with $|\mathcal{A}|$ denoting the cardinality of set $\mathcal{A}$;
- $\boldsymbol{A}^{\mathrm{T}}$, $\boldsymbol{A}^{\dagger}$, and $\boldsymbol{A}^{\ddagger}$ denote the transpose, the conjugate transpose, and the conjugate of matrix $\boldsymbol{A}$, respectively;
- $\boldsymbol{a} = \mathrm{vec}(\boldsymbol{A})$ denotes the vectorization operation, stacking the columns of matrix $\boldsymbol{A}$ into the column vector $\boldsymbol{a}$;
- $\mathrm{diag}(\boldsymbol{a})$ denotes the matrix in which entries in the main diagonal are the elements of vector $\boldsymbol{a}$;
- The operators $\otimes$ and $\diamond$ denote the Kronecker and the Khatri-Rao products, respectively;
- $\mathbb{P}(\cdot)$ and $\mathbb{E}[\cdot]$ denote the probability operator and the statistical expectation, respectively;
- $\lceil \cdot \rceil$ and $\lfloor \cdot \rfloor$ denotes the ceiling and floor operators, respectively;
- $\log(\cdot)$ indicates the natural logarithm function;
- $a \bmod b$ denotes the modulo operation, which returns the remainder of a/b;
- $\binom{a}{b}$ denotes the binomial coefficient;
- The imaginary unit is denoted as $j = \sqrt{-1}$;
- $|a|$ and $\angle a$ denote the modulo and phase of the complex scalar a, respectively;
- The squared norm of vector a is denoted as $||\boldsymbol{a}||^2 = \sum_k [a]_k^2$

1 Introduction

The evolution of mobile networks, particularly the transition from fifth-generation (5G) to beyond-5G (B5G), is marked by diverse and increasingly complex use cases. Recent well-established scenarios include enhanced mobile broadband (eMBB) and machine-type communications (MTC), each with distinct requirements for throughput, latency, and reliability [1]. The shift in focus from human-centric to machine-centric communication, in particular in industry, agritech, and smart buildings, necessitates novel technological solutions. Among these, the massive machine-type communications (mMTC) and ultra-reliable low-latency communications (URLLC) categories, part of the broader internet-of-things (IoT), stand out for their unique challenges: URLLC target ultra-low latency and high reliability for critical applications, while mMTC aim to support a high density of devices in scenarios like industrial IoT. Concurrently, traditional eMBB applications such as high-definition video streaming and augmented reality demand significantly high data rates, especially in densely populated areas. These varying requirements underscore the need for specialized multiple access schemes tailored to each use case.

In the early generations of cellular networks, orthogonal multiple access (OMA) methods like frequency division multiple access (FDMA) and time-division multiple-access (TDMA) were prevalent. FDMA divided the frequency spectrum into separate channels for individual users, while TDMA allocated distinct time slots to each user. The introduction of code-division multiple access (CDMA) marked a significant shift, using unique codes for channel sharing and enabling a more flexible and efficient use of the spectrum [2]. This trend continued with long-term evolution (LTE)'s adoption of orthogonal frequency-division multiple access (OFDMA) [3], [4], which combined time with frequency multi-

plexing and optimized resource allocation. The success of OFDMA, characterized by its balance between flexibility, bandwidth, and receiver complexity, led to its incorporation into 5G networks.

With the advent of B5G networks, there is a significant shift in the design philosophy. For example, the use of the millimeter wave (mmWave) band for cellular communications has been included in the latest releases of the 3rd Generation Partnership Project (3GPP) standard. However, the challenging propagation conditions at high frequencies necessitate the design of multiple input-multiple output (MIMO) transceivers, combined with active or passive relays to enhance coverage. Owing to the inherent complexity of transceiver design, current research primarily focuses on downlink transmissions, due to the space limitations for antennas on the user side and restrictions on transmitting power. Nonetheless, active or passive relaying is essential to overcome the substantial path loss encountered at high frequencies. Among the various proposed solutions, intelligent reflecting surfaces (IRSs) are being widely investigated to address the harsh propagation conditions in a cost- and energy-efficient manner. IRSs can passively tune the phase shift of impinging signals to reflect them favorably towards the intended destination, thus acting as a multi-antenna relay to improve signal quality without active (power-consuming) amplification [5]. However, for downlink multiple access, the technical constraints of current IRS prototypes [6] limit performance, as the IRS configurations must be fixed for subsets of users and cannot be dynamically changed for each different transmission.

Instead, for the uplink multiple access, the rise of new scenarios as mMTC poses new challenges in the management of a massive number of uplink connections with varying requirements for latency and throughput. Many OMA schemes optimizing the user scheduling based on the traffic pattern prediction [7] have recently emerged. Such solutions are particularly useful when users' activations are highly correlated. This may occur as a result of correlated underlying traffic generation [8], [9]: for example, wireless-connected thermometers placed on different parts of the same object or nearby objects may sense a temperature variation at the same time and send signals in the same slot. Also, retransmissions (and the accumulation of further packets in users' buffers) yield correlated transmissions among different users. On one hand, such correlation further increases the chances of collisions; on the other hand, it can be exploited to indirectly coordinate the multiple access [10], [11]. Moreover, in latest works, multiple access procedures based on resource requests and grants have been discussed for MTC. However, the sporadic nature of transmissions by a large number of users that characterizes the above use cases makes these schemes inefficient and pushes for the adoption of a grant-free (GF) or semi-GF solution [12].

On another line of research, non-orthogonal multiple access (NOMA) has also been advocated among the promising approaches to address massive user connectivity [13]–[15]. NOMA can operate in various domains, including power and code, to maximize network capacity. The widely studied power-domain NOMA, leverages the differences in channel strengths among users to maximize the network performance through multi-user detection and successive interference cancellation (SIC) at the receiver. Code-domain NOMA, instead, involves low-complexity multi-user detection schemes and includes methods like sparse-code multiple access (SCMA) and low-density sequence CDMA. NOMA-based GF solutions outperform conventional OMA solutions in many scenarios. An effort has been made to unify and standardize the various NOMA schemes, and their performance gains over their orthogonal counterparts have also been investigated [16], [17]. Recently, NOMA approaches for the unsourced random access (URA) paradigm [18] have emerged to manage a massive number of devices: at any time, a fraction of devices transmit simultaneously using the same channel codebook, i.e., encoding their messages into complex codewords that are known at both the users and the base station (BS). The receiver decodes the arriving messages without knowing the identity of the transmitters (and their respective channel coefficients). Although this approach is very effective in managing a large number of users, good performance can be achieved only for tiny payloads and with highly complex massive MIMO receivers [19], [20]. On the downside, NOMA requires advanced pairing and power allocation techniques, as well as powerful channel coding and interference cancellation mechanisms that only partially mitigate collision effects [15]. Under these conditions, the BS may become prohibitively complex to serve a large number of users. Consequently, the huge appeal of NOMA compared to OMA is mainly relevant for uplink rather than downlink applications. Finally, the authors of [21] recently provided a critical evaluation of multi-user MIMO NOMA, highlighting a simultaneous increase in the receiver complexity and reduction in multiplexing gain compared to conventional multiuser precoding, in both the cases of perfect and imperfect channel state information (CSI). For the above-mentioned reasons, OMA remains attractive in many scenarios.

Thesis Contribution and Organization

In this section, we discuss the thesis contribution for each of the following chapters. Throughout all the thesis, the references to the author's papers are highlighted in bold.

Chapter 2. The chapter presents the contributions of the following papers:

- A. Rech, S. Tomasin, L. Vangelista, and C. Costa, "Partial-information multiple access protocol for orthogonal transmissions," in *Proc. ICUFN*, 2023, pp. 271–276

- A. Rech, S. Tomasin, L. Vangelista, and C. Costa, "Semi-grant-free orthogonal multiple access with partial-information for short packet transmissions," *IEEE Open J. Commun. Soc.*, pp. 1–1, 2023

- A. Rech, S. Tomasin, L. Vangelista, and C. Costa, "Minimum-latency scheduling for partial-information multiple access schemes," in *Proc. IEEE GLOBECOM Wkshps*, 2023. arXiv: 2308.02286

- A. Rech and S. Tomasin, "Coordinated random access for industrial IoT with correlated traffic by reinforcement-learning," in *Proc. IEEE GLOBECOM Wkshps*, 2021, pp. 1–6

We investigate two random access protocols for OMA. Initially, we offer an overview of uplink OMA and introduce the novel partial-information multiple access (PIMA) protocol. This protocol is a semi-GF multiple access scheme tailored for short packet transmission and relies on the knowledge of the number of users with packets ready for transmission. We determine the optimal scheduling in scenarios with i.i.d. activations and evaluate its effectiveness across various users' activation statistics. Additionally, we undertake a theoretical exploration of correlated activations by modeling the protocol as a partially observable-Markov decision process (PO-MDP), utilizing the greedy frame efficiency optimizer (GFEO) algorithm to harness the model's full potential. In the latter part of the chapter, we shift our focus to correlated packet generations, where we develop a distributed learning-based scheduler. Here, each user is conceptualized as a player in a Markov game characterized by incomplete information. By implementing the linear-reward-inaction (LRI) algorithm, we establish pure Nash equilibrium strategies for each player. Numerical analyses reveal that our LRI-based approach surpasses existing state-of-the-art correlation-based OMA schemes in scenarios with moderate traffic correlation and intensity.

Chapter 3. The chapter provides a detailed description of the contribution of the following papers:

- A. Rech, M. Pagin, S. Tomasin, F. Moretto, L. Badia, M. Giordani, J. Gambini, and M. Zorzi, "Downlink TDMA scheduling for IRS-aided communications with block-static constraints," in *Proc. IEEE WCNC*, 2023, pp. 1–6

- A. Rech, L. Badia, S. Tomasin, M. Pagin, M. Giordani, J. Gambini, and M. Zorzi, "Downlink clustering-based scheduling of IRS-assisted communications with reconfiguration constraints," *submitted to IEEE Trans. Wireless Commun.*, 2023. arXiv: 2305.14051

- A. Rech, L. Badia, and S. Tomasin, "Scheduling for downlink OFDMA with IRS reconfiguration constraints," *submitted to IEEE Trans. Veh. Technol.*, 2024. arXiv: 2401.03062

We consider the downlink multiple access in a novel B5G scenario wherein users are served in downlink using an IRS with practical constraints. In particular, the aim is to

maximize the average sum capacity, considering a constrained number of IRS reconfigurations within specific time frames. At first, the simple case of downlink TDMA is investigated. We introduce clustering-based scheduling techniques, grouping users based on key metrics such as distance or achievable rate, thereby ensuring similar optimal IRS configurations within each cluster. The adoption of this strategy marks a significant reduction in the frequency of IRS reconfigurations, thanks to the shared settings among users within the same cluster, providing high-capacity performance with reduced overhead. Then, we extend our investigation to OFDMA downlink scheduling. Here, we formalize the sum rate maximization as an NP-complete generalized multi-knapsack problem. We therefore propose an heuristic solution for the joint IRS configuration and resource allocation. This solution is benchmarked against a more complex genetic algorithm (GA)-based method, demonstrating its practical effectiveness in network scenarios.

Chapter 4. We provide an extended description of the contribution of

- A. Rech, A. Decurninge, and L. G. Ordóñez, "Unsourced random access with tensor-based and coherent modulations," in *Proc. IEEE PIMRC*, 2023, pp. 1–6

Chapter 4 investigates tensor-based modulation (TBM) [20] and tensor-based plus coherent modulation (TBMC) within the context of the URA use case. We begin by examining the current state-of-the-art URA solutions, Then, we discuss advancements in TBM design, incorporating robust forward error correction (FEC), soft-decoding, and SIC techniques, and we introduce the novel TBMC scheme. In the TBMC approach, the users' payloads and channel resources are split into two distinct sub-blocks. One is dedicated to unsourced signal transmissions, which are used for the joint estimation of part of the payload and the users' channel coefficients, while the other focuses on power-domain NOMA signal transmissions, making use of the estimated channels. For the first sub-block, we employ TBM integrated with cutting-edge FEC coding to encode a portion of the message. Subsequently, a NOMA scheme is utilized for the coherent signal transmissions. At the receiver side, we implement SIC strategies to effectively deal with interference. A portion of this chapter analyzes the degrees of freedom (DoF) attainable through both TBM and TBMC under various resource-splitting policies. We also evaluate the energy efficiency of these schemes. Our numerical results indicate that TBMC outperforms TBM in terms of energy efficiency, approaching the achievability bound when the number of active users is moderate. Moreover, when compared to state-of-the-art solutions, TBMC demonstrates superior robustness against large-scale fading effects.

Chapter 5. Lastly, Chapter 5 concludes the thesis. First, the contributions and insights are highlighted; then future works are outlined.

2

Uplink Orthogonal Multiple Access

This part of the thesis discusses the uplink orthogonal multiple access (OMA) for packet transmissions with random user activity. At first, a brief literature review and the common uplink OMA scenario are presented in Section 2.1 and 2.2, respectively. Then, Section 2.3 presents in detail the semi-grant-free (GF) partial-information multiple access (PIMA) protocol proposed in **[22]**–**[24]**, including the performance comparison with other OMA and non-orthogonal multiple access (NOMA) multiple access protocols. Section 2.4 provides a distributed reinforcement learning-based OMA scheme for correlated packet generations **[25]**, wherein the scheduling is optimized based on transmission outcomes. Finally Section 2.5 summarizes the chapter.

2.1 OMA Background

In recent years, grant-based (GB) schemes have been proven to be suitable in internet-of-things (IoT) networks with moderate numbers of users [30]–[32]. A widely adopted solution is multichannel ALOHA, wherein active users choose a preamble from a common pool (codebook) of orthogonal preambles. Then, the base station (BS) can effectively differentiate between multiple users simultaneously accessing the network and schedule the users for data transmission in a second dedicated sub-frame (typically of fixed length). However, such schemes require different preamble lengths based on the number of active users to perform optimally. Indeed, while long preambles support more active users, their entailed communication overhead grows rapidly. Moreover, the use of non-orthogonal preambles has been discussed to reduce overhead in the context of compressive random

access (CRA) [33]–[35]; with CRA the BS resorts to compressed sensing (CS) [36] to identify active users. However, multiple measurements are typically needed to accurately estimate the preambles, therefore requiring either multiple-antenna receivers or multiple transmission steps.

On the other hand, GF approaches typically make better use of the resources by letting users transmit immediately, without waiting for explicit approval from BS. Slotted ALOHA (SALOHA) is the simplest and most widely adopted GF OMA protocol: users transmit at the beginning of the first slot available after packet generation and, when collisions occur, collided packets are retransmitted with random delays (in slots). Collisions are further reduced by framed slotted-ALOHA (FSA), which divides time into frames (each split into slots) wherein users transmit at random: this solution is widely adopted in radio-frequency identification (RFID) systems [37]–[39].

Semi-GF multiple access combines both GB and GF approaches. As for the GB solutions, users compete for resources in a preliminary short sub-frame, then, they may receive a grant to transmit data without contention. Typically, users neither reveal their identity nor the BS deterministically schedules the transmission due to the limited acquired information. This hybrid approach aims at combining the efficiency of GB scheduling with the reduced overhead of GB access. Despite the increasing interest in semi-GF multiple access, the majority of the literature focuses on semi-GF NOMA solutions. For example, [40] and [41] proposed to opportunistically admit GF transmissions of a subset of users on the same resources reserved for GB data transmissions, exploiting the receive power diversity and successive interference cancellation (SIC) for decoding the messages. However, despite the research hype on NOMA, several motivations support the use of OMA. First, the separation of user signals in OMA eliminates multi-user interference, significantly simplifying both transmission scheduling and receiver operations. NOMA indeed requires more sophisticated signal processing techniques to mitigate interference, which may be complex and expensive to deploy. Moreover, OMA is a well-established and relatively simple technique and many wireless networks already have the infrastructure and protocols in place for OMA. In such a context, a transition to NOMA would require significant changes and investments in network architecture and standardization. Therefore OMA remains a valuable choice to ensure compatibility with existing IoT networks and devices. A semi-GF OMA scheme was presented in [42], wherein the BS broadcast the colliding preambles, preventing the data transmissions of the users choosing such preambles.

Other OMA schemes have been proposed for correlated user activity, which is typically due to a correlated underlying traffic generation [8], [9]. Also, re-transmissions (with the consequent accumulation of packets in user queues) introduce a correlation of trans-

missions among users: this further increases collisions, while it can also be exploited to coordinate multiple access. While this correlation inherently heightens the risk of collisions, it also presents an opportunity for indirect coordination in multiple access schemes. Consequently, correlation-based schedulers have recently gained attention as a possible breakthrough for multiple access in machine-type communications (MTC), wherein the users' activations are, in general, correlated, as they exploit the users' activation statistics to reduce collisions and substantially enhance the overall uplink performance. Such schemes typically rely on the knowledge of traffic generation statistics [10], or learn the traffic correlation by tracking successes and collisions [43], or reinforcement learning techniques [44].

2.2 Time-Domain Uplink OMA

We consider the uplink of a multiple access scenario with K single-antenna users transmitting to a common single-antenna BS, under the following assumptions.

- We assume the value of K is known at the BS.
- Perfect time synchronization at the BS is assumed, thus users can transmit signals with specific times of arrival at the BS.
- Time is divided into *frames*, and the part of the frame dedicated to data transmission is split into *slots*, all of the same duration.
- All packets have the same duration of one slot, each user may transmit at most one packet per frame, thus occupying one slot.
- A collision occurs when two or more users transmit in the same slot, and such an event prevents the decoding of all collided packets at the BS.
- We assume that the BS always correctly decodes the received packets in slots without collision and that the channel does not introduce other sources of communication errors.
- Successful transmissions are acknowledged by the BS at the beginning of the following frame, and upon collision, collided users retransmit their packets in the following frame.

Let t denote the frame index, and let $\psi_k(t) = 1$, if a successful transmission of user k occurs at frame t, and $\psi_k(t) = 0$ otherwise. The case $\psi_k(t) = 0$ includes also the event

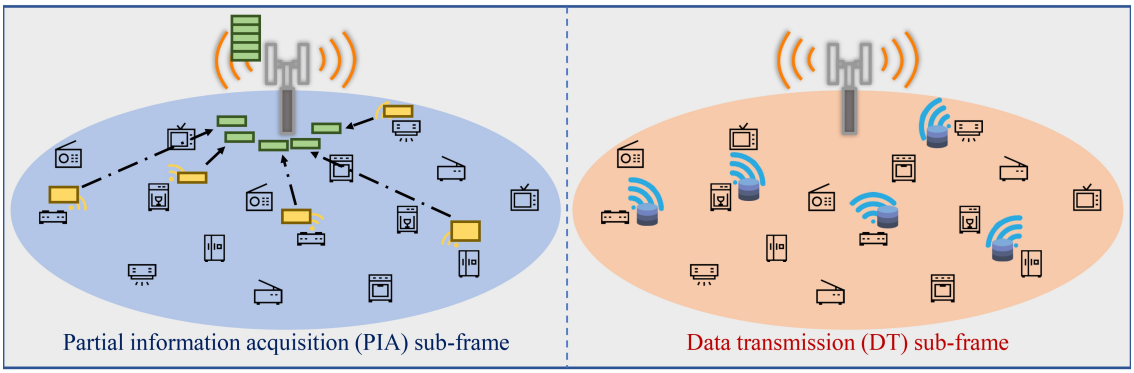

Figure 2.1: PIMA protocol procedure. In the PIA sub-frame, yellow rectangles indicate the signals transmitted by the users for counting, which have different transmission power to compensate for the different channel attenuation. When these signals are received at the BS (green rectangles), they all have the same power, thus, from the total received power, the BS is able to determine the number of active users. In the DT sub-frame, active users transmit their packets.

wherein user k does not transmit at frame t. Successful transmissions are acknowledged by the BS at the end of the current frame. Vector $\boldsymbol{\psi}(t) = [\psi_1(t), \ldots, \psi_K(t)]$ collects values for all the users.

2.3 Partial-Information Multiple Access

In this section, we introduce a new OMA protocol named PIMA. In PIMA, time is organized into frames of *variable length*, each divided into two sub-frames. The first is the partial information acquisition (PIA) subframe, wherein active users (having packets to transmit) transmit an uplink signal, named activation information (AI) to the BS. The BS, using a compute-over-the-air approach [45]–[47], estimates the number of active users. The second sub-frame, named data transmission (DT) sub-frame, is divided into slots, each with a fixed duration of T_{s} seconds. Based on its knowledge on the users activation statistics, the BS firstly allocates an arbitrary number of slots for the entire DT sub-frame, and then assigns one slot in it to each user for the uplink transmission. The allocation is non-exclusive, i.e., a slot is typically given to multiple users, whose transmissions may collide. A PIMA protocol representation with an example of user enumeration procedure is shown in Fig. 2.1.

The PIMA protocol falls into the category of semi-GF multiple access solution. Indeed, without knowledge of the *identity* of active users, collisions could only be avoided using time-division multiple-access (TDMA), which is extremely inefficient for sporadic traffic. We stress that differently from other two-step OMA schemes consisting of preamble and data transmission stages [30], PIMA acquires only partial information on the activation

statistics in the PIA sub-frame, avoiding to reveal the users' identities. Likewise, PIMA cannot be considered a fast uplink grant approach, due to its partial information acquisition at the BS. The main advantage of PIMA with respect to the existing semi-GF solutions is its extremely low overhead (few symbols) required to acquire the partial information and communicate the scheduling, which yields an extremely low latency and complexity.

The main contributions of this section are the following.

1. We introduce the PIMA protocol, detailing the considered frame structure and the basic assumptions on the channel model.

2. We propose two enumeration techniques, based on the channel state information (CSI) available at the users.

3. We consider three different use cases represented by three different packet generation statistics, including independent identically distributed (i.i.d.) activation, b) correlated activation, and c) a bursty traffic generation for massive random access (MRA), wherein the number of users in the system is arbitrarily large while the number of active users remains finite.

4. We prove that, under i.i.d. activation, the allocation of each user to a single slot maximizes the resulting frame efficiency.

5. We prove that the maximum frame efficiency with MRA traffic is obtained by allocating a number of slots equal to the number of active users.

6. Under ideal user enumeration in the PIA subframe, we provide a hidden Markov model-based analysis of PIMA, tracking the users' successful transmissions and failures, and propose the greedy frame efficiency optimizer (GFEO) algorithm.

7. We provide an in-depth numerical evaluation, comparing PIMA also with state-of-the-art preamble-based approaches.

Time organization, Packet Generation, and Buffering

Packets generated in frame t by user k are stored in its buffer and transmitted according to a first in-first out (FIFO) policy. The beginning of frame t, and thus the start of the PIA sub-frame, is triggered by the reservation beacon (ReB), which is transmitted in broadcast by the BS to all users and also contains the acknowledgments of the transmissions occurred at frame $t-1$. The end of the PIA sub-frame and the start of the DT sub-frame is then

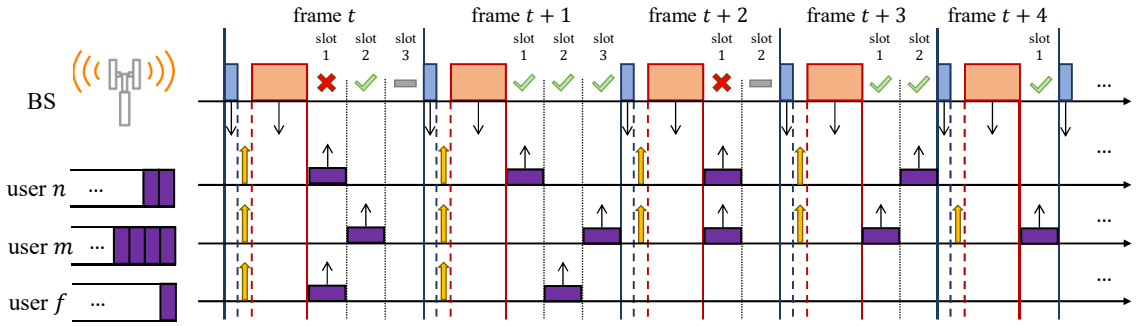

Figure 2.2: Example of the PIMA protocol and its frame structure.

marked by the scheduling beacon (SB), which indicates to each user the slot for packet transmission. An example of PIMA protocol and its frame structure is shown in Fig. 2.2. In this example, users k, m, and f are active at the beginning of frame t, each with a different number of packets to transmit (purple rectangles). The ReB and the SB transmitted by the BS in downlink are represented by the blue and orange rectangles, respectively, while the yellow arrow represents the AI signal for the user enumeration. For drawing simplicity, in this example, no packets are generated after the beginning of frame t. In practice, this may happen at low traffic regime.

In the following, we consider both the case of finite and infinite buffer capacity. In the case of finite-length queues, to ensure data freshness, whenever a new packet is generated at the user k side while its buffer is at full capacity, the oldest packet in its buffer is dropped. Let $Q_k(t)$ be the number of packets in the queue of user k at the beginning of frame t. If $Q_k(t) > 0$, the buffer of user k is non-empty, and k is said to be *active*. Instead, if $Q_k(t) = 0$, its queue is empty and user k is considered *inactive*. The total number of active users at the beginning of frame t is $K_{\mathrm{a}}(t)$.

Activation Statistics

The PIMA scheme has been designed to exploit the sporadic nature of transmissions in the presence of a large number of users. Users can stay dormant for long periods and transmissions are usually triggered by an event or preemptively scheduled. When this happens, users become active with different patterns. To catch the diverse nature of the existing use cases, we analyze the performance of PIMA in three different scenarios, depending on the users' activation statistics.

I.i.d. Activations. User activation times can be described with independent and identically distributed random variables when a) users have a queue for one packet only, and b) all

colliding packets are dropped at the receiver after the first transmission. Such a scenario is typical of monitoring systems requiring frequent updates and data freshness [48] and will be discussed in detail in Section 2.3.3.

Correlated Activations. In this scenario, we assume that queues have infinite lengths. Collided packets at frame t are deterministically queued for retransmission in the following frames. Users' activations are, therefore, generally correlated due to the presence of queues and retransmissions. In this scenario, all queues are assumed to be stable.

For both the i.i.d. and the correlated activation cases, we assume that the traffic generation, also denoted as *packet arrival process*, follows a Poisson distribution with parameter λ (in pkt/s) at each user. The well-known properties of Poisson processes provide a total normalized arrival rate of $\Lambda_T = K\lambda T_{\mathrm{s}}$ (pkt/slot), and when $\Lambda_T = 1$, on average one packet is generated over a slot duration (T_{s}).

Bursty Activations. In this scenario, we assume a bursty traffic model, wherein a finite subset of users is active at the same time, with each user generating a single packet to transmit. Collided packets are retransmitted also in this case, while the buffer capacity is unitary for all users. In particular, we assume that at each burst the number of generated packets follows a Poisson distribution with average Λ_{B} pkt/burst.

2.3.1 The PIMA Protocol

In this section, we provide a detailed description of the proposed PIMA protocol. The PIA sub-frame has a fixed length of L_1 (in slot) and it is used by the BS to estimate the number of currently active users. Based on this information, the BS decides the duration $L_2(t)$ (in slot) of the DT sub-frame and assigns each user to one slot, for uplink data transmission. The total frame duration is

$$L = L_1 + L_2(t) \tag{2.1}$$

A PIMA protocol representation and an example of the frame structure and packet transmissions are reported in Fig. 2.1 and Fig. 2.2, respectively.

Partial Information Acquisition Sub-Frame

At the beginning of frame t, the BS transmits in broadcast the ReB, which triggers the PIA sub-frame and contains the acknowledgments of correctly received packets in the previous frame. ReBs also provide to each user CSI of its channel to the BS. In the following, we will consider both the case of incomplete CSI, wherein the users have an

estimate of the channel gain only, and the case of complete CSI, in which we assume that both channel gains and their phases are estimated at each user.

In the PIA sub-frame the BS obtains the estimate $\hat{K}_{\mathrm{a}}$ of the number of active users K_{a}, as described in detail in Section 2.3.2. The BS, knowing $\hat{K}_{\mathrm{a}}$, schedules the transmissions for the next sub-frame. Let $\boldsymbol{q}(t) = [q_1(t), \ldots, q_K(t)]$ be the *slot selection vector*, collecting the slot indices assigned to each user; then, the length of the DT sub-frame $L_2(t)$ can be derived from $\boldsymbol{q}(t)$ as

$$L_2(t) = \max_k q_k(t). \tag{2.2}$$

Note that, as the BS does not know the identity of the active users, each user in the system is assigned a time slot. Therefore, the length of vector $\boldsymbol{q}(t)$ is always K. To end the PIA sub-frame and trigger the beginning of the following DT sub-frame, the BS transmits the SB, which contains the slot selection vector $\boldsymbol{q}(t)$, encoded as described in Section 2.3.1. The PIA sub-frame duration L_1 accounts for all the symbols transmissions in both uplink and downlink.

To maintain time synchronization, inactive users could a) wake up and wait for the next downlink ReB when generating a packet, or b) always wake up when ReBs and SBs are transmitted (this can be achieved by collecting timing information in the beacons).

SB Overhead. We consider two options for the coding of $\boldsymbol{q}(t)$. The first option provides that all the users in the system receive the explicit indication of the allocated slot in the DT sub-frame. Consider a codebook of K codewords (one per user, each of length $\log_2 K$ bits) representing all possible sorting of user indices, where if a user is in position i_k, its assigned slot is $k = i_k \mod L_2 + 1$. With this codebook, the SB introduces an overhead of

$$R_{\mathrm{SB}} = (K+1)\log_2 K \tag{2.3}$$

bits, since an additional codeword is needed to indicate the length of the DT sub-frame, $L_2(t)$. Note that for a large number of users, this encoding strategy can significantly increase the length of SB, deteriorating the performance of PIMA.

Therefore, we consider a second strategy, wherein all users know a list of random sequences (each of $K\log_2 K$ bits) of length J, indicating the order of user service. In this case, the BS transmit in the SB only the index corresponding to the scheduling sequence and the codeword to indicate $L_2(t)$, providing an overhead of $\log_2 J + \log_2 K$ bits. In the following, we adopt this latter strategy to reduce the SB overhead.

Data Transmission Sub-Frame

In the DT sub-frame, users transmit their packets according to the scheduling set by the BS in the SBs. Note that packets generated by user k during the DT sub-frame are delayed and transmitted in the following frame, to reduce collisions, since the DT frame length is derived only based on the number of users active in the PIA sub-frame. Indeed, data transmissions of users who do not request resources in the PIA subframe would introduce uncertainty in the optimization of $\boldsymbol{q}(t)$, limiting the ability of PIMA to adapt to instantaneous traffic conditions.

Since all the derivations are related to each frame separately, to simplify notation, in the following we drop the frame index t from all the variables.

2.3.2 Estimation of The Number of Active Users

To obtain an estimate of the number of active users at the BS, each active user transmits an AI signal immediately after receiving the ReB. Note that we neglect here the propagation time between BS and the user, which can be easily accounted for by considering a transition (silent) time between the ReB and AI transmissions. The set of users transmitting the AI signals during the PIA sub-frame is

$$\mathcal{K}_{\mathrm{a}} = \{k : Q_k > 0\}, \tag{2.4}$$

with $|\mathcal{K}_{\mathrm{a}}| = K_{\mathrm{a}}$. We stress that the BS does not know the identity of the active users, since the AI signals do not contain such information, to make them shorter.

Given a total system bandwidth W, we assume that each user $k \in \mathcal{K}_{\mathrm{a}}$ transmits $M_1 = WL_1$ symbols $\gamma_{k,\ell}$, $\ell = 1 \ldots, M_1$ during th PIA sub-frame. Assuming perfect synchronization, the ℓ-th received signal at the BS is the superposition of all the symbols transmitted by the users, i.e.,

$$y_\ell = z_\ell + \sum_{k \in \mathcal{K}_{\mathrm{a}}} h_k \gamma_{k,\ell}, \tag{2.5}$$

where h_k is user k complex channel coefficient and z_ℓ is the additive white Gaussian noise (AWGN) term with zero mean and variance σ_z^2. We now propose two different techniques for PIA, under the assumption of incomplete and complete CSI at the transmitter. In both cases, users perform channel estimation with the downlink ReB. However, with incomplete CSI, the users estimate only the channel gain, while the complete CSI case assumes that both channel gains and phases are estimated. Furthermore, we assume that

the acquired CSI (either complete or incomplete) is perfect, i.e., not affected by estimation errors. [1]

PIA With Incomplete CSI

In this section, we consider the case of incomplete CSI at the users, i.e., each user k perfectly estimates its channel gain $g_k = |h_k|$ with the downlink ReB, but not the channel phase. In particular, we assume that each user k transmits M_1 i.i.d. complex Gaussian symbols in the PIA sub-frame with zero mean and variance $1/g_k^2$, therefore the transmit power is such that the signal from each user is received with unitary power at the BS. The BS then measures the total received power and estimates the number of active users. Letting the received samples be $\tilde{\gamma}_\ell$, $\ell = 1, \ldots, M_1$, from (2.5), the estimated total power at the BS is

$$\hat{P} = \frac{1}{M_1} \sum_{\ell=1}^{M_1} \tilde{\gamma}_\ell = \frac{1}{M_1} \sum_{\ell=1}^{M_1} \left| z_\ell + \sum_{k \in \mathcal{K}_\mathrm{a}} h_k \gamma_{k,\ell} \right|^2 . \tag{2.6}$$

Let us indicate the probability density function (PDF) of the received power given that $K_\mathrm{a} = b$ users are active as $p_{\hat{P}|K_\mathrm{a}}(a|b)$, and the probability that $K_\mathrm{a} = b$ users are active as $p_{K_\mathrm{a}}(b)$. The maximum a posteriori probability (MAP) estimate of the number of active users is then

$$\hat{K_\mathrm{a}} = \underset{b}{\mathrm{argmax}} \; p_{\hat{P}|K_\mathrm{a}}(a|b) \, p_{K_\mathrm{a}}(b). \tag{2.7}$$

The value of $\hat{K_\mathrm{a}}$ is obtained from (2.7) by splitting the set of positive real numbers into K properly designed intervals $\mathcal{I}(b) = [\iota_{b-1}, \iota_b]$, $b = 1, \ldots, K$, and finding the region where $\hat{P}$ is falling. Note that the first and last intervals are special, as for the first we have $\mathcal{I}(0) = [0, \iota_0]$, while for the last we have $\mathcal{I}(K) = [\iota_{K-1}, \infty]$. Decision regions have different lengths, thus providing different estimations according to b. Assuming $\gamma_{k,\ell}$ and z_ℓ i.i.d. $\forall t, k, \ell$, as the square modulus of the sum of complex Gaussian random variables is exponentially distributed, $\hat{P}$ follows an Erlang distribution with shape M_1 and rate $1/(K_\mathrm{a} + \sigma_z^2)$. For large values of M_1, $\hat{P}$ can be well approximated as a Gaussian variable with mean $\bar{P}(K_\mathrm{a}) = K_\mathrm{a} + \sigma_z^2$ and variance

$$\sigma_P^2(K_\mathrm{a}) = \frac{[K_\mathrm{a} + \sigma_z^2]^2}{M_1}. \tag{2.8}$$

[1] In practice, time and phase synchronization can be effectively accommodated using orthogonal frequency-division multiplexing (OFDM) with a sufficiently long cyclic prefix (CP). Channel flatness is thereby assured over each subcarrier by properly designed CP, which mitigate the effects of multipath propagation are mitigated. Moreover, even with some degree of synchronization loss, the CP can absorb the delays and ensure proper symbol alignment.

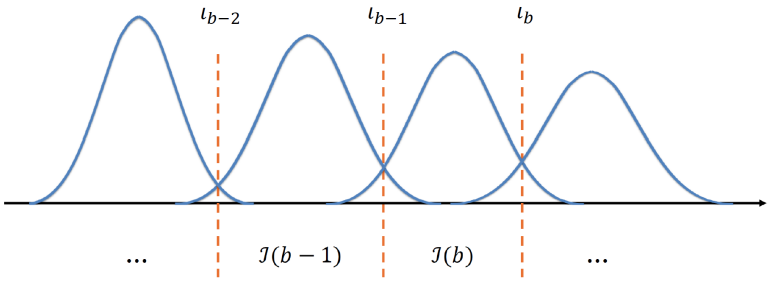

Figure 2.3: Optimal decision regions representation.

As shown in Fig. 2.3, optimal decision regions $\mathcal{I}(b)$, $b = 1, \ldots, K$ are intervals with boundaries at the intersections between the adjacent scaled Gaussian curves; in particular, the boundary ι_b between interval $\mathcal{I}(b)$ and $\mathcal{I}(b+1)$ must solve

$$\frac{p_{K_\mathrm{a}}(b)}{\sigma_P(b)\sqrt{2\pi}} e^{-\frac{(\iota_b - \bar{P}(b))^2}{\sigma_P^2(b)}} = \frac{p_{K_\mathrm{a}}(b+1)}{\sigma_P(b+1)\sqrt{2\pi}} e^{-\frac{(\iota_b - \bar{P}(b+1))^2}{\sigma_P^2(b+1)}}. \tag{2.9}$$

Equation (2.9) is equivalent to the quadratic equation $A\iota_b^2 + B\iota_b + C = 0$, with

$$\begin{aligned} A &= \frac{1}{\sigma_P^2(b+1)} - \frac{1}{\sigma_P^2(b)}, \\ B &= \frac{2\bar{P}(b)}{\sigma_P^2(b)} - \frac{2\bar{P}(b+1)}{\sigma_P^2(b+1)}, \\ C &= \frac{\bar{P}(b+1)^2}{\sigma_P^2(b+1)} - \frac{\bar{P}(b)^2}{\sigma_P^2(b)} - \log\left(\frac{p_{K_\mathrm{a}}(b+1)\sigma_P(b)}{p_{K_\mathrm{a}}(b)\sigma_P(b+1)}\right). \end{aligned} \tag{2.10}$$

Finally, $\hat{K}_\mathrm{a}$ is derived by choosing, among the solutions of the quadratic equation, the one falling between $\bar{P}(b)$ and $\bar{P}(b+1)$.

Estimation Error Probability. We define the average error probability

$$\bar{p}_\mathrm{e} = \mathbb{E}[K_\mathrm{a} \neq \hat{K}_\mathrm{a}] = \sum_b p_\mathrm{e}(b) p_{K_\mathrm{a}}(b), \tag{2.11}$$

where $p_\mathrm{e}(b) = \mathbb{P}[\hat{K}_\mathrm{a} \neq b | K_\mathrm{a} = b]$. Then, under the i.i.d. assumption on $\gamma_{k,\ell}$, the condi-

tional error probability in the enumeration process is

$$\begin{aligned} p_{\mathrm{e}}(b) &= \mathbb{P}[\hat{P} \notin \mathcal{I}(b) | K_{\mathrm{a}} = b] \\ &= \mathrm{Q}\left(\sqrt{M_1}\frac{\iota_b - b + \sigma_z^2}{(b+\sigma_z^2)}\right) + \mathrm{Q}\left(\sqrt{M_1}\frac{-(\iota_{b-1} - b + \sigma_z^2)}{(b+\sigma_z^2)}\right), \end{aligned} \tag{2.12}$$

where $\mathrm{Q}(\cdot)$ is the tail distribution function of the standard normal distribution. For $b = 0$ and $b = K$, the first and second terms in (2.12) are zero, respectively.

To minimize L_1, we should derive the minimum M_1 that guarantees the achievement of a target p_{e}. However, the computation of the optimal decision regions from (2.7) is in general quite complex, due to its dependency on $p_{K_{\mathrm{a}}}(b)$, which in turn depends on the duration of the previous frame(s), as well as on the previous transmission outcomes, therefore being time-variant and strictly dependent on the traffic generation statistics. In the following, for simplicity, we assume that the BS only knows the number of active users and performs the time resource scheduling conditioned on this partial information.

From a practical perspective, since M_1 is a design parameter, it should be time-invariant and should not depend on the user activation statistics. Hence, by defining $\bar{P}(K_{\mathrm{a}}) = K_{\mathrm{a}} + \sigma_z^2$ and choosing $\iota_b = \bar{P}(b) + \frac{1}{2}$, $\forall b$ we approximate (2.12) as

$$p_{\mathrm{e}}(b) \approx 2\mathrm{Q}\left(\frac{\sqrt{M_1}}{2(b+\sigma_z^2)}\right). \tag{2.13}$$

As $\mathrm{Q}(\cdot)$ is a monotonically decreasing function, the maximum estimation error probability is achieved if all users are active in the frame. Then, we derive M_1 in this worst-case scenario, which provides a target error probability $\tilde{p}_{\mathrm{e}} = p_{\mathrm{e}}(K)$, as

$$M_1 = \left[2(K+\sigma_z^2)\mathrm{Q}^{-1}\left(\frac{\tilde{p}_{\mathrm{e}}}{2}\right)\right]^2. \tag{2.14}$$

A major drawback of the PIA design for the incomplete CSI case is that the PIA subframe introduced a significant overhead, as users must transmit a long random sequence to let the BS estimate the total received power, which provided information on the number of active users.

PIA With Complete CSI

In this section, we consider the case of complete CSI at the users, i.e, each user perfectly estimates its channel with the downlink ReB. Assuming perfect phase synchronization, $M_1 = 1$ is sufficient to accurately measure the received power at the BS, therefore we con-

sider that each user then transmits a single symbol γ_k in the PIA sub-frame. Assuming that perfect CSI is obtained by users through the ReB downlink transmission, each user k perfectly inverts the channel, setting $\gamma_k = 1/h_k$. From (2.5), the BS receives

$$y = K_{\mathrm{a}} + z, \tag{2.15}$$

where the symbol index ℓ is omitted for simplicity. Note that in low-signal-to-noise ratio (SNR) scenarios, the AI signal may last several symbols, all with the same structure, and the BS will first average the received samples (obtaining (2.15) but with less noise) and then proceed with the estimate of the number of active users.

The MAP estimate of the number of active users is then

$$\hat{K_{\mathrm{a}}} = \underset{b}{\operatorname{argmax}}\ p_{y|K_{\mathrm{a}}}(y|b)\, p_{K_{\mathrm{a}}}(b), \tag{2.16}$$

where, for the AWGN channel, the PDF of the received signal conditioned to the number of active users is

$$p_{y|K_{\mathrm{a}}}(y|b) = \frac{1}{\sqrt{2\pi\sigma_z^2}} e^{-\frac{|y-b|^2}{\sigma_z^2}}. \tag{2.17}$$

This criterion establishes decision regions on the received signal. Define δ_b as the distance from b (the value obtained without noise) and the region associated with the decision $b+1$. Then, when y falls in the region $[b-\delta_b, b+1-\delta_{b+1}]$, the decision on the number of active devices is b. Since the distance between b and $b+1$ is 1, we have that the distance from b (the value obtained without noise) and the region associated with the decision $b+1$ is $1-\delta_{b+1}$. According to the MAP criterion (2.16), the optimal regions satisfy the following equation

$$p_{b|K_{\mathrm{a}}}(b+\delta_b|b)p_{K_{\mathrm{a}}}(b) = p_{b+1|K_{\mathrm{a}}}(b+1-(1-\delta_b)|b+1)p_{K_{\mathrm{a}}}(b+1), \tag{2.18}$$

since $\delta_{b+1} = 1-\delta_b$. Replacing (2.17) into (2.18), after some algebraic steps we have

$$\delta_b = \frac{1}{2} + \frac{\sigma_z^2}{2} \ln \frac{p_{K_{\mathrm{a}}}(b)}{p_{K_{\mathrm{a}}}(b+1)}. \tag{2.19}$$

The error probability of the enumeration process is the probability of falling out of the correct decision region, thus, conditioned on the fact that $K_{\mathrm{a}} = b$ users are active, we have

$$p_{\mathrm{e}}(b) = \mathrm{Q}\left(\frac{\delta_b}{\sigma_z/\sqrt{2}}\right) + \mathrm{Q}\left(\frac{1-\delta_{b+1}}{\sigma_z/\sqrt{2}}\right). \tag{2.20}$$

I.i.d. Activations. In the case of i.i.d. activations, the activation process coincides with the packet generation process. Assuming that each user generates packets according to a temporal Poisson process with parameter $\lambda_k = \lambda, \forall k$, we obtain

$$p_{K_\mathrm{a}}(b) = \binom{K}{b} b(1 - e^{-\lambda T_\mathrm{a}})(K - b)e^{-\lambda T_\mathrm{a}}, \tag{2.21}$$

where T_a is the time interval considered for the packet generations and $\binom{K}{b}$ counts for all the possibilities of having exactly b active users. Note that for $K \to \infty$ we have $p_{K_\mathrm{a}}(b) \approx p_{K_\mathrm{a}}(b+1)$, thus $\delta_b \to \frac{1}{2}$ and all regions have the same size. In this asymptotic scenario, the error probability in the enumeration process is

$$p_\mathrm{e}(b) \to 2\mathrm{Q}\left(\frac{1}{\sqrt{2}\sigma_z}\right). \tag{2.22}$$

Note that, in case of *imperfect CSI* [49], the estimated channel at user k is

$$\hat{h}_k = h_k + \epsilon_k, \tag{2.23}$$

where ϵ_k accounts for the estimation error. User k transmit $\gamma_k = 1/\hat{h}_k$, and the received samples becomes, from (2.5),

$$y = K_\mathrm{a} - \sum_{k \in \mathcal{K}_\mathrm{a}} \frac{\epsilon_k}{h_k + \epsilon_k} + z = K_\mathrm{a} + z'. \tag{2.24}$$

Assuming $\epsilon_k \sim \mathcal{CN}(0, \sigma_\epsilon)$ for all k, the terms $\frac{\epsilon_k}{h_k + \epsilon_k}$ follow a complex Gaussian ratio distribution, which has been widely studied in both cases of correlated and independent numerator and denominator (see [50] and [51]).

When either the SNRs is high (by the Gaussian ratio statistics) or k is large (by the central limit theorem), the summation in (2.24) can be approximated as a Gaussian r.v., thus z' is also Gaussian. In these scenarios, the imperfect CSI case is modeled as additional noise, and the analysis of the previous subsection still holds. For other scenarios, numerical methods (including Monte Carlo simulations) should be used to evaluate the error probability in the counting process.

2.3.3 Frame Efficiency-Based Scheduling With I.I.D. Activations

In this section, we propose a time-resource scheduling conditioned on the number of active users estimated in the PIA sub-frame.

In the following discussion on scheduling optimization, we assume perfect user counting

in the PIA sub-frame, i.e., $\hat{K}_\mathrm{a} = K_\mathrm{a}$. However, in practical scenarios, the actual scheduling might be based on an erroneous estimation of the number of active users K_a. This discrepancy can lead to performance degradation. In Section 2.3.6, we will analyze the effects of such erroneous estimations by comparing the ideal case of error-free enumeration with the more realistic scenario of error-prone enumeration. This comparison will help quantify the impact of the inaccuracies in user counting on the scheduling performance.

First, we introduce a performance metric that takes into account both the packet latency and the collision probability, whose optimization aims at finding the right balance between the two. Let $l \in \{1, \dots, L_2\}$ be the slot index in the DT sub-frame. We define the success indicator function in slot l as $c_l = 1$ if a successful transmission occurs in slot l and $c_l = 0$ otherwise. Note that the latter case considers both the collision and non-transmission cases. Then, the *conditional frame efficiency* is defined as the ratio between the number of successes in the frame and the length of the DT sub-frame, i.e.,

$$\eta(K_\mathrm{a}) = \frac{1}{L_2} \sum_{l=1}^{L_2} \mathbb{E}[c_l | K_\mathrm{a}]. \tag{2.25}$$

The adaptive maximization of this metric provides the proper balance between the DT sub-frame length and the successful transmission probability.

At each frame, immediately after the end of the PIA sub-frame, the BS solves the following optimization problem:

$$\max_{\boldsymbol{q}} \eta(K_\mathrm{a}), \tag{2.26a}$$

$$\text{s.t.} \quad q_k \in \{1, \dots, L_2\}. \tag{2.26b}$$

The optimization problem (2.26) is of mixed integer non-linear programming (MINLP), and its solution quickly becomes infeasible with long queues or many users. For these reasons, in the following, we focus on the analysis of the i.i.d. activation scenario, designing the parameters of the PIMA scheduler based on its basic assumptions. Note that, while the i.i.d. activation scenario could substantially differ from the correlated activations one at high traffic, it still represents a good approximation in low traffic conditions, wherein retransmissions due to collisions occur sporadically. Moreover, the analysis under i.i.d. activations is useful when no information is available on the transmission correlation at the BS or when obtaining such information is too expensive.

First, we observe that, since user activations are i.i.d., we only have to determine how many users are assigned to each slot, as any specific assignment satisfying this constraint will yield the same collision probabilities, thus the same expected frame efficiency. Note that in case of decoding failure of multiple packets, the user scheduling should be ran-

domized to avoid the repetition of the same collisions.

To minimize the number of users assigned to the same slot, given a length L_2, we assign to slot l the following number of users

$$u_l = \begin{cases} \left\lceil \frac{K}{L_2} \right\rceil & \text{if} \quad l \leq K \bmod L_2, \\ \left\lfloor \frac{K}{L_2} \right\rfloor & \text{if} \quad l > K \bmod L_2, \end{cases} \tag{2.27}$$

where we possibly schedule one more user in the first $\left\lfloor \frac{K}{L_2} \right\rfloor$ slots to minimize the transmission delay.

With this scheduling policy, the slot success random variable c_l can be rewritten as a function of u_l, as it only depends on the number of users scheduled in slot l. Thus, the optimization problem (2.26) is reduced to the optimization of the DT sub-frame length, L_2, and from (2.25), we have

$$L_2^* = \underset{L_2}{\operatorname{argmax}} \frac{1}{L_2} \sum_{l=1}^{L_2} \mathbb{E}[c_l | K_\mathrm{a}, u_l], \tag{2.28a}$$

$$\text{s.t.} \;\; L_2 \in \mathbb{K}/\{0\}. \tag{2.28b}$$

Now, given K_a, the probability that user k is the one and only active user assigned to slot l is derived by considering all cases of active users, where user k is active and all other users assigned to slot l are, instead, inactive. Consider the matrix $\lceil K/L_2 \rceil \times L_2$, having entry (r, c) equal to one when in slot c only user r (among those assigned to that slot) is active. The number of favorable cases wherein we have a single "1" in column l is given by all the possibilities to place the "1" of the remaining $K_\mathrm{a} - 1$ users in any of the $K - u_l$ entries of the matrix excluding column l. Therefore, the favorable case is given by all the combinations of $K_\mathrm{a} - 1$ objects taken from a set of $K - u_l$ objects. Instead, the total number of cases is given by all the combinations of K_a active users chosen from the K scheduled users. The probability of having a successful transmission in slot l is therefore

$$\mathbb{E}[c_l | K_\mathrm{a}, u_l] = u_l \frac{\binom{K-u_l}{K_\mathrm{a}-1}}{\binom{K}{K_\mathrm{a}}}, \tag{2.29}$$

where factor u_l counts the users assigned to slot l. Note that the numerator of (2.29) counts the number of combinations giving exactly one active user assigned to slot l, while the denominator counts the total number of possible combinations of active users. The probability of collision in slot l is therefore $1 - \mathbb{E}[c_l | K_\mathrm{a}, u_l]$.

Problem (2.28) is a MINLP problem, and its solution strictly depends on the number of users in the system. If the number of active users is comparable with the total number of users K, (2.28) is not solvable by continuous relaxation of L_2, as the rounding functions are not differentiable. However, it is possible to find the optimal frame length L_2^* with complexity $O(\log K)$, using a binary search algorithm, or alternatively using a discrete gradient ascent algorithm. In any case, L_2^* depends only on K_a, thus can be computed offline and then stored in a table. Instead, if $K \to \infty$ and $K_\mathrm{a} << K$ is finite, the following result holds:

Theorem 1. *For $K \to \infty$, under i.i.d. activations, given a finite number of active users K_a, the DT sub-frame length L_2 maximizing frame efficiency is exactly K_a.*

Proof. Since $K \to \infty$ and $1 < K_\mathrm{a} << K$, $u_l = \frac{K}{L_2}$ for all $l = 1, \dots, L_2$. From (2.29) we have

$$\eta(K_\mathrm{a}) = \mathbb{E}\left[c_l \middle| K_\mathrm{a}, \frac{K}{L_2}\right] = \frac{\frac{K}{L_2}\binom{K-\frac{K}{L_2}}{K_\mathrm{a}-1}}{\binom{K}{K_\mathrm{a}}} = \frac{K_\mathrm{a}}{L_2}\frac{(K-\frac{K}{L_2})!(K-K_\mathrm{a})!}{(K-\frac{K}{L_2}-K_\mathrm{a}-1)!(K-1)!}, \tag{2.30}$$

then, using the Stirling factorial approximation $\alpha! = \sqrt{2\pi\alpha}(\frac{\alpha}{e})^\alpha$, whose validity is verified with good accuracy even for small values of α, with some algebraic steps we obtain

$$\begin{aligned}\eta(K_\mathrm{a}) =& \frac{K_\mathrm{a}}{L_2}\overbrace{\sqrt{\frac{K(1-\frac{1}{L_2})(K-K_\mathrm{a})}{[K(1-\frac{1}{L_2})-K_\mathrm{a}+1](K-1)}}}^{\mu(K,K_\mathrm{a},L_2)} \times \\ &\times \underbrace{\frac{[K(1-\frac{1}{L_2})]^{K(1-\frac{1}{L_2})}(K-K_\mathrm{a})^{K-K_\mathrm{a}}}{[K(1-\frac{1}{L_2})-K_\mathrm{a}+1]^{K(1-\frac{1}{L_2})-K_\mathrm{a}+1}(K-1)^{K-1}}}_{\xi(K,K_\mathrm{a},L_2)}.\end{aligned} \tag{2.31}$$

Taking the limit for $K \to \infty$ we have

$$\lim_{K\to\infty} \mu(K, K_\mathrm{a}, L_2) = 1, \tag{2.32a}$$

$$\lim_{K\to\infty} \xi(K, K_\mathrm{a}, L_2) = \left(1 - \frac{1}{L_2}\right)^{K_\mathrm{a}-1}. \tag{2.32b}$$

Therefore the maximum frame efficiency only depends on K_a and L_2, and it is given by

$$\eta(K_\mathrm{a}) = \frac{K_\mathrm{a}}{L_2}\left(1 - \frac{1}{L_2}\right)^{K_\mathrm{a}-1}. \tag{2.33}$$

Its stationary points are derived from the first order derivative with respect to L_2 as

$$\frac{d}{dL_2}\left[\frac{K_\mathrm{a}}{L_2}\left(1-\frac{1}{L_2}\right)^{K_\mathrm{a}-1}\right]=0 \Leftrightarrow L_2=K_\mathrm{a} \vee L_2=1, \tag{2.34}$$

thus, while $L_2=1$ is trivially the global minimum for $K_\mathrm{a}>1$, the frame efficiency is maximized for $L_2=K_\mathrm{a}$. □

On the Optimality of the Single Slot Allocation. In PIMA, we have assumed that each user k is assigned to a single slot q_k in the frame. However, we may wonder if this scheduling policy is optimal or if it is preferable to assign multiple slots to each user. Focusing on the case of i.i.d. activations, we have the following result.

Theorem 2. *Under i.i.d. activations, the assignment of a single slot to each user in the DT sub-frame is optimal, i.e., it maximizes the expected frame efficiency.*

Proof. Since the collision probability is the same for all users and depends only on the number of other users transmitting in the same slot, by allocating more slots to each user, we increase the collision probability. Hence, single-slot scheduling is optimal in this case. □

2.3.4 PIMA Protocol Analysis for Correlated Activations

In the previous sections, we considered the PIMA design under the assumption of i.i.d. user activations. However, in the correlated activations scenario, the activation statistics knowledge can be exploited to improve the scheduling performance [43]. In this section, we propose a Markov model-based analysis of PIMA, formalizing the case of correlated activations. In particular, we model PIMA as a partially observable-Markov decision process (PO-MDP) problem, which is solved by the Bellman equation [52], [53]. Then, to address the excessive complexity of the PO-MDP solution, we propose a sub-optimal approach that determines the frame length iteratively, while performing the user scheduling, based on the frame efficiency metric.

In this context, the time index gains relevance, and cannot be omitted in the analysis. In the following, τ denotes a generic time instant, t the frame index, and $\tau_0(t)$ the starting time of frame t. Moreover, for the sake of simplicity, we assume fixed PIA sub-frame length L_1, comprehensive of both the enumeration task and the beacon transmissions, and assume an error-free user enumeration.

PO-MDP. PO-MDP [53] generalize the Markov decision processs (MDPs) by combining such models with the key features of hidden Markov models (HMMs). An HMM [54] is

defined by a Markov process, which is not directly observable (hidden process), and an observable random quantity depending only on the current state of the process (observation). PO-MDPs add the concepts of actions and penalties associated with the state transition-action couples, which are the fundamental features of MDPs. At each time period, the environment, represented here by the communication system, is in some state i. The agent, which is responsible for interacting with the environment, takes an action, a, which causes the transition to state j with probability $p_{i,j}(a)$. At the same time, the agent receives an observation $\boldsymbol{\beta}$ which depends on the new state of the environment j, and on the just taken action a, with emission probability $e_{\boldsymbol{\beta}} = \mathbb{P}(\boldsymbol{\beta}|a, j)$. Finally, when the system moves from state i to state j due to action a at time t, the agent receives a penalty $P(t) = P(i, j, a)$, where $P(\cdot, \cdot, \cdot)$ is the penalty function. Then, the process is iterated. The goal of the agent, at each time step, aims at minimizing its expected future penalty $\mathbb{E}\left[\sum_{t=0}^{\infty} P(t)\right]$. A discount factor may be also added to balance the impact of immediate and future penalties.

Note that, differently from conventional MDP, wherein the process state is known to the agent, in PO-MDP the agent does not directly observe it, thus its actions are taken under uncertainty of the hidden state. However, by interacting with the environment and receiving observations, the agent may update its *belief* in the hidden state, i.e., the state probability distribution based on the observations. Therefore, as the system evolves and the environment is observed, actions are taken with a more accurate estimation of the current state.

PO-MDP Model for The PIMA Protocol

In the following, we map the PIMA protocol features to each of the discussed components of a PO-MDP. For the following analysis, we assume negligible error probability in the PIA sub-frame, i.e., *perfect knowledge* of the number of active users, thus $\hat{K_{\mathrm{a}}}(t) = K_{\mathrm{a}}(t), \forall t$.

Hidden States. The hidden system state is the set of the arrival time of the packets in the buffers of all users. At time τ, the state is $\boldsymbol{\mathcal{X}}(\tau) = \{x_{k,h}, \forall k, h\}$, where $x_{k,h}$ is the instant of the generation of the h-th packet, for all packets currently in its buffer. The state space of the PO-MDP $\mathcal{Y} = \{\boldsymbol{\mathcal{X}}(\tau),\ \forall \tau\}$ has infinite cardinality, due to the infinite buffer length assumption. The buffer state evolves at each transmission attempt or packet generation, however, only the state probability at the beginning of the DT sub-frame is relevant for scheduling.

Actions. The scheduling vector $\boldsymbol{q}(t)$ is the action performed by the agent BS at frame t based on its belief on the current system state. For simplicity, in the following, we denote

the state at the end of the PIA sub-frame as $\boldsymbol{\mathcal{X}}(t)$.

Observations. Observations are acquired at the end of the PIA sub-frame of frame t as

$$\boldsymbol{\beta}(t) = \{K_{\mathrm{a}}(t), \boldsymbol{\psi}(t-1), \mathcal{C}(t-1)\} \in \mathcal{O}, \tag{2.35}$$

where set $\mathcal{C}(t)$ collects all slots wherein a collision is detected in frame t, and $\mathcal{O}$ is the set of possible observations. Note that acknowledgment and collision vectors are referred to the previous frame, as we are at the beginning of the DT sub-frame of frame t. The cardinality of $\mathcal{O}$ is finite, as only a limited number of combinations of successes, collisions, and number of active users may occur.

Conditional Transition Probabilities. The underlying Markov process evolves from state $\boldsymbol{\mathcal{I}} \in \mathcal{Y}$ at frame $t-1$ to state $\boldsymbol{\mathcal{J}} \in \mathcal{Y}$ at t with posterior conditional *transition probability*

$$p_{\boldsymbol{\mathcal{I}}\boldsymbol{\mathcal{J}}}(\boldsymbol{a}) = \mathbb{P}\left[\boldsymbol{\mathcal{X}}(t) = \boldsymbol{\mathcal{J}} | \boldsymbol{\mathcal{X}}(t-1) = \boldsymbol{\mathcal{I}}, \boldsymbol{q}(t-1) = \boldsymbol{a}\right]. \tag{2.36}$$

We observe that, by imposing the condition on the observations and the previous action, transitions occur only according to the packet generation and transmission processes.

Emission Probabilities. For each state, different observations may be acquired in general. The emission probability of observing $\boldsymbol{\beta}'$ by visiting state $\boldsymbol{\mathcal{J}}$ is defined as

$$e_{\boldsymbol{\beta}'}(\boldsymbol{\mathcal{J}}, \boldsymbol{a}) = \mathbb{P}[\boldsymbol{\beta}(t) = \boldsymbol{\beta}' | \boldsymbol{\mathcal{X}}(t) = \boldsymbol{\mathcal{J}}, \boldsymbol{q}(t) = \boldsymbol{a}]. \tag{2.37}$$

Beliefs. We first observe that the information at the end of the PIA sub-frame of frame t is both the observations and the actions up to that frame, i.e.,

$$\mathcal{E}(t) = \{\boldsymbol{\beta}(t), \boldsymbol{\beta}(t-1), \ldots, \boldsymbol{\beta}(0), \boldsymbol{q}(t-1), \ldots, \boldsymbol{q}(0)\}. \tag{2.38}$$

Now, the belief of state $\boldsymbol{\mathcal{X}}$ is the conditional probability of being in state $\boldsymbol{\mathcal{X}}(t)$ at frame t, given the information available at the BS

$$\rho(\boldsymbol{\mathcal{J}}, t) = \mathbb{P}[\boldsymbol{\mathcal{X}}(t) = \boldsymbol{\mathcal{J}} | \mathcal{E}(t)]. \tag{2.39}$$

The belief is recursively computed by exploiting the conditional independence of the hidden Markov chain, observing that $\mathcal{E}(t) = \{\boldsymbol{\beta}(t), \mathcal{E}(t-1)\}$ and setting the initial system conditions as

$$\rho(\boldsymbol{\mathcal{I}}, 0) = \begin{cases} 1 & \boldsymbol{\mathcal{I}} = \mathbf{0}, \\ 0 & \text{otherwise.} \end{cases} \tag{2.40}$$

The belief at the end of the PIA sub-frame of frame t is computed as

$$\rho(\mathcal{J},t)=e_{\boldsymbol{\beta}}(\mathcal{J},\boldsymbol{a})\sum_{\mathcal{I}:\boldsymbol{\beta}(t)=\boldsymbol{\beta}}p_{\mathcal{I}\mathcal{J}}(\boldsymbol{q}(t-1))\rho(\mathcal{I},t-1). \tag{2.41}$$

Let also $\boldsymbol{\rho}(t)$ be the vector collecting $\rho(\mathcal{J},t)$ for all $\mathcal{J}$.

Penalty. When moving from state $\mathcal{I}$ to state $\mathcal{J}$ with action $\boldsymbol{a}$, the penalty is $P(\mathcal{I},\mathcal{J},\boldsymbol{a})$, where the penalty function depends only on the states and action.

Latency As Penalty Function

As a performance metric, we consider packet latency, which measures the time a packet spends in the buffer before successful transmission. Such time includes the delay introduced by collisions and retransmissions.

In formulas, the *latency* of packet h in user k buffer is defined as

$$D_{k,h}=\tau_{k,h}-x_{k,h}, \tag{2.42}$$

where $\tau_{k,h}$ is the instant of the successful delivery of the packet to the BS. Note that all packets in user k buffer at time $\tau_0(t)$ increase their latency by $L(t)=L_1+L_2(t)$ if they are not successfully transmitted at frame t. Instead, a successful transmission provides an increment of $L_1+q_k(t)$.

We consider the latency increment penalty associated with action $\boldsymbol{q}_t=\boldsymbol{a}$ when in state $\mathcal{I}$ at frame t, defined as

$$P(\mathcal{I},\mathcal{J},\boldsymbol{a})=\sum_{k=1}^{K}\sum_{h=1}^{K_k(\tau_0(t))}d_{k,h}(t), \tag{2.43}$$

where the incremental latency of packet h in user k buffer is

$$d_{k,h}(t)=\begin{cases}L_1+q_k(t-1), & h=1,\ \psi_k(t-1)=1,\\ L(t-1), & \psi_k(t-1)=0,\\ \tau_0(t)-x_{k,h} & \text{otherwise,}\end{cases} \tag{2.44}$$

and we note that from the couple of subsequent states $\mathcal{I},\mathcal{J}$ at frames t and $t+1$ we can compute $\boldsymbol{\psi}(t)$. Since we consider FIFO buffers, $h=1$ refers to the oldest packet in the buffer, which is also the first scheduled for transmission in the buffer.

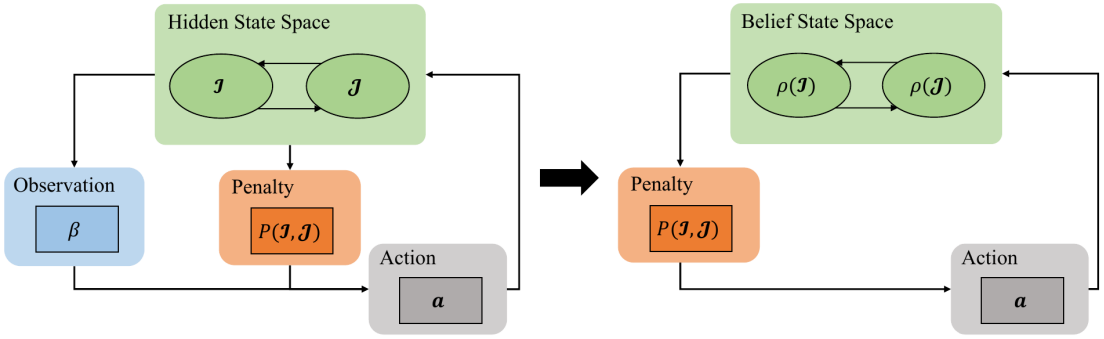

Figure 2.4: Block diagram illustrating the PO-MDP framework on the left and its corresponding belief state space MDP on the right, with simplified notation neglecting the time index t.

PO-MDP Solution

As for conventional MDPs, the solution of the PO-MDP minimizes the expected future penalty $\mathbb{E}\left[\sum_{t=0}^{\infty} P(t)\right]$. Note that, since the agent does not directly observe the environment's state, it must make decisions based on its belief of the current state. For this reason, the PO-MDP is typically formulated as a conventional infinite-states MDP by moving from space $\mathcal{Y}$ to the continuous space of all distributions of the beliefs, thus all possible values of $\rho(\mathcal{J})$, for all $\mathcal{J} \in \mathcal{Y}$. Both the observations and actions are the same as the original PO-MDP, and the *policy* function maps each belief state to an action, $\pi : \boldsymbol{\rho}(t) \rightarrow \boldsymbol{q}(t)$. The block diagram depicting the PO-MDP and its respective MDP in the belief state space is shown in Fig. 2.4. The optimal policy, i.e., the one minimizing the long-term penalty, is the solution of the Bellman equation applied to the belief MDP, as detailed in [52], [55].

2.3.5 Greedy Frame Efficiency Optimizer Algorithm

The direct PO-MDP solution is, in general, very challenging, due to the infinite number of hidden states of the PO-MDP model. Therefore, we consider a sub-optimal solution that determines the frame length $L_2(t)$ iteratively, while performing the user assignments. To this end, we once again resort to the frame efficiency metric (2.25), which can be extended to the correlated activation case exploiting the PO-MDP formulation.

At frame t, immediately after the end of the PIA sub-frame, the BS solves the optimization problem (2.26). However, problem (2.26) is one of MINLP, and its solution quickly becomes for large numbers of users. Therefore, to simplify the analysis, we resort to a greedy scheduling solution.

The proposed algorithm is denoted as GFEO algorithm, and it iteratively adjusts the

frame length $L_2(t)$, while performing the user assignments $\boldsymbol{q}(t)$. First, note that, due to the assumption of buffering packets generated during frame t and single slot assignment to each user, each hidden state/action couple leads to a single possible observation $\boldsymbol{\beta}^*$. Thus, the emission probability is $e_{\boldsymbol{\beta}}(\boldsymbol{\mathcal{J}}, \boldsymbol{a}) = 1$, for $\boldsymbol{\beta} = \boldsymbol{\beta}^*$, and $e_{\boldsymbol{\beta}}(\boldsymbol{\mathcal{J}}, \boldsymbol{a}) = 0$ otherwise. Hence, (2.41) can be rewritten and recursively computed as

$$\rho(\boldsymbol{\mathcal{J}}, t) = \sum_{\boldsymbol{\mathcal{I}}:\boldsymbol{\beta}(t)=\boldsymbol{\beta}^*} p_{\boldsymbol{\mathcal{I}}\boldsymbol{\mathcal{J}}}(\boldsymbol{q}(t-1))\rho(\boldsymbol{\mathcal{I}}, t-1). \tag{2.45}$$

Now, let $\eta(L_2(t), \boldsymbol{q}(t)) = \eta(t)$ be the expected conditional frame efficiency, where we now highlight its dependence on the DT sub-frame length and the user assignment. Let us also introduce the activation probability of user k conditioned to the current belief states, i.e., from (2.45),

$$\phi_k(t) = \sum_{\boldsymbol{\mathcal{I}}:K_k(\tau_0(t))>0} \rho(\boldsymbol{\mathcal{I}}, t). \tag{2.46}$$

Finally suppose, without loss of generality, that users' indices are ordered with decreasing activation probability, i.e.,

$$\phi_1(t) \geq \phi_2(t) \geq \ldots \geq \phi_K(t). \tag{2.47}$$

The GFEO algorithm includes K iterations (one per user), assigning user k to a specific time slot at iteration k. At the first iteration ($k = 1$), user 1 is assigned to the first DT slot of the frame, i.e., $q_1(t) = 1$. The algorithm compares the frame efficiency obtained by assigning the current user to each of the already allocated slots, or to a new slot, thus increasing $L_2(t)$. Then, the best solution among those explored is chosen, and the algorithm moves to the scheduling of the next user. Specifically, at iteration $k \geq 2$, the algorithm computes the conditional frame efficiency obtained by assigning user k to each slot $l \in \{1, \ldots, L_2(t)\}$. Letting $q_m(t)$, $m = 1, \ldots, k-1$, be the indices of the slots assigned to the previous $k-1$ users, the GFEO assigns user k to the slot with index

$$q_k(t) = \underset{\ell}{\operatorname{argmax}} \left\{ \max \left[\eta(L_2(t), \tilde{\boldsymbol{q}}_k(l,t)), \eta(L_2(t)+1, \tilde{\boldsymbol{q}}_k(l,t)) \right] \right\}, \tag{2.48}$$

where $\tilde{\boldsymbol{q}}_k(l,t) = [q_1(t), \ldots, q_{k-1}(t), l, 0, \ldots, 0]$. The frame length $L_2(t)$ is updated at each iteration, depending on the frame efficiency provided by each assignment. Note that the BS exploits only the partial information acquired through the observation history, while the instantaneous state of the hidden Markov process is never exploited, as the BS has no knowledge of the buffers conditions. Thus, in general, this algorithm provides a

sub-optimal policy.

Practical MDP Considerations. Due to the potentially infinite state space provided by the arrival instants of the packets in the users' buffers, it is impossible to compute (2.46) in practice. As a first approximation, instead of considering the state of the arrival instants, we consider the state of the buffer load, i.e., the state is described by the number of packets in each user's buffer. Still, under the assumption of infinite buffer capacities, the state space remains infinite. Nevertheless, we can assume finite buffers of length C and analyze the system in stability conditions, wherein the number of packets in each user is always less than C in practice. Under this further assumption, the total number of PO-MDP states is $|\mathcal{Y}| = (C+1)^K$.

Simplified GFEO

Although it is extremely accurate in the estimation of the users' buffer states and their correlation, due to the memory of the previous observations, the PO-MDP model quickly becomes unfeasible with the increasing number of users in the system. In particular, as the number of states increases exponentially with the total number of users K, the complexity of the computation of the posterior probabilities (2.45) drastically increases. Moreover, (2.45) is solved with the forward–backward algorithm, which runs with time complexity $O(|\mathcal{Y}|^2 t)$, where t is the length of the observation sequence, i.e., the current frame index. Therefore, the GFEO complexity rapidly increases as we consider long observation periods.

To overcome this limitation, we further simplify the state space and consider a low-complexity variant of the proposed greedy scheduler, named simplified GFEO (S-GFEO). With S-GFEO, at frame t the recursion in (2.45) is removed by considering $\mathcal{E}(t) = \{\boldsymbol{\beta}(t), K_{\mathrm{a}}(t-1)\}$, i.e., only the observation of frame $t-1$ and not the entire history of actions and observations. Under this assumption, the memory of the state transitions is not kept, and the computation of $\rho(\boldsymbol{\mathcal{I}}, t-1)$ is avoided by setting a uniform distribution of the states compatible with the current observation $\mathcal{E}(t)$. Let $\mathcal{Z}(t) = \{\boldsymbol{\mathcal{I}} : \mathcal{E}(t) = \boldsymbol{\beta}^*\}$ be the set of state compatible with observation $\boldsymbol{\beta}^*$, the posterior probabilities at frame t are computed from (2.41) and (2.45) as

$$\rho(\boldsymbol{\mathcal{J}}, t) = \sum_{\boldsymbol{\mathcal{I}} \in \mathcal{Z}} p_{\boldsymbol{\mathcal{I}}\boldsymbol{\mathcal{J}}}(\boldsymbol{q}(t-1)) \frac{1}{|\mathcal{Z}(t)|}. \tag{2.49}$$

Then, S-GFEO proceeds with the users' scheduling as GFEO.

2.3.6 Numerical Results

In this section, we present the numerical results for both PIMA and GFEO. Given the distinct assumptions made in the analysis of Sections 2.3.3 and 2.3.4, we provide two different sets of results for the PIMA and GFEO performance comparison, respectively.

PIMA Performance

In this section, we compare our PIMA protocol with the state-of-the-art OMA schedulers in three different scenarios: a) i.i.d. activation scenario, with $K = 50$ users, b) correlated activation scenario, also with $K = 50$ users, and c) bursty activation scenario, with a large K. Following the assumption of *short packet transmission*, the number of symbols in each packet, i.e., transmitted in a slot of duration T_{s} seconds, is set to 10. In the first set of results, the time is measured in unit symbol duration (usd), regardless the actual slot duration T_{s}, [2] and the packet generation intensity is Λ_T (in pkt/slot), Furthermore, an SNR of 10 dB is assumed at the BS.

Note that the analysis outlined in Section 2.3.3 operates under the assumption of perfect estimation of the number of active users for scheduling purposes. However, any inaccuracies in estimating K_a may lead to suboptimal slot allocations, potentially impacting the system performance. To investigate the implications of imperfect estimation on the scheduling, we introduce two scenarios within the PIMA framework. Firstly, we denote the ideal scheme, where perfect estimation of K_{a} is assumed, as PIMA-ideal. Secondly, we consider the scheme where estimation is affected by noise, simply referred to as PIMA, in the context of error-prone scheduling.

For performance comparison, we consider a) the standard TDMA, which provides fixed-duration frames of K slots, with one user assigned per slot deterministically, b) a stabilized version of the SALOHA protocol, c) the NOMA-ALOHA protocol, and d) the CRA-2 protocol of [35] with preambles of length $M_{\mathrm{p}} = K/2$ and K.

Stabilized Slotted ALOHA. For the SALOHA protocol, we consider Rivest's stabilized SALOHA [56, Chapter 4], [57], where all users generating packets at slot l are backlogged with equal probability. The backlog probability is computed for each user through a pseudo-Bayesian algorithm based on an estimate of the number of backlogged nodes $v(l)$ as

$$\alpha(l) = \min\left(1, \frac{1}{v(l)}\right), \tag{2.50}$$

[2] The usd is the inverse of the bandwidth if the Nyquist sampling rate is used. All the lengths of the sequences, slots, and beacons are given in usd.

where

$$\upsilon(l) = \begin{cases} \upsilon(l-1) + K\theta + (e-2)^{-1} & \text{if } c_l = 0, \\ \max(K\theta, \upsilon(l-1) + K\theta - 1) & \text{if } c_l = 1, \end{cases} \tag{2.51}$$

is the estimated number of backlogged users (with $\upsilon(0) = 0$) and $\theta = 1 - e^{-\lambda}$ is the packet generation of probability at slot l.

NOMA-ALOHA. For the NOMA-ALOHA [58], we assume that active users transmit with high (`H`) or low (`L`) power chosen with equal probability. According to [58] a relatively large number of users, i.e., up to a few dozen, can transmit with `L` without interfering with the users transmitting with level `H`. In such an implementation, a collision occurs when two or more users transmit with the same power level. Moreover, if two or more active users choose `H` it is impossible to decode the packets transmitted with both `H` and `L`, as the interference cancellation fails. Note that this is an ideal assumption, as we do not consider the noise term but only the interference, assuming high SNR. The same backlogging mechanism (2.51) of SALOHA is adopted.

Modified CRA-2 Protocol. The CRA-2 protocol was proposed in [35]. Similarly to PIMA, each frame includes two sub-frames, and in the first sub-frame active users are identified with a temporary identifier, rather than just counted. To this end, each active user uniformly randomly chooses and transmits a sequence of complex symbols of length M_{p} (*preamble*), from a preamble pool known to both users and BS. The BS receives all preambles simultaneously and detects them. Preambles are used as temporary identifiers for the active users, and the BS schedules the data transmission in the second sub-frame by allocating one slot per each detected preamble. Here, we assume that preambles are orthogonal; therefore, the number of preambles equals their length M_{p}. When $M_{\mathrm{p}} = K$, each user is uniquely assigned to a preamble, while for $M_{\mathrm{p}} = K/2$, the preamble choice is random. In the latter case, if two or more users transmit the same preamble (and the BS detect it), they are assigned the same slot and collide. For both schemes, we consider the probability of misdetection in the preamble in the first subframe $P_{\mathrm{md}} = 0.1$. Note that in [35] preambles are assumed to be non-orthogonal, and a CS-based algorithm is applied. However, preamble detection in the presence of noise is not considered and a fixed misdetection probability is assumed. The impact on system performance of different CS algorithms has been discussed for the case of multiple measurements (e.g., multiple antennas in BS) in [59]. Although on one hand CS-based detection allows increasing the number of preambles and reducing the probability of collision, on the other hand, it also produces a high probability of misdetection when BS is equipped with a single antenna (single measurement) and a large number of users are active [60].

Table 2.1: Overhead comparison of the considered protocols.

Protocol	Uplink Overhead	Downlink Overhead
PIMA with complete CSI	1 usd	2 usd
PIMA with incomplete CSI	$\propto K^2$ usd	2 usd
CRA-2	M_{p} usd	$\hat{K}_{\mathrm{a}}$ usd

Comparing PIMA with CRA-2, we have two main differences: a) the first sub-frame is shorter for PIMA than for CRA-2, and b) the second sub-frame has the same length for both approaches. Thus, on the one hand, overall the PIMA frame is shorter, reducing the average number of packets generated in each frame, and this reduces the average number of packets accumulated in the buffers before transmission in the next frame. On the other hand, in PIMA users may collide in the second sub-frame due to a non-exclusive allocation, which increases (with respect to CRA-2) the number of packets to be re-transmitted in the next frame (thus increasing the average number of users in buffers). Lastly, a wrong counting of users in the PIA sub-frame or a wrong identification in the first CRA-2 sub-frame increases the collision probability of both schemes. The numerical results presented in this section will compare the performance of both schemes, taking into account all these effects.

Overhead Comparison. Since the packet acknowledgments are neglected for all schemes, both TDMA and SALOHA do not entail any overhead. For both PIMA and the preamble-based solutions, we assume that a 64-QAM modulation is used to modulate the SB, and the list of the scheduling sequence is set to $J = 64$. Under the aforementioned assumptions, the total overhead induced by the PIA sub-frame is constant and equal to $L_1 = 3$ usd (one for AI and two for SB, as the overhead of the ReB is neglected). Instead, for preamble-based approaches, the overhead is given by the preamble of M_{p} usd and the BS feedback, which is typically longer than the SB. In particular, assuming that K_{a} preambles are detected by the BS, the identifiers of these preambles are fed back in broadcast, in the order of slot allocation (for the subsequent data transmission), providing a total overhead of $M_{\mathrm{p}} + \hat{K}_{\mathrm{a}}$ usd. The overhead of ReB is neglected and does not play any role in the performance comparison, as its length is comparable for all the considered schedulers. The overhead of the compared schemes (in usd) is summarized in Table 2.1.

Performance metrics. For the i.i.d. and correlated activation case, performance is assessed in terms of both *average frame efficiency* $\bar{\eta}$ and *average latency* $\bar{D}$. The former metric is the average of the conditional frame efficiency for $K_{\mathrm{a}} > 0$, i.e., $\bar{\eta} = \mathbb{E}[\eta(K_{\mathrm{a}})|K_{\mathrm{a}} > 0]$. In the latter metric, the average is computed among all successfully delivered packets.

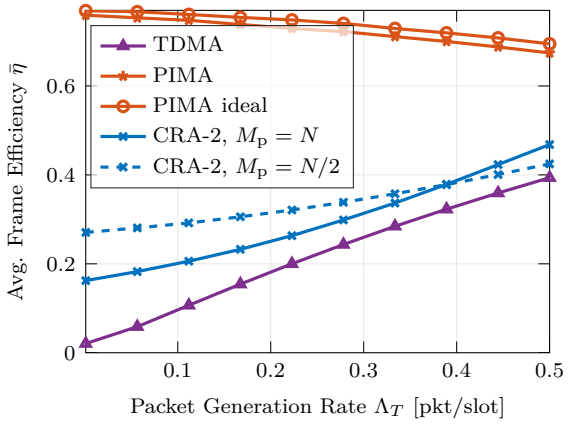

Figure 2.5: Average frame efficiency versus the total packet generation rate for $K = 50$ and i.i.d. activations.

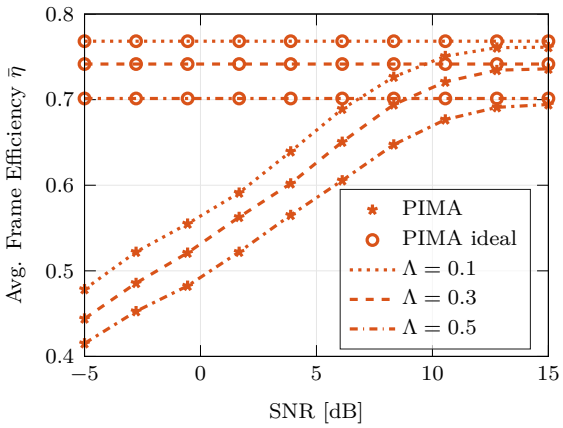

Figure 2.6: Average frame efficiency versus the SNR for $K = 50$ and $\Lambda_T = \{0.1, 0.3, 0.5\}$, under i.i.d. activations.

Moreover, in the case of i.i.d. activations, we also consider the packet dropping probability P_drop, counting the packets dropped due to both collisions and replacements in the unit-length buffers when generations occur. This probability is 0 in the correlated activation case for all schemes, due to the possible retransmission and the infinite-length queues.

Finally, for bursty activations, the performance of the system is evaluated in terms of the *burst transmission time* D_B, i.e., the time needed to transmit all the packets generated in a traffic burst, and its average $\bar{D}_\mathrm{B} = \mathbb{E}[D_\mathrm{B}]$, computed over many bursts.

i.i.d. activations. We first report and discuss the results obtained for i.i.d. user activity and $K = 50$ users. In this activation scenario, retransmissions are not allowed. Therefore, SALOHA does not include backlogging, and each user attempts the transmission immediately upon the packet generation, i.e., $\alpha(l) = 1, \forall l$.

Firstly, a comparison of the average frame efficiency achieved by each of the schemes is shown in Fig. 2.5, as a function of the total packet generation rate Λ_T. While this metric cannot be defined for SALOHA and NOMA-ALOHA as they do not divide time into frames, we observe that TDMA, adopting the constant frame length, provides a very low frame efficiency. Moreover, since only the frames with $K_\mathrm{a} > 0$ are considered in the average, PIMA achieves its highest frame efficiency at extremely low traffic due to its low overhead, and the efficiency slightly decreases at higher traffic due to collisions. As the traffic intensity increases, PIMA always achieves the highest frame efficiency, outperforming both the TDMA and the preamble-based schemes, whose overhead severely affects performance. Fig.2.6, instead, illustrates the relationship between SNR and average frame

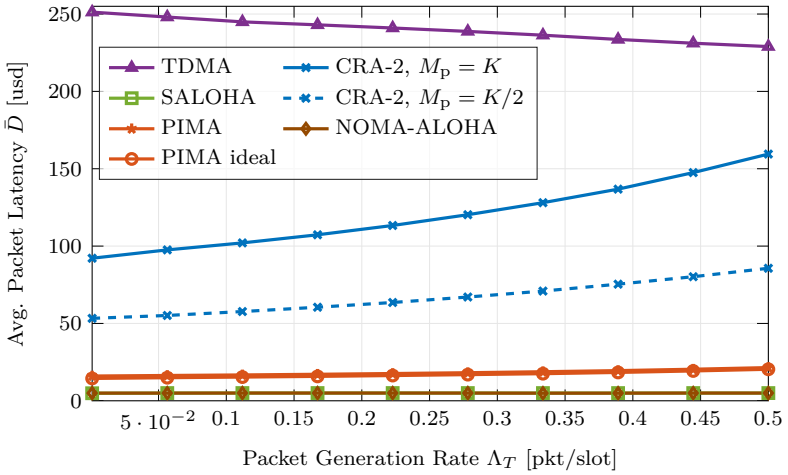

Figure 2.7: Average latency versus the total packet generation rate for $K = 50$ and i.i.d. activations.

efficiency of PIMA, showing a monotonically increasing trend, in all the considered traffic conditions. Notably, for SNR values exceeding 10 dB, the curves approach the PIMA ideal upper bound.

Figs. 2.7 and 2.8 show the effect of the packet generation rate on the average latency and packet dropping probability, respectively. In this context, all packets generated during a frame transmission wait, on average, $K/2$ slots in low traffic conditions, therefore TDMA shows the highest latency. Still, latency decreases as the traffic increases, since the buffering delay is reduced by the new packets replacing the older ones in the queue. However, the dropping probability increases up to over 0.1 in high-traffic conditions. Instead, SALOHA and NOMA-ALOHA attain the lowest latency in this scenario, transmitting all packets immediately after their generation. Indeed, these schemes provide a lower bound on the latency, as all colliding packets are discarded and do not contribute to its evaluation. However, dropped packets increase the dropping probability, which approaches 1 for SALOHA at large Λ_T and is comparable to both TDMA and NOMA-ALOHA. The CRA-2 scheduler with K preambles, instead, is collision-free, and it drops a reduced number of buffered packets due to its shorter DT sub-frame with respect to TDMA. Indeed, CRA-2 achieves the lowest P_{drop} among the considered approaches: this improvement comes at the cost of higher latency, due to the longer time needed for the first sub-frame. Lastly, while the already mentioned schemes drop packets due either to collision (SALOHA) or new packet generations (TDMA and CRA-2 with $M_{\mathrm{p}} = K$), both PIMA and CRA-2 with $M_{\mathrm{p}} = K/2$ merge the advantages of the aforementioned solutions. On one hand, PIMA provides a higher collision probability than the preamble collision probability of CRA-2. On the other hand, collisions are compensated by a reduced dropping probability of

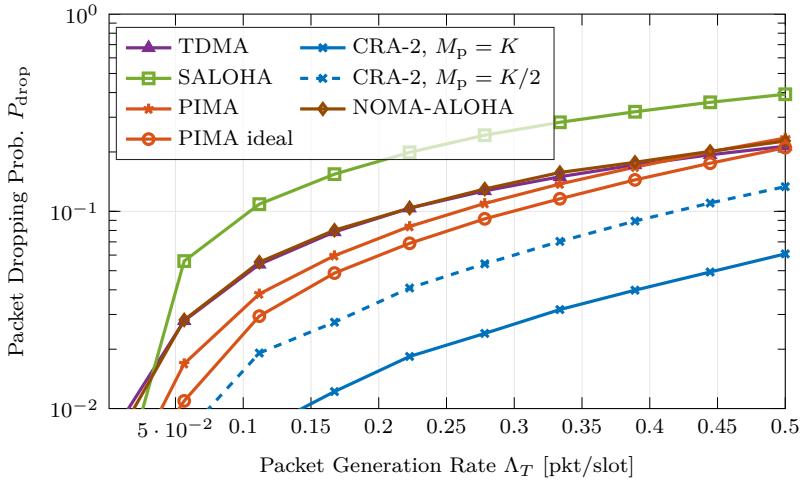

Figure 2.8: Average packet dropping probability versus the total packet generation rate for $K = 50$ and i.i.d. activations.

newly generated packets, thanks to a shorter first sub-frame. Thus, while CRA-2 achieves a considerably lower dropping probability than PIMA, its latency is higher than that of PIMA, which guarantees close-to-minimum latency.

Correlated Activations. We now assess the performance of the correlated user activation scenario, assuming infinite queue lengths and an infinite number of possible transmission attempts of collided packets. We consider a total number of $K = 50$ users and performance results are shown as a function of the traffic intensity $0.001 \leq \Lambda_T \leq 0.35$ pkt/slot.

First, Fig. 2.9 shows the average frame efficiency $\bar{\eta}$, as a function of the total packet generation rate. The performance is almost the same as in the i.i.d. activation scenario. This is mostly due to the fact that, in stability conditions, few retransmissions are performed multiple times. While all the observations on Fig. 2.5 still hold, we also note a very slight degradation of PIMA, as it is designed for i.i.d. activations and does not take into account previous collisions.

Second, Fig. 2.10 shows the average packet latency as a function of the packet generation rate for $K = 50$ users. Still, the latency of TDMA is much higher than that of other schemes, due to its frame length (K, the maximum among all schemes). We also observe that, at low traffic, the PIMA scheduler achieves extremely low latency, comparable to the minimum achieved by SALOHA. In higher traffic conditions, instead, the SALOHA backlogging mechanism prevents users from transmitting their buffered packets immediately, thus increasing the average latency. This effect is mitigated in PIMA, whose latency is reduced, due to its better ability to adapt to instantaneous traffic load.

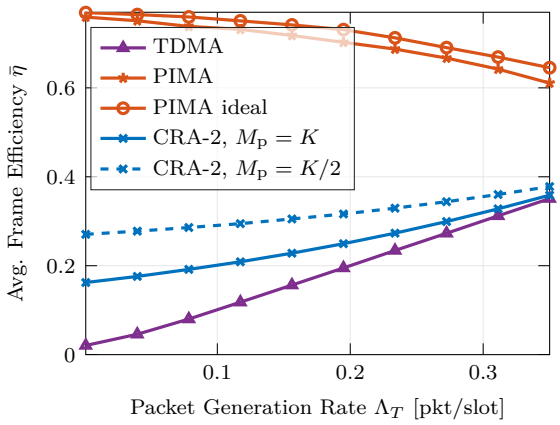

Figure 2.9: Average frame efficiency versus the total packet generation rate for $K = 50$ and correlated activations.

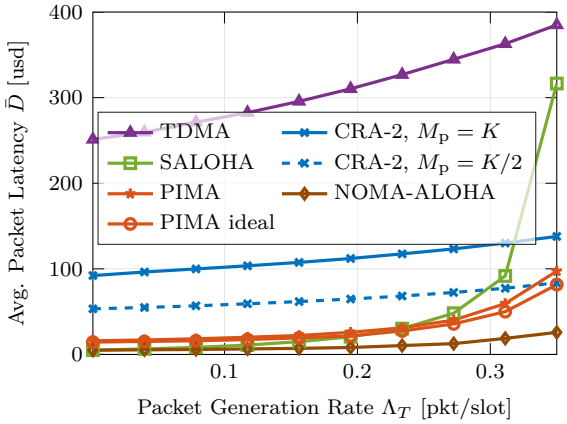

Figure 2.10: Average packet latency versus the total packet generation rate for $K = 50$ and correlated activations.

For the preamble-based approach, instead, we observe that overhead plays a crucial role in overall latency, and shorter preambles yield better performance, while PIMA is still outperforming CRA-2. Finally, NOMA-ALOHA is the most effective protocol in terms of latency. However, we stress that with respect to the other compared schemes, its implementation requires high SNR at the BS to perform SIC, which is here assumed to be ideal.

The average latency comparison for different numbers of users in the system (K) is shown in Fig. 2.11, for $\Lambda_T = 0.3$ pkt/slot. The performance of SALOHA and NOMA-ALOHA remains constant for all the considered values of K, as the performance of such protocols is only dependent on the traffic intensity. Differently, the latency provided by the CRA schemes strictly depends on the number of users in the system, as preamble lengths need to be tuned accordingly. Indeed, the larger the number of users in the system, the longer the preamble is required to ensure user identification, with a direct impact on the average packet delay. The proposed PIMA protocol achieves a low latency for all the considered values of K. Still, performance significantly changes for different numbers of users. This is mainly due to the increased number of collisions occurring for large K. Indeed, the optimal DT sub-frame duration $L_2(t)$ solving (2.28) is proportional to the number of active users in the system $K_\mathrm{a}(t)$. However, with the allocation of (2.27), once $L_2(t)$ is fixed, more users are assigned to the same slots for large K, increasing both the collision probability and (as a consequence) the average packet latency.

Lastly, in the correlated activation scenario, we have considered infinite-length queues, thus we may wonder if such queues are stable for the considered traffic intensity. However,

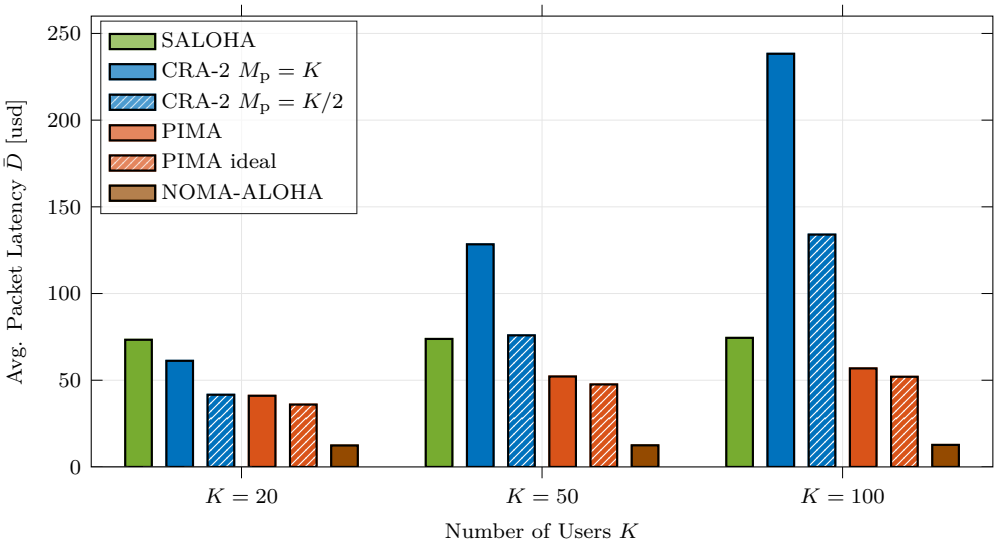

Figure 2.11: Average packet latency versus the number of users K, for $\Lambda_T = 0.3$ pkt/slot and correlated activations.

since collision statistics in this scenario are quite difficult to compute due to the correlated nature of activations, we leave an in-depth analysis of the stability for future study.

Bursty Activations. We now investigate the performance in the bursty activations scenario. We first assess the performance obtained for a single burst of intensity Λ_{B}, and then discuss some constraints on the burst interarrival time. As discussed in Section 2.3, here we assume that a random number of active users K_{a}, out of an arbitrarily large number of users in the system K, generate a single short packet to be transmitted in the following time slots. As we consider an arbitrary large K, the length of the DT sub-frame in PIMA is here derived according to Theorem 1.

The number of packet generations in a burst follows a Poisson distribution, with average $\Lambda_{\mathrm{B}} \in [10, 10000]$ pkt/burst. For comparison purposes, we consider CRA-2 with fixed preamble lengths $M_{\mathrm{p}} = 1000$ and 10000. We also consider an ideal solution, wherein the length of the preamble is adapted to the average number of generated packets, that is, $M_{\mathrm{p}} = \Lambda_{\mathrm{B}}$. Note that this ideal solution is hardly implementable, as it requires different preamble pools based on the traffic generation rate. Moreover, we do not consider SALOHA and NOMA-ALOHA, as all packets simultaneously generated would collide with extremely high probability (1 for SALOHA). We also exclude TDMA, as a large K results in very long frame lengths. Note that a longer list of random sequences (that is, a longer overhead) for the scheduling vector encoding (Section 2.3.1) is necessary as the number of users in the system increases. In the following, we still consider a PIA sub-frame overhead

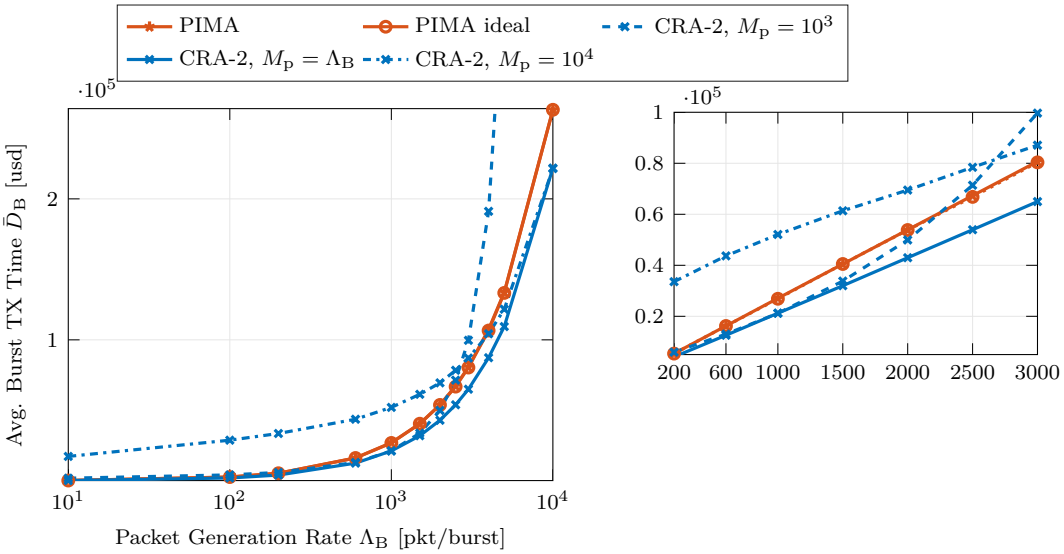

Figure 2.12: Average burst transmission time versus the packet generations rate (in log scale) in a bursty scenario. The zoomed plot reports results for 600 pkt/burst $\leq \Lambda_B \leq$ 3000 pkt/burst, in linear scale.

of $L_1 = 3$ symbols, which can be easily accommodated by adopting a higher modulation order at the BS for SB transmission.

Fig. 2.12 shows the average burst transmission time as a function of the average number of packet generations. First, we observe a constant gap between PIMA and the ideal preamble-based solution with $M_p = \Lambda_B$, while fixed-length preambles achieve better performance when the number of active users is comparable to the preamble length. In particular, the CRA-2 solution with $M_p = 1000$ preambles achieves a lower burst transmission time only for 400 pkt/burst $\leq \Lambda_B \leq$ 2000 pkt/burst, while at least $\Lambda_B = 4000$ pkt/burst is needed when $M_p = 1000$. For a low average number of packet generations, PIMA achieves the best performance due to its reduced overhead. For faster packet generations, both fixed-length preamble approaches suffer from preamble collisions, which implies a much higher packet transmission time due to retransmissions. Therefore, while PIMA adapts to all traffic conditions, preamble-based approaches should adopt different preamble pools depending on the traffic intensity to achieve a good performance.

Finally, the ECCDF of the burst transmission time is shown by Fig. 2.13 for $\Lambda_B = 600$ and 3000 pkt/burst. The results confirm the comments on Fig. 2.12, with the ideal case $M_p = \Lambda_B$ always attaining the lowest transmission time and the fixed-preamble approaches outperforming PIMA only for a preamble length comparable to the number of packet generations.

The plot gives also an indication of the minimum burst interarrival time τ_B that mini-

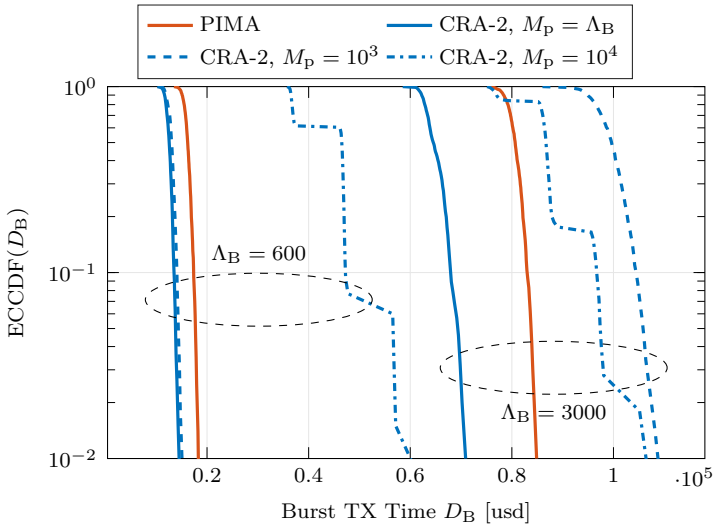

Figure 2.13: Empirical complementary cumulative distribution function (ECCDF) of the burst transmission time.

mizes the probability of overlap between two traffic bursts. For example, from Fig. 2.13, the probability of overlap of PIMA is 10^{-2} if $\tau_B = D_B \approx 19 \cdot 10^3$ usd for $\Lambda_B = 600$ pkt/burst, and if $\tau_B \approx 85 \cdot 10^3$ usd for $\Lambda_B = 3000$ pkt/burst. In this comparison, PIMA is shown to be effective in minimizing burst transmission time, being very close to the CRA-2 solutions with $M_p = 1000$ and $M_p = \Lambda_B$ in the low traffic scenario, while outperforming both fixed-length preamble solutions for $\Lambda_B = 3000$ pkt/burst.

On the Estimation of K_a. Note that, all Figs. 2.5-2.12 show a negligible performance gap between PIMA (where estimation of K_a is subject to errors) and PIMA where users are perfectly counted in the PIA sub-frame. Therefore, the optimal scheduling analysis provided in Section 2.3.3 nicely approximates the case of imperfect estimation for the considered SNR. In Fig. 2.13 we have not included the performance of PIMA ideal to improve the readability, while, based on the results shown in Fig. 2.12, performances are almost identical to those of PIMA.

GFEO and S-GFEO Performance

In a different setting with respect to the previous section, we present the numerical evaluation of GFEO and S-GFEO. The results are obtained through simulation over a time duration of 10^6 s, and for all schemes, we adopt the third numerology of the new radio (NR) specification, which provides DT time slots of $T_s = 0.125$ ms [61]. Note that, differently from the previous set of results, in the following, the delay is measured in seconds

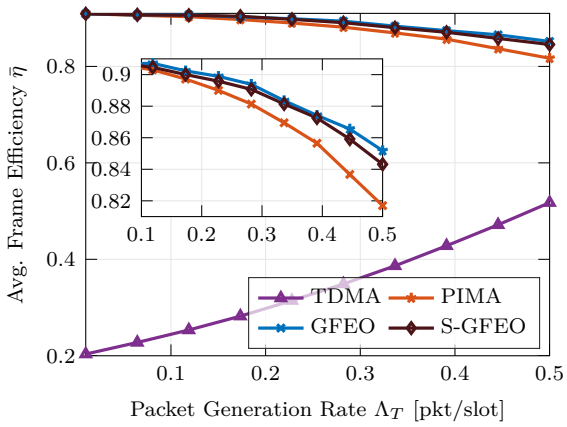

Figure 2.14: Average frame efficiency versus the total arrival rate for $K = 5$.

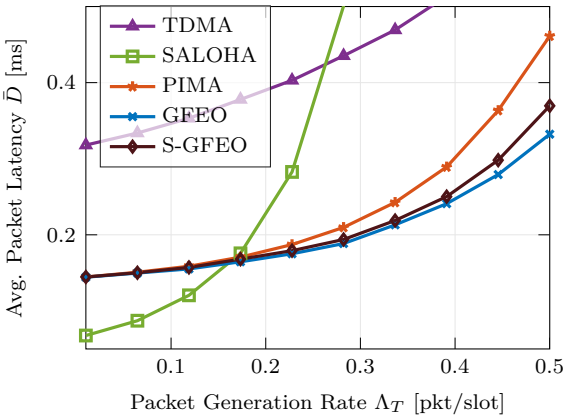

Figure 2.15: Average packet latency versus the packet arrival rate for $K = 5$.

and not in usd. The performance of GFEO and S-GFEO, still assessed in terms of average frame efficiency $\bar{\eta}$ and average latency $\bar{D}$, are here compared with TDMA, SALOHA and PIMA. Moreover, for PIMA, GFEO, and S-GFEO, we assume an error-free user enumeration with a fixed L_1.

Firstly, we consider a scenario with $K = 5$ users with traffic intensity $0.01 \leq \Lambda_T \leq 0.5$, which corresponds to the queues' stability regime of the GFEO algorithm, which has been derived empirically from the simulations. The length of the PIA sub-frame is set to $L_1 = T_s/10$, which is sufficient to guarantee negligible enumeration error probability. Fig. 2.14 shows the average frame efficiency $\bar{\eta}$ as a function of the total packet generation rate. The zoom plot inside the figure highlights the performance gap between the PIMA-based schedulers. Note that the performance of SALOHA is not reported, as the frame efficiency cannot be defined for fra
me-less protocols SALOHA. TDMA, adopting the constant maximum frame length, provides a very low frame efficiency, while the PIMA-based schedulers attain close-to-optimal performance in the whole considered range of traffic intensity. Among these schedulers, GFEO, which exploit the correlation knowledge at best, achieve the highest frame efficiency providing approximately up to 5% gain with respect PIMA. However, the results also show that the gap between GFEO and S-GFEO is almost negligible, therefore the approximations introduced with S-GFEO have a very limited negative impact on the system performance. Finally, while the frame efficiency is increasing with the traffic intensity for TDMA due to the reduced unused time slots, it is slightly decreasing for the PIMA-based schemes due to the increasing chances of collisions.

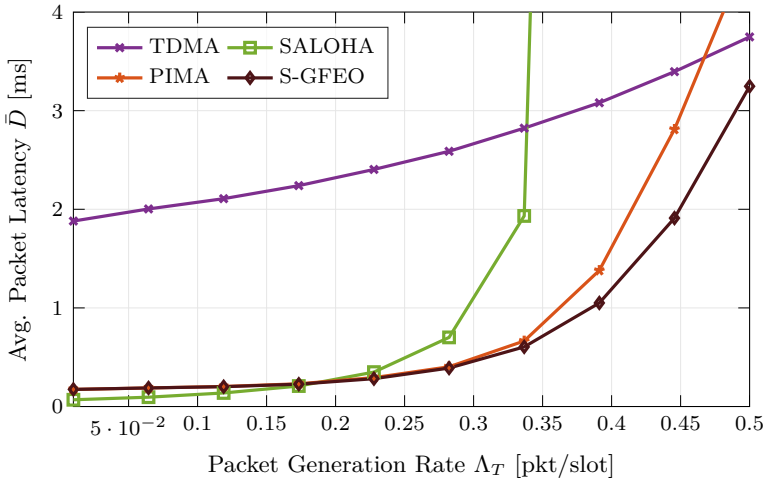

Figure 2.16: Average packet latency versus the packet arrival rate for $K = 30$.

The comparison of the average packet latency is shown in Fig. 2.15. At low traffic, TDMA provides the larger latency due to the frame length fixed to K, while SALOHA achieves extremely low latency due to the absence of collisions. Instead, at high traffic intensity, the SALOHA backlogging mechanism prevents the users from transmitting their buffered packets immediately, therefore increasing the average latency. The PIMA-based schemes, due to their better capability of adapting to traffic conditions, outperform both schemes when the traffic intensity is moderately large. In particular, both GFEO and S-GFEO achieve the lowest latency, still with an almost negligible gap between these greedy solutions.

Finally, we consider a scenario with $K = 30$ users and a fixed PIA sub-frame length $L_1 = T_s/4$. Here, the performance of GFEO is not reported due to its extremely high complexity for a large number of users. However, we have observed that its low-complexity variant S-GFEO scales better at the cost of a negligible loss in performance. Fig. 2.16 depicts the average packet latency achieved by the compared schemes. First, note that similarly to Fig. 2.15, the results show a huge latency reduction of the PIMA-based solutions with respect to the other considered schemes. We stress that the average latency counts only for the successfully delivered packets and that we are considering values of Λ_T such that the queues' stability is verified for PIMA and GFEO. Therefore, TDMA seems to outperform PIMA at high traffic, due to the instability conditions of TDMA, which drops the oldest packets in the users' queues when the maximum capacity is reached. Still, we observe that S-GFEO achieves the lowest latency among all the compared schemes.

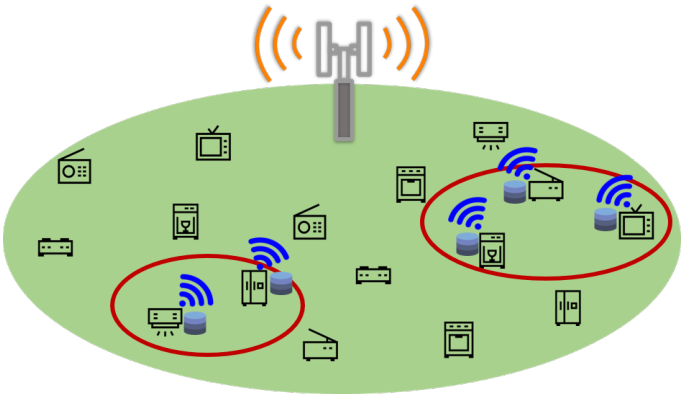

Figure 2.17: Considered system model for correlated packets generation. In this example, underlying processes (red ellipses) trigger the uplink transmissions of the users in the same geographic area.

2.4 Distributed OMA Scheduling

In this section, we investigate an OMA uplink solution under *correlated traffic generation*. In particular, the term correlation here refers to the scenario in which the traffic correlation is due to correlated packet generations, which may result from an underlying process, and it is not only due to collisions and retransmission attempts. In the following, time is divided into frames, but differently from the frame structure of PIMA, all frames have equal lengths (in slots), and the PIA sub-frame is absent. Moreover, scheduling is fully distributed; without any coordination from the BS (except for the time synchronization), each active user randomly selects a slot for transmission according to its individual PDF. This PDF is designed specifically for each user and depends on the number of transmission attempt. The PDFs are obtained by an iterative reinforcement learning (RL)-based approach, carried out locally at each user, to minimize the probability of collision. To this end, we first model the distributed optimization problem as a repeated Markov game with incomplete information, where the users are the players and transmission slots are the actions. Then, we resort to the linear-reward-inaction (LRI) algorithm for the PDF optimization.

2.4.1 Frame Structure, Packet Generation, and Access Protocol

Time is split into frames of fixed length, each split into L slots. We again consider K users in the system, which activate at frame t in a correlated fashion according to an underlying process, as reported in the example in Fig. 2.17. Note that, as here the PIA subframe is absent and the length of each frame is constant, we are focusing on the particular case with $L(t) = L_2(t) = L$, $\forall t$.

For notational convenience, let $y_k(t)$ be the indicator function of packet generation, i.e., $y_k(t) = 1$ if user k generates a packet at frame t, while $y_k(t) = 0$ otherwise; let us also define the row vector $\boldsymbol{y}(t) = [y_1(t), \ldots, y_K(t)]$. Packet generations are triggered by events common to multiple (random) users, therefore variables $y_k(t)$, $k \in \{1, \ldots, K\}$ are correlated. Let $w_k = \mathbb{P}(y_k(t) = 1)$ be the marginal probability of packet generation at user k. In Section 2.4.3, we will consider a specific correlated traffic generation model, while the derivation of our proposed scheme holds in general for any correlated traffic.

We assume that each user can store only one packet for transmission and a user that already stores a packet will drop other generated packets. Packets are generated at the end of each frame and stored (one per user), then their transmission starts in the next frame. Each user with a stored packet attempts to transmit it in each frame, selecting slot $q_k(t) \in \{1, \ldots, L\}$, until either the packet is successfully delivered to the BS, or a maximum number of transmissions β is reached. In this latter case, the packet is discarded.

Note that β is strictly related to the latency constraints. In particular, following the fixed frame length assumption, the maximum packet latency is proportional to βL.

Let $\nu_k(t) = i$ indicate that user k in frame t is performing the transmission attempt $i > 0$ of its packet. We also set $\nu_k(t) = 0$ if $y_k(t) = 0$, and define the vector $\boldsymbol{\nu}(t) = [\nu_1(t), \ldots, \nu_K(t)]$. If the maximum number of transmission attempts is reached in frame t, the packet is discarded, and at the next frame, we have $\nu_k(t+1) = y_k(t)$.

The probability of user k transmitting in slot l at the i-th attempt is

$$p_{k,l}(i) = \mathbb{P}(q_k(t) = l | \nu_k(t) = i). \tag{2.52}$$

Thus, the PDF of the slot selected for transmission by user k in frame t is $\boldsymbol{p}_k(\nu_k(t))$, which depends on the number of transmissions $\nu_k(t)$ of the current packet.

Therefore, vector $\boldsymbol{p}_k(\nu_k(t)) = [p_{k,1}(\nu_k(t)), \ldots, p_{k,L}(\nu_k(t))]^{\mathrm{T}}$ is the discrete PDF defining the access scheme of user k at the $\nu_k(t)$-th transmission attempt. For example, a FSA protocol selects the slot uniformly at random and independently for users, i.e., $p_{k,l}(i) = \frac{1}{L}$. The design of user PDFs is the subject of the scheduling optimization and will be discussed in the next sections.

Successful Transmission Probability and BS Feedback. Recall that $\psi_k(t) = 1$ if the transmission of user k at frame t is successful and $\psi_k(t) = 0$ otherwise. The success probability

at frame t is

$$\omega_{k,l}(t) = \mathbb{P}(\psi_k(t) = 1 | q_k(t) = l) = \prod_{\substack{m=1 \\ m \neq k}}^{N} [1 - \mathbb{P}(\nu_m(t) > 0) p_{m,l}(\nu_m(t))]. \tag{2.53}$$

At the end of frame t, the BS sends in unicast the acknowledgment to each user k for which the packet was successfully received.

Knowledge Assumptions. The statistics of packet generation are not known and the acknowledgments are sent in unicast, thus the outcome of transmissions is known only to the transmitting user.

2.4.2 PDF Optimization

We now propose a fully distributed algorithm for the optimization of the user PDFs $\boldsymbol{p}_k(i),\ i \in \{1, \ldots, \beta\}$. The algorithms operate locally at each user, with the aim of maximizing the user's individual throughput, i.e., minimizing the number of retransmissions.

To this end, we first model our distributed OMA scheme as a Markov game, wherein users are the players competing in the slot selection. Markov games are of particular interest as they represent a specific framework for multi-agent RL. Indeed, differently from a MDP, wherein a single adaptive agent interacts with the environment and secondary agents can only be part of it, Markov games allow modeling of multiple adaptive agents (players) interacting with each other for cooperative or competing goals [62]. Several multi-agent RL algorithms have been developed to learn equilibrium points in Markov games. For the specific task of slot selection, we resort to LRI, a learning automata algorithm, which learns an equilibrium point of the game by updating the PDFs at each retransmission. LRI provably converges to sub-optimal deterministic solutions, leading each user to always transmit in the same slot when facing a certain transmission attempt.

Slot Selection As a Markov Game

Game Definition. Our slot selection process can be modeled as a Markov game (also called stochastic game), where users are the players, and their actions are their slots selected for transmission. The game is played in multiple *rounds*, once per frame.

The action taken by each user k in frame t depends only on the number of retransmissions $\nu_k(t)$, which represents the *state* of the player. There are $\beta + 1$ states, denoted as $0, 1, \ldots, \beta$, where state 0 indicates that the user has no packet to transmit, while at state β the maximum number of retransmissions is reached. The *strategy* of player k is

the set of PDFs by which actions are taken, i.e., $\{\boldsymbol{p}_k(i), i = 1, \ldots, \beta\}$; note that at state 0 only one action (no transmission) is accessible. Let $\boldsymbol{\pi}_k$ be the *strategy matrix* of player k, defined as

$$\boldsymbol{\pi}_k = [\boldsymbol{p}_k(1), \ldots, \boldsymbol{p}_k(\beta)]. \tag{2.54}$$

Let us also define the matrix collecting all strategies of each user in each state as $\boldsymbol{\pi} = [\boldsymbol{\pi}_1, \ldots, \boldsymbol{\pi}_K]$.

At the end of each round (frame), player k receives the *reward* $\psi_k(t)$, which depends on the actions of all the players. The *utility function* is the expected reward, which for each user k can be written as

$$u_k(\boldsymbol{\pi}) = \mathbb{E}[\psi_k(t)], \tag{2.55}$$

where we highlighted the dependency of the utility from the strategies. The objective of user k, is to find a strategy matrix $\boldsymbol{\pi}_k^*$ which maximizes its own expected reward, i.e.,

$$\boldsymbol{\pi}_k^* = \underset{\boldsymbol{\pi}_k}{\operatorname{argmax}}\, u_k(\boldsymbol{\pi}). \tag{2.56}$$

This is a game of incomplete information since players have no knowledge of the other players' actions. Each player selects its own strategy with an individual objective, thus the game is non-cooperative.

State Transitions. We now describe the state transitions and their probabilities. The transition from state 0 to state 1 is due only to a new packet generation, thus occurs with probability w_k. States $i = 1, \ldots, \beta - 1$, evolve either towards state 0 (successful transmission) or towards state $i + 1$ (failed transmission): the first case occurs with probability $\omega_{k,l}(i)$ upon action $q_k(t) = l$, while the latter occurs with probability $1-\omega_{k,l}(i)$. When in state β, the packet is either successfully received or discarded and possibly replaced by a new packet: thus, this state evolves with probability w_k to state 1 and with probability $1-w_k$ to state 0. When in state 0, only one action is possible (no transmission) denoted with 0 in the square.

State of the Game. The *state of the game* at round t is the collection of the states of all players, $\boldsymbol{\nu}(t)$.

Learning The Strategies

The distributed nature of the optimization problem (2.56) requires the use of distributed intelligence at the users, and, therefore, represents the main rationale behind the choice of multi-agent RL techniques. In particular, the objective of each user is to find a strategy

that maximizes the expected reward (2.56) at each transmission attempt. To this end, we resort to the LRI algorithm [63], which is run locally by each user and works iteratively, with one iteration per frame. Let $\{\boldsymbol{p}_k^{(t)}(i), i = 1, \ldots, \beta\}$ be the strategy of user k at frame t, where $\boldsymbol{p}_k^{(t)}(i) = [p_{k,1}^{(t)}(i), \ldots, p_{k,L}^{(t)}(i)]$.

At the first iteration, we start with a uniform PDF for all the users, i.e., $p_{k,l}^{(0)}(i) = \frac{1}{L}$ for all $i \in \{1, \ldots, \beta\}$ and $l \in \{1, \ldots, L\}$.

At iteration t, user k (storing a packet) transmits in a random slot selected according to its state and strategy. For failed transmissions ($\psi_k(t) = 0$), the strategy is not updated, thus $\boldsymbol{p}_k^{(t+1)}(i) = \boldsymbol{p}_k^{(t)}(i)$, $i = 1, \ldots, \beta$. If a packet is successfully received ($\psi_k(t) = 1$), user k updates its strategy as follows

$$p_{k,l}^{(t+1)}(\nu_k(t)) = \begin{cases} p_{k,l}^{(t)}(\nu_k(t)) + \alpha\psi_k(t)[1 - p_{k,l}^{(t)}(\nu_k(t))] & l = q_k(t), \\ p_{k,l}^{(t)}(\nu_k(t)) - \alpha\psi_k(t)p_{k,l}^{(t)}(\nu_k(t)) & l \neq q_k(t), \end{cases} \tag{2.57}$$

where α is the *learning rate*, which dictates the speed of the learning process. PDFs relative to other retransmissions than $\nu_k(t)$ are left unaltered, i.e., $\boldsymbol{p}_k^{(t+1)}(i) = \boldsymbol{p}_k^{(t)}(i)$, $i \neq x(t)$. From (2.57) we note that the probability of transmitting in slot k is increased, while the other slots are penalized.

We remark that LRI does not require any knowledge of the other players' states and strategies. In fact, from (2.57), it can be seen that the algorithm is fully distributed.

LRI Convergence

It is proven that, for small values of α, the LRI algorithm converges to a pure Nash equilibrium [64], i.e., the strategy of any player k maximizes its utility function, given the strategies of all other players [65]. Moreover, LRI converges to a *pure strategy*, i.e., only one slot is deterministically selected by each user at each retransmission.

However, note that LRI may not achieve the maximum utility $u_k(\boldsymbol{\pi})$, and in general will not even provide the maximum sum of utility among all users. Still, it converges to a deterministic policy, ensuring the stability of the algorithm.

2.4.3 Numerical Results

To assess the performance of the proposed solution, we consider a network where each frame comprises $L = 4$ slots and $K = 20$ users are uniformly randomly placed in a square area of side 10 m.

We consider the space-time Poisson process traffic model described in [10], with modifications to account for packet generations across multiple frames. First, active frames,

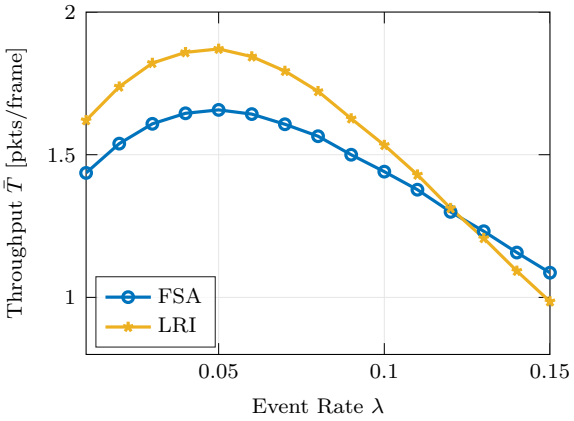

Figure 2.18: Average system throughput as a function of λ, for $\mu = 0$ and $\beta = 5$.

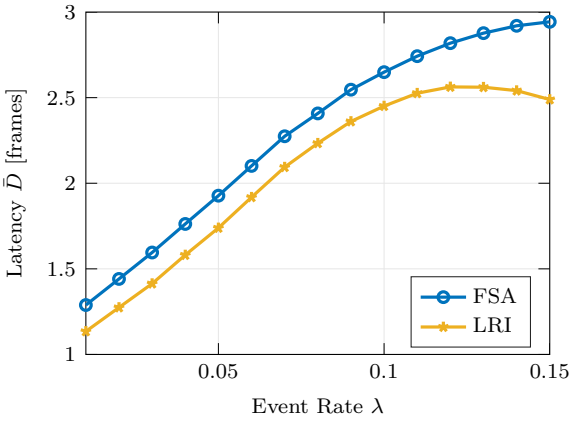

Figure 2.19: Average packet transmission time as a function of λ, for $\mu = 0$ and $\beta = 5$.

i.e., those in which one or more packets are generated, follow a temporal Poisson process with intensity μ. Within these active frames, several positions (referred to as *events*) are selected in the considered area according to a spatial Poisson process with intensity λ, as for [10]. Specifically, in these active frames, all users within a radius of 1.25 m from an event generate one packet each. By adjusting the parameters μ and λ, we observe two main effects. On one hand, as μ is the rate of the temporal process, its increment results in more frequent active frames. Conversely, increasing λ has a dual impact: it increases the correlation in packet generation and increases the average number of generated packets within the cell in the active frames.

Performance is assessed in terms of average packet transmission time (delay) and system throughput. In formulas, the average packet transmission time (in frames) is

$$\bar{D} = \frac{1}{K} \sum_{k=1}^{K} \mathbb{E}[\nu_k(t) | \psi_k(t) = 1], \tag{2.58}$$

while the average system throughput is defined as the ratio between the average number of packets successfully received at the BS and the average number of frames used for its transmission, i.e.,

$$\bar{T} = \frac{1}{L} \sum_{k=1}^{K} \mathbb{E}[\psi_k(t)]. \tag{2.59}$$

Note that, in our LRI scheme, each user acts in a *selfish* fashion, thus an optimal result for the global system throughput (2.59) cannot be obtained in general.

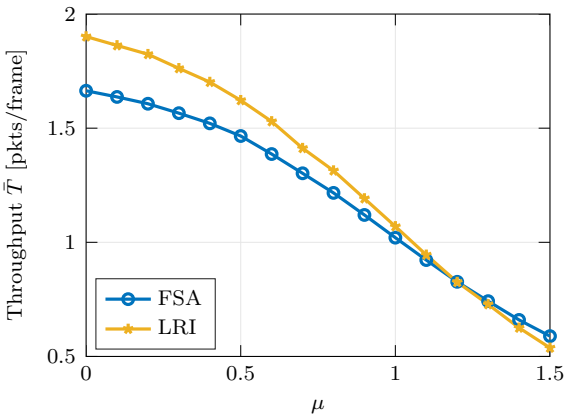

Figure 2.20: Average system throughput as a function of μ, for $\lambda = 0.05$ and $\beta = 5$.

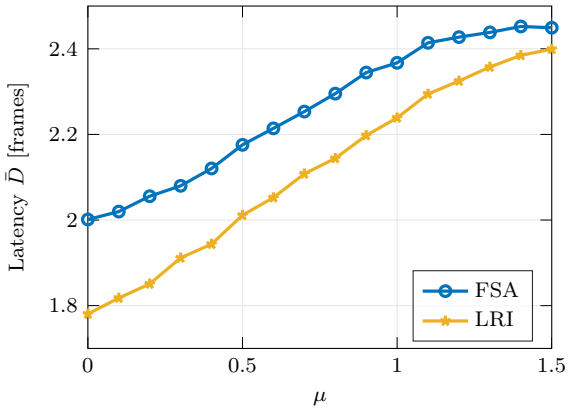

Figure 2.21: Average packet transmission time as a function of μ, for $\lambda = 0.05$ and $\beta = 5$.

Low-Traffic Scenario

We first consider a low-traffic scenario ($\mu = 0$), where packets are generated only in frame $t = 0$. The maximum number of transmission attempts is here $\beta = 5$.

Figs. 2.18 and 2.19 show the average system throughput $\bar{T}$ in packets per frame and the average packet transmission time $\bar{D}$ in frames, respectively, both as a function of the spatial events generation rate λ. The performance according to both metrics is reported for both the LRI and FSA schedulers. We observe that our LRI solution outperforms FSA with low and moderate event generation rates λ, while the performance decreases for high values of λ. Indeed, going from small to moderate event rates, the traffic correlation increases, a condition exploited by LRI, which yields a higher throughput than FSA. For high values of λ, instead, the overall generation rate increases (more packets are generated), which increases collisions and ultimately decreases the rate and increases the packet delay, as well known for these kinds of OMA schemes. Moreover, notice that, for very high values of λ, the average transmission time is reduced, due to the increase in the probability of packet expiration (maximum number of transmission attempts reached). Indeed, as LRI in general does not find the optimal maximum throughput solution, in this case, it turns out to be sub-optimal also with respect to FSA.

Throughput vs Traffic Intensity

We then consider various traffic intensity scenarios, and Fig. 2.20 and Fig. 2.21 show the performance as a function of μ, for $\lambda = 0.05$. Note that new packets are generated on average every $1/\mu$ frames, and we always generate packets at frame $t = 0$.

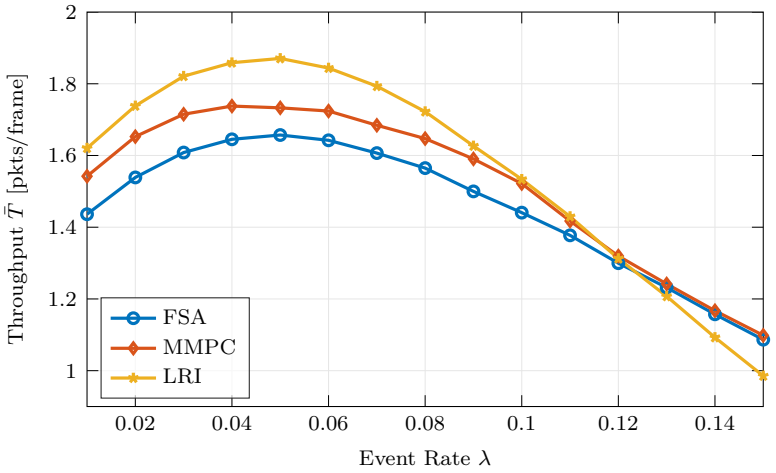

Figure 2.22: Average system throughput of LRI, min-max pairwise correlation (MMPC), and FSA, as a function of λ for $\beta = 1$.

In this scenario, whenever a packet is generated at user k while another is in its buffer, the old packet is dropped and the counter of transmission attempts restarts. We note that as μ increases, the average delay increases and the throughput decreases: this is due to the fact that more packets yield more collisions, with a throughput reduction. Moreover, we observe that the gain of LRI over FSA, in terms of both delay and throughput, vanishes as μ increases. Taking, for example, the first frames, with a higher μ, there will be new packet generations at frame $t > 0$, when some users are still handling packets generated at $t = 0$, therefore the statistics of $\boldsymbol{\nu}(t)$ is altered by the new arrivals, decorrelating the resulting traffic. Packet drops due to new arrivals have a significant impact also on the average delay: indeed, from Fig. 2.21, we observe that the curves are nearly flat for very high values of μ. In this case, LRI loses its advantage over FSA.

Single Transmission

We now consider the case $\beta = 1$, which provides a direct comparison with the MMPC scheme of [10]: in this case, all colliding packets are discarded without further retransmissions. From (2.58), we have $L = 1$, therefore the system throughput T boils down to the expected number of successful transmissions in a frame. Fig. 2.22 shows the average system throughput of our LRI, MMPC, and FSA, as a function of the event generation rate λ, for $\beta = 1$. The throughput behavior is similar to that with $\beta > 1$, providing a higher improvement for low event generation rates, while being overcome by MMPC and FSA for higher event generation rates. Indeed, we note that, although both LRI and MMPC are designed taking into account the traffic correlation, LRI has better perfor-

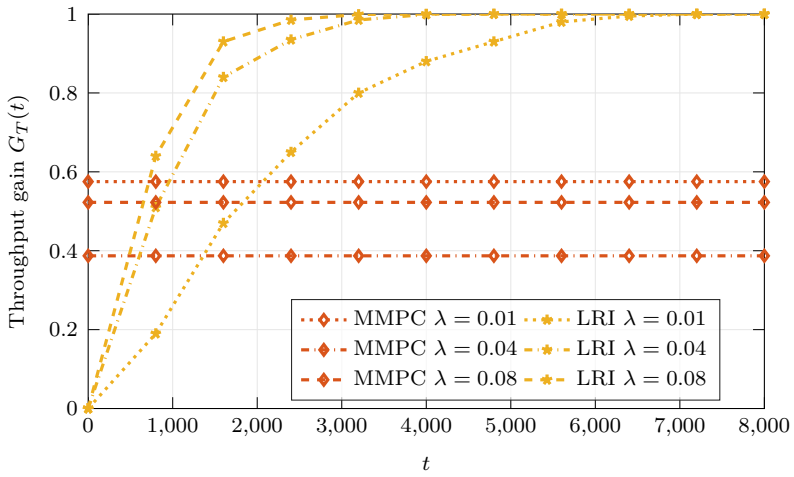

Figure 2.23: Throughput gain of LRI as a function of the frame t, for different traffic correlations ($\lambda = 0.01$, 0.04, and 0.08) and $\beta = 1$.

mance up to moderate event generation rates, as it changes the user strategies at each retransmission. Again, we observe that for high values of λ, all the compared schemes achieve a lower throughput, with LRI degrading its performance due to the selection of a suboptimal solution.

Convergence Speed for Single Transmission

Finally, we evaluate the convergence speed of the learning algorithm with $\beta = 1$, which still allows the comparison with MMPC. For the training, we set the learning rate $\alpha = 0.01$. Let us define the *throughput gain*

$$G_T(t) = \frac{T(t) - T_{\text{FSA}}}{T_{\text{LRI}} - T_{\text{FSA}}}, \tag{2.60}$$

where $T(t)$ is the throughput computed after t frames of learning, T_{FSA} is the throughput of FSA and T_{LRI} is the throughput of LRI at convergence. Note that we initialize the LRI algorithm with uniform PDFs, thus $T(0) = T_{\text{FSA}}$ and $G_T(0) = 0$. At convergence, we have $G_T(t) = 1$. Fig. 2.23 shows the throughput gain of LRI, as a function of the learning frames. For comparison purposes, we also report the throughput gain (normalized to the LRI throughput) of MMPC, obtained by replacing $T(t)$ with the MMPC throughput in (2.60). Three event generation intensities are considered, $\lambda = 0.01$, 0.04, and 0.08. We observe that convergence is faster for high values of λ, as the correlation is stronger in this case, thus the LRI iterations quickly adjust the strategy. Moreover, LRI already outperforms MMPC within about 1 000 frames. The learning process is slower for low

values of λ, requiring more than 2 000 frames to overcome the throughput achieved with MMPC.

2.5 Summary

In this chapter, we provided an overview uplink of OMA solutions and propose the PIMA protocol, a semi-GF multiple access scheme for short packet transmission, based on the knowledge of the number of users that have packets to transmit. We derived the optimal scheduling in the case of i.i.d. activations and assessed its performance with different users' activation statistics. Moreover, we provided a theoretical analysis of the correlated activation case by modeling the protocol with a PO-MDP, and we exploited the model capabilities with the GFEO algorithm. Numerical results show that PIMA and GFEO achieve extremely low latency with respect to state-of-the-art OMA multiple access solutions due to their low overhead and adapt to different activation conditions by exploiting the partial knowledge of the instantaneous traffic load.

Moving on, in the second part of the chapter, we considered the case of correlated packet generations and developed a distributed learning-based scheduler. We modeled each user as a player of a Markov game of incomplete information and, applying the LRI algorithm, we derived pure Nash equilibrium strategies for each player. Numerical results show that our proposed LRI solution outperforms the state-of-the-art correlation-based random access schemes for moderate traffic correlation and intensity.

3

Downlink Orthogonal Multiple Access in IRS-Aided Communications

In this chapter, we discuss the downlink OMA scheduling of an intelligent reflecting surface (IRS)-assisted communication scenario. First, we review the prior work on IRS-aided communications in Section 3.1, discussing both state of the art scheduling solutions and the practical constraints in the IRS networks deployments. Then, we discuss the downlink OMA system model in Section 3.2. The specific cases of TDMA **[26],** **[27]** and orthogonal frequency-division multiple access (OFDMA) **[28]** scheduling are analyzed in Section 3.3 and Section 3.4, respectively, and the numerical results are presented in Section 3.5. Finally, Section 3.6 summarizes the chapter.

3.1 IRS-Aided Communications Background

The ever-increasing growth of mobile traffic has called both academia and industry to identify and develop solutions for extending the radio spectrum beyond the crowded sub-6 GHz bands. As a result, the use of millimeter wave (mmWave) band for cellular communications has been included in the latest releases of the 3rd Generation Partnership Project (3GPP) standard, namely fifth-generation (5G) NR [66]. Moreover, Terahertz (THz) frequencies are being investigated as enablers for sixth-generation (6G) networks as well [67]. However, transmissions in the mmWave and THz bands are subject to challenging propagation conditions, mainly due to severe path loss and susceptibility to blockages [68]. To mitigate these limitations, a possible solution is to densify the network,

thus reducing the cell radius. Unfortunately, this approach was shown to be infeasible for network operators, since trenching and deploying the necessary fiber backhaul links usually has an excessive financial and logistical hurdle [69], [70]. This issue is exacerbated in remote areas, where the limited access to electrical power and the lower density of users further complicates dense network deployments from a business standpoint [71], [72]. Even worse, network densification will also inevitably increase carbon emissions due to BS management operations, with serious environmental concerns. To solve these issues, the research community has explored solutions to improve network coverage, for example using integrated access and backhaul (IAB) nodes, as also approved by the 3GPP as part of 5G NR specifications [73]. In particular, IAB allows BSs to establish wireless (rather than traditional fiber-like) backhaul links, possibly through multiple hops, to a donor, thus reducing deployment costs [74]. Still, IAB involves complex signal processing and saturation of the available resources and may be costly and energy-consuming for network operators.

IRSs are being investigated as solutions to overcome the harsh propagation conditions shown by mmWave and THz bands in a cost- and energy-efficient manner [6]. IRSs are meta-surfaces, whose radiating elements can *passively* tune the phase shift of impinging signals to favorably alter an electromagnetic field towards an intended destination. They can be configured to beamform the reflected signal virtually in any direction, hence acting as a relay to improve the signal quality without an active (power-consuming) amplification [5].

3.1.1 Multiple Access in IRS-Aided Communications

IRS-assisted downlink scheduling solutions have been widely studied in different domains, each with its own theoretical constraints. For example, in OFDMA-based user scheduling, all the users scheduled in a given time slot must be served using the same reflection coefficients, due to the lack of frequency selective beamforming capabilities at the IRS. In this context, dynamic optimization schemes, wherein the IRS configurations are adjusted over each time slot, have been studied in [75], [76]. The authors of [77] consider a two-user downlink transmission in an IRS-aided scenario over fading channels and compare the results of different basic OMA and NOMA schemes. It is found that, while NOMA appears to be the best solution, by exploiting IRS reconfiguration at each slot of the fading block, TDMA outperforms frequency division multiple access (FDMA) and approaches NOMA performance. A hybrid TDMA-NOMA approach, instead, was investigated in the uplink by [78], [79], in the context of a wireless-powered network, where users are grouped based on their channel gain. Then, users within the same group transmit in a non-

orthogonal fashion, while different groups are assigned to different time slots. Moreover, a user scheduling algorithm based on graph neural networks, able to jointly optimize the IRS configuration and the BS beamforming in downlink, was recently presented in [80]. Similarly, the authors of [81]–[83] evaluated the performance of several non-orthogonal downlink scheduling methods, such as rate-splitting multiple access (RSMA). Finally, IRSs with energy harvesting capabilities are considered in [84]. In this work, the authors propose a trade-off between the system sum rate and the IRS energetic self-sustainability, with the goal of achieving coverage flexibility and low deployment costs.

3.1.2 Practical Constraints in IRS-Aided Communications

Despite the substantial research hype, most recent studies on IRSs rely on strong assumptions that do not match real-world deployments. Specifically, a significant body of literature is based on the assumption that IRSs establish an ideal (i.e., fiber-like) control channel with the base station [85]–[87]. Instead, actual deployments are expected to feature a wireless, i.e., error-prone, IRS control, possibly implemented with low-cost technologies [88], [89]. This introduces constraints on the IRS reconfiguration period, which needs to be synchronized with the base station to beamform the signal towards the users (or user equipments (UEs)) served during the specific time slot [6], a similar research problem to scheduling in cellular networks. Nevertheless, early IRS control circuitry prototypes, which have a low power consumption (i.e., in the order of hundreds of mW), exhibit non-negligible phase-shifts reconfiguration time [90], [91], thus posing additional constraints in the system design. The prototypes described in [92] and [93] exhibit a reconfiguration time of a few tens of ms, while architectures based on field programmable gate array (FPGA) [94] achieve much lower configuration times, of the order of tens of microseconds. Moreover, the expected large number of elements of IRSs also increases the overhead (in terms of time and energy), as investigated in [95]–[97]. In any case, a constraint on the number of reconfigurations (and relative period) should be accounted to ensure system synchronization.

In this regard, it is of interest to a) investigate the level of performance degradation experienced by IRS-assisted systems when considering practical constraints, including limitations in the number of reconfigurations, and b) design algorithms that can mitigate these constraints. The limitation of the number of IRS configurations in a given time frame has been initially studied in [90], where the rate characterization of both OMA and NOMA schemes of a 2-users IRS-aided single input-single output (SISO) system was carried out under Rayleigh fading conditions.

To deal with these limitations, in this chapter, we propose OMA scheduling policies

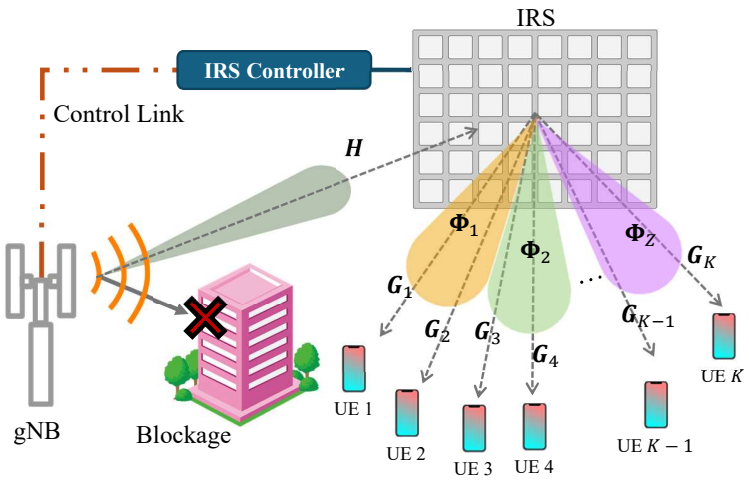

Figure 3.1: Downlink scheduling for IRS-assisted multi-user communications.

for downlink cellular transmissions based on clustering algorithms, that maximize the sum rate in IRS-assisted network deployments with practical constraints. Notably, we assume a fixed maximum number of IRS reconfigurations within a time frame and aim at optimizing both the reconfiguration time and the resulting IRS configuration(s). The limit on the number of reconfigurations sets a simple constraint on the overhead entailed by the control of the IRS. We formalize optimization problems to determine the optimal IRS configuration(s) that maximize the downlink sum rate in both the cases of TDMA and OFDMA. Specifically, we partition the users into disjoint groups and propose an algorithm that iteratively optimizes the IRS configuration for each group, as well as the relative beamformers to be used for transmission. Accordingly, we design clustering algorithms for the users, such that all users in the same cluster will adopt the same IRS configuration. The goal is to minimize the rate loss associated with a sub-optimal IRS configuration for each user in the cluster, to promote communication efficiency and reduce the overhead.

3.2 Multi-User IRS-Aided Communications

We consider downlink data transmissions for the multi-user multiple input-multiple output (MIMO) communication system shown in Fig. 3.1, wherein the transmission from the BS to K users is assisted by an IRS. The BS and the users are equipped with N_{B} and N_{U} antennas, respectively. We assume that the direct link between the BS and the users is unavailable due to a deep blockage. As a consequence, the BS transmits signals to the

f_F	RB $K-\frac{K}{F}+1$	RB $K-\frac{K}{F}+2$	…	RB $K-1$	RB K
	⋮	⋮	…	⋮	⋮
f_2	RB $\frac{K}{F}+1$	RB $\frac{K}{F}+2$	…	RB $\frac{2K}{F}-1$	RB $\frac{2K}{F}$
f_1	RB 1	RB 2	…	RB $\frac{K}{F}-1$	RB $\frac{K}{F}$
	slot 1	slot 2	···	slot $\frac{K}{F}-1$	slot $\frac{K}{F}$

Figure 3.2: Resource grid for orthogonal downlink transmissions.

users by exploiting the virtual link offered by the IRS. In this context, the IRS configuration is managed by the BS through the IRS controller, by exploiting a dedicated link between the BS and the IRS, thus avoiding the introduction of communication overhead in the BS-users downlink.

We assume that users are either static or moving slowly, which is the most typical application scenario for IRS-aided networks. Under such conditions, the channel coherence time is of the order of 10 ms [98], and assuming that perfect CSI of all users is acquired at the BS at the beginning of each frame, it is reasonable to assume that the channel remains constant throughout the whole time frame. Here we assume that the CSI is available for any IRS configuration.

The BS schedules the users in the time-frequency domain by allocating resources (referred to as resource blocks (RBs)) from a grid of K RBs. All RBs occupy a fixed bandwidth and a time slot, and flat fading is assumed in each RB. Let F be the number of RB per time slot. As shown in Fig. 3.2, each RB identifies a time-frequency resource, therefore the number of time slots (frame length) is K/F. We consider K as an integer multiple of F, with one user scheduled per RB, as in our scenario we expect that the BS-IRS channel has rank one, i.e., it has a single dominant path: this makes spatial multiplexing unfeasible. However, when higher-rank channels are available between the IRS and the BS, spatial multiplexing can be used and our approach can be suitably modified to accommodate this scenario.

Let f_i be the central frequency of the RB identified by frequency index i and an arbitrary time slot. Given the total system bandwidth W and assuming equally spaced frequencies, the set collecting the central frequencies of all RBs is defined as

$$\mathcal{F} = \left\{ f_i = f_c - \frac{W}{F} + \left(i - \frac{1}{2}\right)\frac{W}{F}, \quad i = 1, \ldots, F \right\}, \tag{3.1}$$

where f_c denotes the system's overall carrier frequency.

3.2.1 IRS Model

Each of the N_{I} elements of the IRS acts independently as an omnidirectional antenna unit that reflects the impinging electromagnetic field by introducing a tunable phase shift on the baseband-equivalent signal. We denote as $\phi_n = e^{j\theta_n}$ the reflection coefficient of the n-th IRS element, where $\theta_n \in \mathcal{P}_\theta$ is the induced phase shift, and $\mathcal{P}_\theta$ is the set of possible phase shifts. Recent works argue that continuous phase shifts are hardly implementable in practice [99]. Therefore, we consider both continuous and quantized phase shifts. While in the former case the set of phase shifts is $\mathcal{P}_\theta = [-\pi, \pi)$, in the latter we have

$$\mathcal{P}_\theta = \left\{0, \frac{2\pi}{2^b}, \ldots, \frac{2\pi(2^b-1)}{2^b}\right\}, \tag{3.2}$$

where $b > 0$ is the number of bits employed to quantize the phase shifts. To further reduce the overhead of the IRS configuration, the configuration matrix is chosen from a codebook $\mathcal{C}_{\boldsymbol{\Phi}}$, compliantly with the currently standardized initial access framework [100]. A large variety of codebooks for both near-field and far-field communication has been discussed in the literature, and the evaluation of their impact on system performance is out of the scope of this work. Note that the codebook is $\mathcal{C}_{\boldsymbol{\Phi}} = \mathcal{P}_\theta^{N_{\mathrm{I}}}$, in the general case wherein all the possible phase shift combinations are considered.

We denote with $\boldsymbol{H}(f_i) \in \mathbb{C}^{N_{\mathrm{I}} \times N_{\mathrm{B}}}$ the BS-IRS channel matrix and with $\boldsymbol{G}_k(f_i) \in \mathbb{C}^{N_{\mathrm{U}} \times N_{\mathrm{I}}}$ the channel matrix of the link between the IRS and user k at frequency f_i. We consider single-stream transmissions,[1] with $\boldsymbol{w}_k \in \mathbb{C}^{N_{\mathrm{B}} \times 1}$ and $\boldsymbol{v}_k \in \mathbb{C}^{N_{\mathrm{U}} \times 1}$ defined as the beamforming vectors at the BS and user k, respectively. Let x_k be the single-stream signal transmitted by the BS to user k; the received post-processing signal can be expressed as

$$z_k = \boldsymbol{v}_k^{\mathrm{T}} \boldsymbol{G}_k(f_i) \boldsymbol{\Phi}_k \boldsymbol{H}(f_i) \boldsymbol{w}_k x_k + \boldsymbol{v}_k^{\mathrm{T}} \boldsymbol{n}_k, \tag{3.3}$$

where $\boldsymbol{n}_k \in \mathbb{C}^{N_{\mathrm{U}} \times 1}$ represents the circularly symmetric complex Gaussian noise vector with entries having zero-mean and variance σ_n^2, while $\boldsymbol{\Phi}_k \in \mathbb{C}^{N_{\mathrm{I}} \times N_{\mathrm{I}}}$ is the IRS configuration while serving user k, i.e., a diagonal matrix defined as $\mathrm{diag}(\phi_1, \ldots, \phi_{N_{\mathrm{I}}})$. Note that for a given IRS configuration, signals at all frequencies are shifted by the same set of phase shifts, although going through different channels.

As the RBs are separated in the time-frequency domain, there is no mutual interference

[1] The assumption of single-stream transmissions is justified by the rank of the cascade channel matrix, which is likely equal to one. This conclusion comes from the combination of [101], [102] and [103], and it has been verified numerically for the considered setup.

among users. Therefore, the SNR at user k under IRS configuration $\boldsymbol{\Phi}_k$ is

$$\Gamma_k(\boldsymbol{\Phi}_k, f_i) = \frac{|\boldsymbol{v}_k^{\mathrm{T}} \boldsymbol{G}_k(f_i) \boldsymbol{\Phi}_k \boldsymbol{H}(f_i) \boldsymbol{w}_k|^2 \sigma_x^2}{|\boldsymbol{v}_k|^2 \sigma_n^2}, \tag{3.4}$$

where σ_x^2 is the power of the transmitted signal. User k also attains the achievable rate

$$R_k(\boldsymbol{\Phi}_k, f_i) = \log_2 \left[1 + \Gamma_k(\boldsymbol{\Phi}_k, f_i)\right]. \tag{3.5}$$

3.2.2 Configuration and User Scheduling

In general, different IRS configurations should be adopted for each user to maximize its achievable rate (3.5) based on its position in the cell and on its channel conditions. However, $\boldsymbol{\Phi}$ is not frequency-selective, i.e., its configuration is the same at each RB in the same time slot. Moreover, we here impose a constraint on the number of IRS reconfigurations per time frame, with the goal of either limiting the reconfiguration and reducing the overhead, or accounting for practical limitations that might arise in realistic deployments. This limitation usually leads to an achievable rate degradation as sub-optimal IRS configurations could be adopted to serve some users.

To mitigate this effect, we formulate a constrained discrete optimization problem, wherein we impose a limit on the re-configurations within a time frame to a maximum number of $Z \leq K/F$. We remark that, typically, the BS communicates a (possibly new) IRS configuration during each transmission time interval (TTI). The block-static constraint that we introduce reduces such overhead by a factor $\frac{ZF}{K} \leq 1$. On the downside, achieving this objective usually leads to SNR degradation as sub-optimal IRS configurations might be adopted for some users. Within this time frame the BS serves the K users by splitting them into Z disjoint subsets $\mathcal{U}_1, \ldots, \mathcal{U}_Z$, each with cardinality $\alpha_z F$, with $\alpha_z \in \mathbb{N}$, for $z = 1, \ldots, Z$, and assigning each user to one RB. While serving the user in subset $\mathcal{U}_z$ the IRS configuration is fixed to $\boldsymbol{\Phi}^{(z)}$, and α_z represents the number of slots wherein $\boldsymbol{\Phi}^{(z)}$ is kept. Let $\mathcal{I} = \{\boldsymbol{\Phi}^{(1)}, \boldsymbol{\Phi}^{(2)}, \ldots, \boldsymbol{\Phi}^{(Z)}\}$ be the set of IRS configurations corresponding to subsets $\mathcal{U}_1, \ldots, \mathcal{U}_Z$, let $f^{(k)}$ be the frequency assigned to user k and $\mathcal{Y} = \{f^{(1)}, \ldots, f^{(K)}\}$. Under the aforementioned constraints, the system sum rate is given by

$$R(\mathcal{U}_1, \ldots, \mathcal{U}_Z, \mathcal{Y}, \mathcal{I}) = \sum_{z=1}^{Z} \sum_{k \in \mathcal{U}_z} R_k(\boldsymbol{\Phi}^{(z)}, f^{(k)}). \tag{3.6}$$

In the following sections, we propose clustering-based sum-rate optimization algorithms. In particular, Section 3.3 focuses on the particular case of $F = 1$, which corresponds to

the TDMA framework. Then the generalization to OFDMA is investigated in Section 3.4.

3.3 Downlink TDMA Scheduling

In this section, the special case of downlink TDMA scheduling with reconfiguration constraints is investigated. In this framework $F = 1$, therefore the users must be scheduled in the time domain only. Note that part of the constraints introduced in Section 3.2 can be neglected without loss of generality. Indeed, the absence of frequency-selectivity of the IRS does not imply any scheduling constraint. Moreover, throughout all the section, we assume that the IRS configuration codebook is $\mathcal{C}_{\mathbf{\Phi}} = \mathcal{P}_{\theta}^{N_{\mathrm{I}}}$, which eventually includes the case of b-bits quantized phase shifts. We investigate the adoption of clustering techniques to group the users into subsets $\mathcal{U}_1, \ldots, \mathcal{U}_Z$, and assign configurations $\mathcal{I} = \{\mathbf{\Phi}^{(1)}, \mathbf{\Phi}^{(2)}, \ldots, \mathbf{\Phi}^{(Z)}\}$ to each cluster. In particular, we investigate two clustering techniques:

1. distance-based clustering, which adjusts the cluster configuration based on the distance with the optimal IRS configuration of each user in the cluster;

2. capacity-based clustering, which adjusts the cluster configuration to maximize the sum rate and/or the user fairness. Specifically, we propose three clustering algorithms. The first, named capacity-weighted clustering (CWC), iteratively adjusts the clusters' centroids weighting the points in each cluster by the rate achieved by each user in the cluster, therefore favoring the best users and maximizing the sum rate. The second, named one-shot capacity-based clustering (OSCBC), is a low-complexity approach where the centroids are simply the optimal configurations of the users experiencing the highest SNR in each cluster, without considering the impact of the remaining users. Finally, the inverse capacity-weighted clustering (ICWC) algorithm promotes fairness among the users by weighting the points in the clusters by the inverse of the users' achievable rate.

Numerical results depicting the performance of the distance- and capacity-based clustering in different IRS-assisted scenarios are finally presented.

3.3.1 TDMA Sum Rate Optimization Problem

As already discussed, we impose a constraint on the number of IRS reconfigurations per time frame, with the goal of either limiting the reconfiguration or accounting for practical limitations that might arise in realistic deployments. In the particular case of TDMA

we can omit the frequency indexes (i.e., variables i, f_i), and the constraints discussed in Section 3.2.2 are simplified into the following conditions:

1. at most Z IRS reconfigurations can occur per time frame;
2. the BS serves K users by partitioning them into Z disjoint subsets $\mathcal{U}_1, \ldots, \mathcal{U}_Z$, $Z \leq K$;
3. for each user in $\mathcal{U}_z$, the same IRS configuration $\boldsymbol{\Phi}^{(z)}$ is used, i.e., $\boldsymbol{\Phi}_k = \boldsymbol{\Phi}^{(z)}, \forall\, k \in \mathcal{U}_z, \forall\, 1 \leq z \leq Z$.

The sum rate can be therefore simplified from (3.6) as

$$R(\mathcal{U}_1, \ldots, \mathcal{U}_Z, \mathcal{I}) = \sum_{z=1}^{Z} \sum_{k \in \mathcal{U}_z} R_k(\boldsymbol{\Phi}^{(z)}), \tag{3.7}$$

and the optimization problem is then formulated as

$$\max_{\mathcal{U}_1, \ldots, \mathcal{U}_Z, \mathcal{I}} \quad R(\mathcal{U}_1, \ldots, \mathcal{U}_Z, \mathcal{I}), \tag{3.8a}$$

$$\text{s.t.} \quad \angle\big[\boldsymbol{\Phi}^{(z)}\big]_{n,n} \in \mathcal{P}_\theta, \quad \forall\, n, z. \tag{3.8b}$$

Problem (3.8) determines the optimal grouping strategy for the users subsets $\mathcal{U}_1, \ldots, \mathcal{U}_Z$, and assigns the best IRS configuration accordingly. Therefore, (3.8) incorporates both the continuous aspect of the configuration optimization and the combinatorial aspect of the user assignment problem and can be thus classified as a MINLP problem. Moreover, the following theorem holds

Theorem 3. *The sum rate maximization problem (3.8) is NP-complete.*

Proof. First, we observe that the problem falls within the general NP class. This happens since if (3.8) is solved to find $\mathcal{U}_1, \ldots, \mathcal{U}_Z, \mathcal{I}$, both the sum rate and the phase-shift constraints (3.8b) can be verified in polynomial time.

To prove the NP-hardness, let us set $\mathcal{I}$ and consider the simplified problem

$$\max_{\mathcal{U}_1, \ldots, \mathcal{U}_Z} \quad R(\mathcal{U}_1, \ldots, \mathcal{U}_Z, \mathcal{I}). \tag{3.9}$$

This problem can be viewed as a multi-knapsack problem, with different clusters $\mathcal{U}_1, \ldots, \mathcal{U}_Z$, as knapsacks, and the goal being the maximization of the total system rate. This is known

to be NP-hard, as it generalizes the classic knapsack problem. The original sum rate maximization problem (3.8), where we consider the additional degrees of freedom of the IRS configurations, remains NP-hard, thus giving NP-completeness. □

Given the inherent problem complexity, we adopt heuristic *clustering* algorithms to obtain approximated, though close-to-optimal, solutions, as described in Section 3.3.2.

3.3.2 Heuristic Sum Capacity Maximization

In this section, we provide heuristic solutions to (3.8). First, we present two clustering-based approaches to identify and group users with a similar optimal IRS configuration. Then, we solve the scheduling problem on the identified clusters with a TDMA approach [104]. We compute the users' clusters by first estimating the optimal individual IRS configurations, denoted as $\boldsymbol{\Phi}_k^*$, $1 \leq k \leq K$, i.e., the IRS configurations leading to the maximum rate for each user k. These configurations would solve (3.8) for $Z = K$, as in this case all users are served in a TDMA fashion and with their optimal IRS configuration. The phase coefficients of the optimal IRS configuration matrices are then chosen as the initial points of a procedure leveraging clustering algorithms in the N_{I}-dimensional space.

Optimal Individual IRS Configurations

In MIMO systems, both the BS and the users adopt properly tuned beamformers to match the signal transmissions and receptions to the spatial direction providing the highest channel gain [6]. For the optimization of the IRS configuration of each individual user, we adopt a procedure similar to that presented in [97], focusing on single-stream transmissions and, without loss of generality, on user k.

For a given IRS configuration, the optimal beamforming vectors $\boldsymbol{v}_k$ and $\boldsymbol{w}_k$ coincide with the singular vectors corresponding to the highest singular value of the wireless channel matrix. In particular, we calculate the singular value decomposition (SVD) of the overall cascade channel matrix

$$\boldsymbol{G}_k \boldsymbol{\Phi}_k \boldsymbol{H} = \boldsymbol{U} \boldsymbol{\Sigma} \boldsymbol{V}^{\dagger}, \tag{3.10}$$

where the right and left singular vectors of $\boldsymbol{G}_k \boldsymbol{\Phi}_k \boldsymbol{H}$ are the columns of $\boldsymbol{V}$ and $\boldsymbol{U}$, and the corresponding singular values are the diagonal entries of $\boldsymbol{\Sigma}$.

In our formulation, the IRS configuration $\boldsymbol{\Phi}_k$ is one of the optimization variables. In-

deed, given $\boldsymbol{v}_k$ and $\boldsymbol{w}_k$, we can solve

$$\boldsymbol{\Phi}_k^* = \underset{\boldsymbol{\Phi}_k}{\operatorname{argmax}}\, R_k(\boldsymbol{\Phi}_k), \tag{3.11a}$$

$$\text{s.t.} \quad \angle[\boldsymbol{\Phi}_k]_{n,n} \in \mathcal{P}_\theta, \quad n = 1, \ldots, N_{\mathrm{I}}\,, \tag{3.11b}$$

where R_k is the achievable rate of user k, $1 \leq k \leq K$, according to (3.5). The derivation of the optimal IRS configuration of user k requires the alignment of the channel phase coefficients. According to [105], the cascade channel can be expressed as

$$\boldsymbol{v}_k^{\mathrm{T}} \boldsymbol{G}_k \boldsymbol{\Phi}_k \boldsymbol{H} \boldsymbol{w}_k = \operatorname{vec}\left(\boldsymbol{v}_k^{\mathrm{T}} \boldsymbol{G}_k \boldsymbol{\Phi}_k \boldsymbol{H} \boldsymbol{w}_k\right) = \left(\boldsymbol{w}_k^{\mathrm{T}} \boldsymbol{H}^{\mathrm{T}} \diamond \boldsymbol{v}_k^{\mathrm{T}} \boldsymbol{G}_k\right) \operatorname{diag}(\boldsymbol{\Phi}_k) \tag{3.12}$$

where $\diamond$ denotes the Khatri-Rao product operator and $\operatorname{diag}(\boldsymbol{\Phi}_k)$ return the column vector with all the elements in the diagonal of $\boldsymbol{\Phi}_k$. Then, it is sufficient to observe that the SNR is maximized when the phase shifts introduced by the IRS are aligned with the phase shifts accumulated along the various paths, i.e.,

$$\theta_{k,n} = -(\angle\left[\left(\boldsymbol{w}_k^{\mathrm{T}} \boldsymbol{H}^{\mathrm{T}} \diamond \boldsymbol{v}_k^{\mathrm{T}} \boldsymbol{G}_k\right)\right]_n), \quad \forall n. \tag{3.13}$$

Note that, in general, we need to know the estimated phase shift of each component resulting from the Khatri-Rao product in (3.13), rather than the exact phase coefficients of $\boldsymbol{H}$ and $\boldsymbol{G}_k$. Moreover, as pointed out in [105], for structured channel models adopted at mmWaves, where multipath scattering is sparse and propagation is often dominated by strong specular components, the estimation of the separated channel matrices $\boldsymbol{H}$ and $\boldsymbol{G}_k$ can be simply accommodated by optimizing a limited number of parameters.

Taking into account the possible quantization, the optimal phase shifts are given by

$$\angle[\boldsymbol{\Phi}_k^*]_{n,n} \leftarrow \underset{\psi \in \mathcal{P}_\theta}{\operatorname{argmin}} \left(\angle e^{j(\theta_{k,n} - \psi)}\right), \quad \forall n. \tag{3.14}$$

To overcome the interdependence between optimal IRS configurations and beamforming vectors, we propose an iterative alternate optimization approach. We first estimate the optimal beamforming vectors for a given IRS configuration using (3.10). Then, we plug the derived beamformers into (3.11a), and obtain the corresponding optimal IRS configuration. We repeat this two-step procedure until convergence, which, for practical purposes, is assumed to be reached when the difference between the achievable rates R_k, $\forall k$, in two consecutive iterations is lower than a tolerance $\nu > 0$. This procedure is summarized in Algorithm 3.1, where t is the iteration index. The number of iterations grows

Algorithm 3.1 Iterative Alternate IRS Optimization

Require: $\boldsymbol{G}_k, \boldsymbol{H}$
Ensure: $\boldsymbol{\Phi}_k^*$
1: $t \leftarrow 0$
2: $\boldsymbol{v}_k, \boldsymbol{w}_k \leftarrow \mathbf{1}$
3: **repeat**
4: $\quad \theta_{k,n} \leftarrow -(\angle \left[\left(\boldsymbol{w}_k^{\mathrm{T}} \boldsymbol{H}^{\mathrm{T}} \diamond \boldsymbol{v}_k^{\mathrm{T}} \boldsymbol{G}_k \right) \right]_n), \quad \forall n$
5: $\quad \angle[\boldsymbol{\Phi}_{k,t}]_{n,n} \leftarrow \mathrm{argmin}_{\psi \in \mathcal{P}_\theta} (\angle e^{j(\theta_{k,n} - \psi)}), \quad \forall n$
6: $\quad \boldsymbol{U}, \boldsymbol{\Sigma}, \boldsymbol{V}^\dagger \leftarrow$ SVD of $\boldsymbol{v}_k^{\mathrm{T}} \boldsymbol{G}_k \boldsymbol{\Phi}_{k,t} \boldsymbol{H} \boldsymbol{w}_k$
7: $\quad \boldsymbol{v}_k \leftarrow$ column of $\boldsymbol{V}$ corresponding to the largest singular value
8: $\quad \boldsymbol{w}_k \leftarrow$ column of $\boldsymbol{U}$ corresponding to the largest singular value
9: $\quad t \leftarrow t + 1$
10: **until** $|R_k(\boldsymbol{\Phi}_{k,t}) - R_k(\boldsymbol{\Phi}_{k,t-1})| < \nu$
11: $\boldsymbol{\Phi}_k^* \leftarrow \boldsymbol{\Phi}_{k,t}$

with the number of antennas and IRS phase shifters. However, from preliminary simulations, and based on the set of parameters we considered (see Section 3.5), convergence is typically reached in less than 10 iterations.

Clustering-based TDMA Scheduling

For an approximated but close-to-optimal solution to (3.8), we resort to a clustering-based approach. Our proposed clustering algorithms estimate both the subsets of users $\mathcal{U}_1, \ldots, \mathcal{U}_Z$, and the relative set of IRS configurations $\mathcal{I}$. We operate on the *phase vector space*, i.e., the points to be clustered are identified by the IRS phase shifts vector $[\angle\phi_1, \ldots, \angle\phi_{N_\mathrm{I}}]^{\mathrm{T}} = [\theta_1, \ldots, \theta_{N_\mathrm{I}}]^{\mathrm{T}}$, which maps each IRS configuration $\boldsymbol{\Phi}$ to a point in $[-\pi, \pi)^{N_\mathrm{I}}$. In case of quantized phase shifts, the phase vector space is a lattice in the continuous space $[-\pi, \pi)^{N_\mathrm{I}}$.

The general clustering-based procedure works as follows:

1. find $\boldsymbol{\Phi}_k^*$, $\forall k$, i.e., the optimal individual IRS configurations for each user as in Section 3.3.2;

2. build user subsets $\mathcal{U}_z$, $z = 1, \ldots, Z$, by using a clustering algorithm, according to Sections 3.3.3 and 3.3.4;

3. assign $\boldsymbol{\Phi}^{(z)}$ to all users $\in \mathcal{U}_z$.

The core idea of this procedure is to use clustering algorithms to group users and assign the respective IRS configurations, which are mapped to the *centroid* of the cluster. In

the case of quantized phase shifts, once the clustering procedure is performed, clusters may share the same centroid and be merged. Therefore, Z represents the *maximum number of clusters*, not the effective number. Moreover, we remark that steps 2-3 do not rely on the perfect CSI assumption, as the grouping strategy and the individual optimization of step 1 are performed independently. Nevertheless, in the case of imperfect CSI, the estimated individual optimal configurations may differ from the actual optimal configurations, leading to a sub-optimal grouping as well. The multi-user scenario with imperfect CSI has been studied in [106], where a single IRS configuration is optimized to maximize the system weighted sum rate taking into consideration the imperfect CSI of all users jointly.

In the following, we propose different techniques to build the clusters based on either a distance metric (Section 3.3.3) or the achievable rate (Section 3.3.4).

3.3.3 Distance-Based Clustering Algorithms

The class of distance-based clustering contains methods that group data points based on their similarity or dissimilarity according to a distance metric. This approach has several advantages, including the efficiency in handling large datasets, and the flexibility to adapt to many different scenarios of interest. However, distance-based clustering can be sensitive to the choice of the distance metric (which depends on the nature of the data and the clustering problem), and the initialization values. Moreover, in our specific case, it does not take into account the achievable rate, which is not directly related to the distance among the points in the phase vector space.

Since the scalar field is the range $[-\pi, \pi)$, the adopted distance has to take into account the circularity of data. However, the convergence to a local minimum of the majority of the clustering algorithm is guaranteed only if the points to be clustered belong to an Euclidean space. For all distance-based algorithms we thus define the bijective mapping $f : \mathcal{P}_{\theta}^{N_\mathrm{I}} \to \mathbb{R}^{2N_\mathrm{I}}$ as

$$f(\boldsymbol{\theta}) = f([\theta_1, \ldots, \theta_{N_\mathrm{I}}]) = [\cos(\theta_1), \sin(\theta_1), \ldots, \cos(\theta_{N_\mathrm{I}}), \sin(\theta_{N_\mathrm{I}})]\,, \tag{3.15}$$

and then we define the pairwise *distance* between two generic IRS configurations $\boldsymbol{\alpha}, \boldsymbol{\beta}$ as

$$\delta(\boldsymbol{\alpha}, \boldsymbol{\beta}) = ||f(\boldsymbol{\alpha}) - f(\boldsymbol{\beta})||, \tag{3.16}$$

i.e., the Euclidean distance between the mapping on the unit N_I-sphere of their respective phase vectors. In the following, with a slight abuse of notation, $f(\boldsymbol{\Phi})$ maps the phases of

the complex entries in the diagonal of $\mathbf{\Phi}$ as in (3.15), and $\delta(\mathbf{\Phi}_1, \mathbf{\Phi}_2)$ denotes the pairwise distance between the phases of the elements in the diagonal of matrices $\mathbf{\Phi}_1$ and $\mathbf{\Phi}_2$. The sum of squared distances is defined as

$$J(\mathcal{U}_1, \ldots, \mathcal{U}_Z, \mathcal{I}) = \sum_{z=1}^{Z} \sum_{k \in \mathcal{U}_z} \delta \left(\mathbf{\Phi}_k^*, \mathbf{\Phi}^{(z)} \right)^2, \tag{3.17}$$

and the distance-based clustering schemes aim at solving

$$\min_{\mathcal{U}_1, \ldots, \mathcal{U}_Z, \mathcal{I}} \quad J(\mathcal{U}_1, \ldots, \mathcal{U}_Z, \mathcal{I}), \qquad \text{s.t.} \quad (3.8\text{b}). \tag{3.18}$$

We consider and compare some of the most popular distance-based clustering algorithms, namely, K-means, agglomerative hierarchical clustering, and K-medoids.

K-means. K-means (KM) clustering [107] aims at finding Z disjoint clusters minimizing the within-cluster squared Euclidean distances. Here, we consider the generalized Lloyd algorithm [108], which randomly selects Z points in the space of phase vectors as the initial centroids. In our setup, to ensure optimal performance when $Z = K$, we force the algorithm initialization to a random selection among the phase vectors of the optimal individual IRS configurations derived in Section 3.3.2. Then, in the *assignment step* KM assigns each data point to the closest centroid, according to the specified distance metric. In the subsequent *update step*, the set of centroids is re-computed as the average of the data points that belong to each cluster. These steps are repeated until either convergence or a maximum number of iterations $I_{\max}^{\text{KM}}$ is reached.

Agglomerative Hierarchical clustering. The agglomerative hierarchical clustering (HC) [109] partitions a set of data points into disjoint clusters by iteratively merging points into clusters until a target number of partitions is met. In our setup, clusters are initialized as the optimal phase vectors, which thus act as the respective centroids. Then, the average distance between all pairs of data points in any pair of clusters is evaluated. The closest pair of clusters are merged into a new single cluster, whose centroid is computed as the mean of its data points. The procedure is repeated until the number of clusters is Z.

K-medoids. K-medoids (KMed) [110] is a clustering technique similar to KM, but instead of the mean of the data points within each cluster, it uses the medoid, i.e., the data point that is closest to the center of the cluster. In our setup, we consider the partition around medoids (PAM) method [111], which starts by randomly selecting Z medoids among the optimal phase vectors and assigns each point to the cluster with the closest medoid. In each iteration, the algorithm evaluates potential *swaps* of medoids with non-medoids. A

swap is accepted only if it results in a lower value of the sum of the squared distances to all other data points within the same cluster. The algorithm continues until the medoids no longer change.

Theorem 4. *The presented distance-based clustering techniques converge to a local minimum of (3.17).*

Proof for KM (LLoyd). In the assignment step each user k is assigned to the cluster z that minimizes the squared distance $\delta\left(\mathbf{\Phi}_k^*, \mathbf{\Phi}^{(z)}\right)^2$. This guarantees that the total sum $J(\mathcal{U}_1, \ldots, \mathcal{U}_Z, \mathcal{I})$ does not increase. Then, the update step, recalculating $\mathbf{\Phi}^{(z)}$ as the average $\mathbf{\Phi}_k^*$ within each cluster, yields the minimization of the intra-cluster sum of squared distances $\sum_{k\in\mathcal{U}_z} \delta\left(\mathbf{\Phi}_k^*, \mathbf{\Phi}^{(z)}\right)^2$, for all z. Therefore, the conditions of [112, Lemma 5] are satisfied, and the convergence to a local minimum is assured. [2] □

Proof for Agglomerative HC. At each step, the merge between clusters minimizes the increase in the total intra-cluster sum of squared distances. This is equivalent to choosing the merge that results in the smallest increase in $J(\mathcal{U}_1, \ldots, \mathcal{U}_Z, \mathcal{I})$. Then, as for KM in the update step, the average of the data points minimizes $\sum_{k\in\mathcal{U}_z} \delta\left(\mathbf{\Phi}_k^*, \mathbf{\Phi}^{(z)}\right)^2$, for all z. Once the desired number of clusters Z the convergence to a local minimum is reached. □

Proof for K-Medoids (PAM). Since in each iteration, a swap is performed only when it leads to a lower value of the intra-cluster sum of squares, $J(\mathcal{U}_1, \ldots, \mathcal{U}_Z, \mathcal{I})$ is non-increasing over the iterations. Given the finite number of data points and possible configurations, the algorithm is guaranteed to converge to a configuration where no swap can further decrease the objective function, thus reaching a local minimum. □

3.3.4 Capacity-Based Clustering Algorithms

The distance-based clustering techniques presented in Section 3.3.3 do not directly take into account the actual rate achievable by the users, which is a crucial factor for the sum rate maximization (3.8). Thus, in the following we propose original capacity-based clustering algorithms that go beyond the state of the art, namely CWC (Section 3.3.4), OSCBC (Section 3.3.4), and ICWC (Section 3.3.4).

Capacity-Weighted Clustering (CWC)

Similarly to distance-based clustering, also CWC proceeds iteratively. However, the stopping condition is based on the variation of the sum rate of each cluster, rather than

[2] Note that [112] does not specify the iterations needed to converge, which could be large in the case of highly dimensional spaces, therefore, in practice, we limit the maximum number of iterations to $I_{\max}^{\mathrm{KM}}$.

on the distance between the centroids. In this approach, the clustering algorithm itself weighs the users based on their achievable rate, so that the parameters of the resulting clusters are closer to the ones preferred by the users with higher rates, thus promoting the maximization of the sum rate.

Let $\boldsymbol{\Phi}_i^{(z)}$ be the IRS configuration of cluster $\mathcal{U}_{z,i}$ at iteration i. Users are initially sorted in decreasing order of achievable rate. The algorithm then selects the Z users providing the highest achievable rate based on the expression in (3.5) with their optimal IRS configurations. Without loss of generality, we let $z = 1, \dots, Z$, be the index of those users, and set $\boldsymbol{\Phi}_1^{(z)} = \boldsymbol{\Phi}_z^*, \forall\ 1 \leq z \leq Z$, as the centroids of the initial clusters $\mathcal{U}_{1,0}, \dots, \mathcal{U}_{Z,0}$. In the following, for simplicity, we denote with $z_{k,i}$ the cluster such that $k \in \mathcal{U}_{z,i}$. Each user $k > Z$ is assigned to the cluster whose centroid provides the lowest rate difference with respect to its ideal configuration. Let $R_k(\boldsymbol{\Phi}_k^*)$ be the maximum achievable rate of user k, obtained from the solution of problem (3.1). user k is assigned to cluster

$$z_{k,i} = \underset{z}{\operatorname{argmin}}[R_k(\boldsymbol{\Phi}_k^*) - R_k(\boldsymbol{\Phi}_i^{(z)})], \tag{3.19}$$

where $R_k(\boldsymbol{\Phi}_i^{(z)})$ is the rate achieved by user k adopting the IRS configuration of cluster z at iteration i. Note that, despite being always non-negative, the rate difference in (3.19) cannot be considered a distance metric as, in general, it does not satisfy the triangle inequality.

However, the following result proves that increasing distances from the optimal configuration correspond to lower rates, thus supporting the use of the rate difference as a clustering criterion.

Theorem 5. *Given the optimal configuration $\boldsymbol{\Phi}_k^*$, the rate $R_k(\boldsymbol{\Phi})$ is monotonically decreasing with respect to the magnitude of any phase shifts error ϵ.*

Proof. Let ϵ be an arbitrary error phase shift $\in [-\pi, \pi]$, and consider the configuration $\boldsymbol{\Phi}_k^\epsilon = \boldsymbol{\Phi}_k^* \boldsymbol{E}$, where $\boldsymbol{E} = \operatorname{diag}(e^{j\epsilon}, 1, \dots, 1)$, i.e., the sub-optimal configuration where only the first IRS element is affected by the error ϵ. Assuming without loss of generality that $N_\mathrm{B} = N_k = 1$ and $\sigma_x = \sigma_n = 1$, the rate $R_k(\boldsymbol{\Phi}_k^\epsilon)$ is proportional to $\Gamma_k(\boldsymbol{\Phi}_k^\epsilon)$ when using configuration $\boldsymbol{\Phi}_k^\epsilon$. The SNR $\Gamma_k(\boldsymbol{\Phi}_k^\epsilon)$ reads

$$\Gamma_k(\boldsymbol{\Phi}_k^\epsilon) = |\boldsymbol{g}_k \boldsymbol{\Phi}_k^* \boldsymbol{E} \boldsymbol{h}|^2 = |[\boldsymbol{g}_k]_1 [\boldsymbol{\Phi}_k^* \boldsymbol{E}]_{1,1} [\boldsymbol{h}]_1 + A|^2\,, \tag{3.20}$$

where $A = \sum_{n=2}^{N_\mathrm{I}} [\boldsymbol{g}_k]_n [\boldsymbol{\Phi}_k^*]_{n,n} [\boldsymbol{h}]_n$. Since $\boldsymbol{\Phi}_k^*$ is the optimal configuration, it satisfies (3.13).

It follows that $A \in \mathbb{R}^+$ and that (3.20) can be further manipulated into

$$\Gamma_k(\boldsymbol{\Phi}_k^\epsilon) = |[\boldsymbol{g}_k]_1||[\boldsymbol{h}]_1|e^{j\epsilon} + A|^2 = A^2 + (|[\boldsymbol{g}_k]_1||[\boldsymbol{h}]_1|)^2 + 2A|[\boldsymbol{g}_k]_1||[\boldsymbol{h}]_1|\cos(\epsilon). \quad (3.21)$$

Finally, it suffices to evaluate the sign of the derivative of $\Gamma_k(\boldsymbol{\Phi}_k^\epsilon)$ with respect to the error ϵ

$$\frac{\partial \Gamma_k(\boldsymbol{\Phi}_k^\epsilon)}{\partial \epsilon} = -2A|[\boldsymbol{g}_k]_1||[\boldsymbol{h}]_1|\sin(\epsilon), \quad (3.22)$$

and observe that $\Gamma_k(\boldsymbol{\Phi}_k^\epsilon)$, and therefore $R_k(\boldsymbol{\Phi}_k^\epsilon)$, is strictly decreasing for $0 < |\epsilon| \leq \pi$. □

After all the remaining users have been assigned to the corresponding clusters, the coordinates of the centroids are updated. At iteration $i+1$, the new IRS configuration (centroid) of cluster $\mathcal{U}_{z,i+1}$ is computed as the average of the data points in the cluster, weighted by their achievable rate, i.e.,

$$\boldsymbol{\Phi}_{i+1}^{(z)} = f^{-1}\left(\frac{\sum_{k\in\mathcal{U}_z} f(\boldsymbol{\Phi}_k^*)R_k(\boldsymbol{\Phi}_k^*)}{\sum_{k\in\mathcal{U}_z} R_k(\boldsymbol{\Phi}_k^*)}\right). \quad (3.23)$$

Also, in the case of phase shift quantization, an additional approximation step must be performed as

$$\angle[\boldsymbol{\Phi}_{i+1}^{(z)}]_{n,n} \leftarrow \underset{\psi\in\mathcal{P}_\theta}{\operatorname{argmin}} \left(\angle e^{j(\angle[\boldsymbol{\Phi}_{i+1}^{(z)}]_{n,n}-\psi)}\right), \quad \forall n. \quad (3.24)$$

This two-step procedure is repeated until convergence, which is reached when the rate difference between two consecutive iterations is lower than the sum rate tolerance $\mu > 0$.

The rationale behind the algorithm is that, based on the initial centroid assignment, the users experiencing the best channel conditions, i.e., those dominating the system sum rate, are initially served with their optimal (individual) IRS configurations. Even after the adjustment of the clusters, these users will always get the largest weight coefficient within the cluster. The remaining users, instead, will be penalized by the configuration constraints, but their impact on the sum rate will be limited. The whole workflow of the CWC procedure is summarized in Algorithm 3.2.

One-Shot Capacity-Based Clustering (OSCBC)

The main drawback of CWC presented in Section 3.3.4 is that it requires solving problem (3.19) at each iteration, relative to all the users in each cluster. Considering massive MIMO systems, the CWC procedure could become exceedingly complex, as it requires the SVD computation of extremely large matrices. Therefore, we propose another lower-complexity clustering algorithm, denoted as OSCBC.

Algorithm 3.2 CWC Algorithm

Require: Z, $\boldsymbol{H}$, $\boldsymbol{G}_k$, $\forall k$
Ensure: $\mathcal{U}_1, \ldots, \mathcal{U}_Z$, $\mathcal{I}$
1: Compute $\boldsymbol{\Phi}_k^*, \forall k$ with the procedure of Algorithm 3.1
2: Sort the users in decreasing order of $R_k(\boldsymbol{\Phi}_k^*)$
3: Select the Z users providing the highest $R_k(\boldsymbol{\Phi}_k^*)$,
4: Set $\boldsymbol{\Phi}_1^{(z)} = \boldsymbol{\Phi}_k^*$, $z = 1, \ldots, Z$ as the initial centroids.
5: **repeat**
6: **for** each user k
7: $z_{k,i} \leftarrow \text{argmin}_z \, R_k(\boldsymbol{\Phi}_k^*) - R_k(\boldsymbol{\Phi}_i^{(z)})$
8: **end for**
9: **for** each cluster z
10: Compute $\boldsymbol{\Phi}_{i+1}^{(z)}$ as per (3.23), (3.24)
11: **end for**
12: $i \leftarrow i + 1$
13: **until** $\left| \sum_{k \in \mathcal{U}_z} R_k(\boldsymbol{\Phi}_i^{(z)}) - \sum_{k \in \mathcal{U}_z} R_k(\boldsymbol{\Phi}_{i-1}^{(z)}) \right| < \mu$
14: Assign $\boldsymbol{\Phi}^{(z)}$ to all $k \in \mathcal{U}_z$.

As in CWC, also in OSCBC a) the users are sorted in decreasing order of achievable rate; b) the Z IRS configurations of the Z users experiencing the highest rates are chosen as initial centroids for the clusters; and c) the remaining users are assigned to the closest centroid in terms of circular distance, as per (3.16). Then, compared to CWC, instead of recomputing the coordinates of the centroids at each iteration until convergence, the algorithm stops right after the initial association. Therefore, with OSCBC the computed centroids are the optimal configurations relative to the Z users achieving the highest individual rate, which provides sub-optimal (non-optimized) performance for the rest of the users in the clusters.

Inverse Capacity-Weighted Clustering (ICWC)

The CWC algorithm is designed to optimize the rate of the users experiencing the best channel conditions and is unfair to the other users in the system, which may use sub-optimal IRS configurations. Therefore, we propose an additional variation of CWC, named ICWC, with the goal of achieving higher fairness among the users in the system. In ICWC, while the cluster association principle of (3.19) is preserved, the initial condition is reversed. Specifically:

1. users are sorted in increasing order of achievable rate;
2. the initial configurations of the clusters $\boldsymbol{\Phi}_1^{(z)} = \boldsymbol{\Phi}_z^*$, $z = 1, \ldots, Z$, are based on the

Table 3.1: Computational complexity of distance-based vs. capacity-based clustering.

Clustering algorithm	Computational complexity
KM (Lloyd)	$O(IZKN_{\mathrm{I}})$
KMed (PAM)	$O(Z^3K^2N_{\mathrm{I}})$
HC	$O(K^3N_{\mathrm{I}})$
CWC/ICWC	$O(IZKN_{\mathrm{B}}N_{\mathrm{I}}^2)$
OSCBC	$O(Z(K-Z)N_{\mathrm{I}})$

optimal configurations of the users with the worst channel conditions.

The remaining $k > Z$ users are associated as in (3.19). Then, at iteration i, the IRS configuration is updated as

$$\boldsymbol{\Phi}_{i+1}^{(z)} = f^{-1}\left(\frac{\sum_{k\in\mathcal{U}_z}\boldsymbol{\Phi}_k^* R_k^{-1}(\boldsymbol{\Phi}_k^*)}{\sum_{k\in\mathcal{U}_z} R_k^{-1}(\boldsymbol{\Phi}_k^*)}\right), \tag{3.25}$$

and the discretization step (3.24) is performed (if needed). As in CWC, convergence is achieved if the rate difference between two consecutive iterations is lower than the tolerance μ. While ICWC obtains lower sum rate than CWC, it can provide significant improvements in terms of fairness, especially from the perspective of the users with the worst channel conditions.

3.3.5 Computational Complexity Comparison

Computational complexity is evaluated as the number of iterations required by each of the clustering algorithms to:

1. obtain the optimal IRS configuration of each user;
2. partition the users into disjoint subsets, or clusters, based on distance or capacity metrics; and
3. for each cluster, find the best IRS configuration to serve the corresponding users.

In Table 3.1 we compare the computational complexity of the clustering algorithms presented in Sections 3.3.3 and 3.3.4. In all the algorithms, the first step is to obtain the optimal IRS configuration of each user, as described in Section 3.3.2. At each iteration, the main source of complexity is the computation of the overall cascade channel matrix $\boldsymbol{G}_k\boldsymbol{\Phi}_k\boldsymbol{H}$, which has complexity $O\big(N_{\mathrm{B}}N_{\mathrm{I}}^2 + N_{\mathrm{B}}N_{\mathrm{I}}N_{\mathrm{U}}\big)$. Additionally, in the case of quantized IRS phase shifts, after obtaining the optimal beamformers, the optimal phase shifts

for the IRS are obtained through an exhaustive search over the set of possible phase shifts $\mathcal{P}_\theta$, yielding a complexity of $O(2^b N_\mathrm{I})$.

Notice that different clustering algorithms, in general, require a different number of iterations I to reach convergence, thus possibly introducing practical limitations. Moreover, the complexity exhibited by each iteration varies across different clustering algorithms. Therefore, in the following, we characterize the overall complexity of each considered clustering strategy.

Distance-based clustering. These algorithms do not require specific initialization. For KM, based on the Lloyd implementation in [108], each iteration involves calculating the distances between data points and centroids. As a result, the computational complexity is influenced by the number of iterations required for convergence, the number of data points, the number of clusters, and the dimensionality of data, resulting in an overall complexity of $O(IZKN_\mathrm{I})$. KMed can be solved with the PAM algorithm [111], which exhibits computational complexity $O(Z^3K^2N_\mathrm{I})$, due to the pairwise distance computations between data points and medoids. Finally, the computational complexity of the agglomerate HC is primarily determined by the computation of pairwise distances among all data points, resulting in a total complexity of $O(K^3N_\mathrm{I})$ [113].

Capacity-based clustering. The complexity of the OSCBC algorithm is dominated by the centroid assignment upon initialization, which, has complexity $O\big(Z(K-Z)\big)N_\mathrm{I}$. Instead, for the iterative capacity-based clustering algorithms, the following result holds.

Theorem 6. *The time complexity of CWC and ICWC scales quadratically with N_I as $O(IZKN_\mathrm{B}N_\mathrm{I}^2)$.*

Proof. Capacity-based clustering requires an initialization stage where the algorithm selects the Z users providing the highest (or lowest) $R_k\big(\mathbf{\Phi}_k^*\big)$, resulting in a complexity of $O(K\log K)$ due to the sorting of K scalars. In the subsequent iterations:

1. Both CWC and ICWC compute the rate difference between each user and the Z centroids. The complexity of computing $R_k(\mathbf{\Phi}_i^{(z)})$ can be either dominated by the matrix multiplication in (3.4), or by the SVD needed for the single stream beamforming which requires, respectively, $O\big(N_\mathrm{B}N_\mathrm{I}^2 + N_\mathrm{B}N_\mathrm{I}N_\mathrm{U}\big)$ and $O\big(N_\mathrm{B}N_\mathrm{U}\min(N_\mathrm{B},N_\mathrm{U})\big)$ operations for each user and each centroid.

2. The computation of the centroids as per (3.23)-(3.25) requires $N_\mathrm{I}+1$ scalar operations per user, thus exhibiting negligible complexity with respect to the rate computation.

In typical IRS-aided systems $N_{\mathrm{I}} \gg N_{\mathrm{B}} > N_{\mathrm{U}}$, therefore, the complexity at each iteration is dominated by the channel matrix product, and the overall algorithm complexity is $O(IZKN_{\mathrm{B}}N_{\mathrm{I}}^2)$. □

3.4 Downlink OFDMA Scheduling

In this section, the extension to the downlink OFDMA scheduling with reconfiguration constraints is investigated. In this framework $F \geq 1$, therefore all the constraints exposed in Section 3.2 must be considered in the scheduling optimization. Moreover, we consider different that the IRS configuration codebooks, inluding the case $\mathcal{C}_{\mathbf{\Phi}} = \mathcal{P}_{\theta}^{N_{\mathrm{I}}}$, which eventually includes the case of b-bits quantized phase shifts. We formalize the sum rate maximization problem as an NP-complete generalized multi-knapsack problem, and we propose a heuristic greedy algorithm for the joint IRS configuration and time-frequency scheduling. Numerical simulations prove the effectiveness of our greedy solution.

3.4.1 OFDMA Sum Rate Optimization Problem

As for the TDMA case, we impose the following constraints.

1. at most Z IRS reconfigurations, choosen from codebook $\mathcal{C}_{\mathbf{\Phi}}$, can occur per time frame. Each configuration is kept for $\alpha_z \in \mathbb{N}$ time slots, where α_z has to be optimized as well; [3]

2. the BS serves K users by partitioning them into Z disjoint subsets $\mathcal{U}_1, \ldots, \mathcal{U}_Z$, $Z \leq K/F$, and assigning each user to a unique RB;

3. for each user in $\mathcal{U}_z$, the same IRS configuration $\mathbf{\Phi}^{(z)}$ is used, i.e., $\mathbf{\Phi}_k = \mathbf{\Phi}^{(z)}, \forall\, k \in \mathcal{U}_z, \forall\, 1 \leq z \leq Z$.

Let $\mathcal{S}_i$, $i = 1, \ldots, F$, be the set of users assigned to frequency i. Also, define the assignment variables

$$x_{k,z,i} = \begin{cases} 1 & \text{if } k \in \mathcal{U}_z \cap \mathcal{S}_i, \\ 0 & \text{otherwise.} \end{cases} \tag{3.26}$$

With this notation, the system sum rate 3.6 can be rewritten as

$$R(\mathcal{U}_1, \ldots, \mathcal{U}_Z, \mathcal{Y}, \mathcal{I}) = \sum_{z=1}^{Z} \sum_{k=1}^{K} \sum_{i=1}^{F} R_k(\mathbf{\Phi}^{(z)}, f_i) x_{k,z,i} \tag{3.27}$$

[3] Note that, if the codebook is small, two or more users' subsets could share the optimal configuration, in such case, the clusters are merged, and the number of reconfigurations is reduced.

leading to the following formulation of the joint resource allocation and configuration optimization problem.

$$\max_{\substack{\boldsymbol{\Phi}^{(z)},\alpha_z \\ x_{k,z,i}}} \sum_{z=1}^{Z}\sum_{k=1}^{K}\sum_{i=1}^{F} R_k(\boldsymbol{\Phi}^{(z)}, f_i)x_{k,z,i} \tag{3.28a}$$

$$\text{s.t.} \quad \boldsymbol{\Phi}^{(z)} \in \mathcal{C}_{\boldsymbol{\Phi}}, \tag{3.28b}$$

$$x_{k,z,i} \in \{0,1\}, \quad \forall k,z,i, \tag{3.28c}$$

$$\sum_{z=1}^{Z}\sum_{i=1}^{F} x_{k,z,i} = 1 \quad \forall k, \tag{3.28d}$$

$$\sum_{k=1}^{K} x_{k,z,i} = \alpha_z \quad \forall i,z, \tag{3.28e}$$

where constraint (3.28b) imposes the IRS configurations to be chosen the codebook $\mathcal{C}_{\boldsymbol{\Phi}}$, and (3.28c)-(3.28d) impose the assignment of each user to a unique RB. Instead, constraint (3.28e) imposes the clusters' cardinalities to be an integer multiple of F, reflecting the frequency non-selectivity of the IRS configuration. Note that, due to constraints (3.28d)-(3.28e) $\sum_{z=1}^{Z}\alpha_z = K/F$, α_z represents indeed the number of time slots for which $\boldsymbol{\Phi}^{(z)}$ is kept.

Note that (3.28) belongs to the class of generalized multi-knapsack problems, which are well-known to be NP-complete. This straightforward intuition also comes from the NP-completeness of the simpler problem for sum rate optimization in TDMA (3.8). Its solution requires an exhaustive search over all the discrete parameters, therefore, a heuristic approach, which splits (3.28) into two sub-problems, is necessary to reduce the complexity. Moreover, we remark that the size of codebook $\mathcal{C}_{\boldsymbol{\Phi}}$ may be extremely large, up to the case $|\mathcal{C}_{\boldsymbol{\Phi}}| = 2^{b_{\mathrm{I}}N_{\mathrm{I}}}$, i.e., all the combinations of phase shifts, thus exacerbating the problem complexity.

3.4.2 Optimization Problem Decomposition

With the aim of simplifying problem (3.28), we first propose to decompose the joint resource allocation and configuration assignment into two sub-problems named, respectively, the *configurations assignment*, and the *RB assignment*.

The configuration assignment sub-problem assigns one user per cluster, leaving $K - Z$ users unassigned, and sets the IRS configuration for each cluster. The problem can be

written as

$$\max_{\substack{\boldsymbol{\Phi}^{(z)} \\ x_{k,z,i}}} \sum_{z=1}^{Z} \sum_{i=1}^{F} R_k(\boldsymbol{\Phi}^{(z)}, f_i) x_{k,z,i} \tag{3.29a}$$

$$\text{s.t.} \quad (3.28\text{b}), (3.28\text{c}), \sum_{k=1}^{K} \sum_{i=1}^{F} x_{k,z,i} = 1 \quad \forall z. \tag{3.29b}$$

In the RB assignment sub-problem, instead, the remaining users are assigned to the clusters defined with (3.29) as

$$\max_{\substack{\alpha_z \\ x_{k,z,i}}} \sum_{z=1}^{Z} \sum_{k=1}^{K} \sum_{i=1}^{F} R_k(\boldsymbol{\Phi}^{(z)}, f_i) x_{k,z,i}, \text{ s.t. } (3.28\text{c}), (3.28\text{d}), (3.28\text{e}). \tag{3.30}$$

Note that both the RB assignments and the cluster cardinality constraint (3.28e), are assessed in this second step, as α_z, $z = 1, \ldots, Z$ are optimization variables. Moreover, (3.30) is still a multi-knapsack assignment problem with variable knapsack capacities, therefore belonging to the class of NP-complete problems.

3.4.3 Greedy Maximum-Rate Scheduler

Algorithm 3.3 Greedy Maximum-Rate Scheduler

Require: $R_k(\boldsymbol{\Phi}, f_i)$ for all $k, i, \boldsymbol{\Phi} \in \mathcal{C}_{\boldsymbol{\Phi}}$
Ensure: $\mathcal{I}, x_{k,z,i}$, for all k, z, i
$\alpha_z \leftarrow 1$, for all z
$x_{k,z,i} \leftarrow 0$, for all k, z, i
$(x_{k,z,i}, \boldsymbol{\Phi}^{(z)}) \leftarrow$ solve (3.29) exhaustively
while $\sum_{z=1}^{Z} \sum_{k=1}^{K} \sum_{i=1}^{F} x_{k,z,i} < K$
  while $\sum_{z=1}^{Z} \sum_{k=1}^{K} \sum_{i=1}^{F} x_{k,z,i} \leq F \sum_{z=1}^{Z} \alpha_z$
    $x_{k,z,i} \leftarrow 1$ for k, i solving (3.31)
  end while
  if $\sum_{z=1}^{Z} \sum_{k=1}^{K} \sum_{i=1}^{F} x_{k,z,i} < K$
    $(k, z, i) \leftarrow$ solve (3.31) neglecting constraint (3.28e)
    $\alpha_z \leftarrow \alpha_z + 1$
    $x_{k,z,i} \leftarrow 1$
  end if
end while

Due to the complexity of (3.28), we resort to a greedy approach to obtain a heuristic but close-to-optimal solution, by proposing the greedy maximum-rate scheduler (GMAX)

algorithm, summarized in Algorithm 3.3.

First, we observe that (3.29) can be solved by exhaustively computing $R_k(\mathbf{\Phi}, f_i)$ for all $i = 1, \dots, F$, $\mathbf{\Phi} \in \mathcal{C}_{\mathbf{\Phi}}$, and $k = 1, \dots, K$, and then selecting the Z users (with their IRS configuration) providing the highest rate. Each of the selected users is assigned to RB maximizing (3.27), respectively. Once (3.29) is solved, Z clusters are created, each consisting of one user only. Moreover, each cluster z is associated with a configuration $\mathbf{\Phi}^{(z)}$, and the configurations for $z = 1, \dots, Z$ are collected in set $\mathcal{I}$.

To handle the remaining users and solve (3.30), instead, we resort to a greedy sub-optimal approach. At each iteration, GMAX solves

$$(k, z, i) = \underset{k,z,i}{\operatorname{argmax}} R_k(\mathbf{\Phi}^{(z)}, f_i) \tag{3.31a}$$

$$\text{s.t.} \quad (3.28e),\ \mathbf{\Phi} \in \mathcal{I}, \tag{3.31b}$$

$$k \in \{k : x_{k,z,i} = 0 \ \forall\, z, i\}, \tag{3.31c}$$

$$(z, i) \in \{(z, i) : x_{k,z,i} = 0 \ \forall\, k\}. \tag{3.31d}$$

Since $Z \leq \frac{K}{F}$ in general, the users are firstly allocated considering only F RBs per cluster, i.e., one time slot per IRS configuration, by setting $\alpha_z = 1$ for all z. Once the first ZF users are allocated, the algorithm proceeds by solving problem (3.31), considering the allocation of new time slots in the resource grid (i.e. increasing α_z by one).

At the end of the procedure, each user is assigned to a specific RB, satisfying all the constraints of problem (3.28). Note that, as per (3.26), sets $\mathcal{U}_1, \dots, \mathcal{U}_Z$, and $\mathcal{S}_i$ are uniquely determined by variables $x_{k,z,i}$, for $z = 1 \dots, Z$, $i = 1, \dots, F$, $k = 1, \dots, K$. We remark that codebook $\mathcal{C}_{\mathbf{\Phi}}$ may contain all the possible IRS configurations, i.e., all the $2^{bN_{\mathrm{I}}}$ combinations of phase shifts. Therefore, the introduction of the codebook constraint does not limit the contribution, but it extends it to the more general case of limited choices of the configurations.

Codebook Design And Control Overhead

To obtain the cell-specific codebook of IRS configurations $\mathcal{C}_{\mathbf{\Phi}}$, a clustering-based approach is employed. In particular, similarly to the distance-based clustering proposed in Section 3.3.3, the points to be clustered are the IRS phase shifters (with b-bits quantization) that maximize the achievable rate (3.5), at each $f \in \mathcal{F}$, of $\bar{K}$ users deployed at random positions in the cell, with $\bar{K} \gg K$. Such configurations are grouped into $|\mathcal{C}_{\mathbf{\Phi}}| \ll \bar{K}$ clusters, according to the well-known KM clustering [108], and the codebook entries are

the resulting cluster centroids.

Note that the codebook allows a substantial reduction of the IRS control link overhead. Indeed, for each IRS reconfiguration, the BS transmits $b_{\mathrm{q}} = \log_2 |\mathcal{C}_{\boldsymbol{\Phi}}|$ bits, instead of the bN_{I} bits needed to configure each phase shifter individually. Moreover, by further limiting the number of reconfigurations per time frame to Z, the total number of control bits is reduced by a factor $\frac{ZF}{K} \leq 1$.

Computational Complexity

The computational complexity of GMAX is mainly due to the maximum rate computation for the initial choice of the Z IRS configurations in (3.29). Specifically, the cascade channel matrix product $\boldsymbol{G}_k \boldsymbol{\Phi}_k \boldsymbol{H}$ dominates computations with a complexity $O\big(N_{\mathrm{B}} N_{\mathrm{I}}^2 + N_{\mathrm{B}} N_{\mathrm{I}} N_{\mathrm{U}}\big)$, and the procedure must be done for all users, central frequencies, and IRS configurations in the codebook. Similarly, the second loop computes the R_k in the same fashion, but the search is restricted to set $\mathcal{I}$, and typically $|\mathcal{I}| = Z \ll 2^{b_{\mathrm{q}}}$. As a result, the overall complexity of GMAX is $O\big(ZF(2^{b_{\mathrm{q}}} + 1)(N_{\mathrm{B}} N_{\mathrm{I}}^2 + N_{\mathrm{B}} N_{\mathrm{I}} N_{\mathrm{U}})\big)$. Note that, in the first step the complexity grows exponentially with the codebook overhead, penalizing codebooks of large resolution. This suggests the adoption of a cell-specific codebook to maximize the rate with low overhead. However, a further complexity reduction can be achieved by observing that, in the first loop, only the optimal IRS configuration of each user, i.e., the one maximizing its transmission rate, is needed. A possible approach is to derive the optimal IRS configuration $\boldsymbol{\Phi}_k'^{*}(f_i)$ for all k, i in the continuous phase domain, as described in Section 3.3.2. $\boldsymbol{\Phi}_k'^{*}(f_i)$ is then mapped to the closest (in the sense of circular distance) codeword in the codebook $\boldsymbol{\Phi}_k^* \in \mathcal{C}_{\boldsymbol{\Phi}}$. While the time complexity of deriving $\boldsymbol{\Phi}_k'^{*}(f_i)$ for each k, i is $O\big(N_{\mathrm{B}} N_{\mathrm{I}}^2 + N_{\mathrm{B}} N_{\mathrm{I}} N_{\mathrm{U}}\big)$, its approximation requires $O(2^{b_{\mathrm{q}}} N_{\mathrm{I}})$ operations. With this approximation, the total complexity can be reduced to $O\big(K(2^{b_q} + (N_{\mathrm{B}} N_{\mathrm{I}}^2 + N_{\mathrm{B}} N_{\mathrm{I}} N_{\mathrm{U}} N_{\mathrm{I}})) + ZF(N_{\mathrm{B}} N_{\mathrm{I}}^2 + N_{\mathrm{B}} N_{\mathrm{I}} N_{\mathrm{U}})\big)$.

3.5 Numerical Results

After presenting our various simulation scenarios and evaluation metrics, in this section, we assess the scheduling performance of an IRS-assisted network with practical constraints.

Simulation Parameters

Our simulation parameters are reported in Table 3.2.

Table 3.2: Simulation parameters.

Parameter	Value
Carrier frequency	28 GHz
Total bandwidth (W)	100 MHz
Noise spectral density	-174 dBm/Hz
Number of users (K)	100
BS antenna array (N_{B})	8H×8V
BS transmit power	33 dBm
UE antenna array (N_{U})	2H×1V
IRS elements (N_{I})	{10H×20V, 20H×40V, 40H×80V, 60H×120V}
Phase shift quant. bits (b)	{unquantized, 1-bit, 2-bits}
LoS probability (p_{LoS})	Eq. (3.33)
Individual rate opt. tolerance (ν)	10^{-6} [bit/s/Hz]
KM max. iterations ($I_{\max}^{\mathrm{KM}}$)	50
CWC/ICWC rate tolerance (μ)	10^{-3} [bit/s]

Scenario. All devices are assumed to lie on a 2D plane, and we consider an urban macrocell (UMi) scenario, according to the 3GPP nomenclature [114], with the BS placed at the center. According to the 3GPP specifications, the coverage area of the BS is characterized by an average radius of 167 m and is assumed to lie in the positive x-axis region.

We assume that $K = 100$ users are randomly deployed according to a uniform distribution within the cell area, to be served in downlink by the BS, assisted by an IRS at coordinates $(75, 100)$ m. The BS is equipped with a uniform planar array (UPA) with 8H×8V antennas (i.e., $N_{\mathrm{B}} = 64$), and the users with uniform linear arrays (ULAs) of 2H×1V antennas (i.e., $N_{\mathrm{U}} = 2$). For the IRS, if not otherwise specified, we adopt a 40H×80V reflective panel ($N_{\mathrm{I}} = 3200$).

Channel and Frame Structure. The system operates at a carrier frequency of 28 GHz (that is in the lower part of the mmWave bands), the transmission power at the BS is set to 33 dBm, the noise power spectral density at the receivers is -174 dBm/Hz and the total system bandwidth is 100 MHz. Finally, we consider the fourth numerology of the NR frame structure [61], wherein each 10 ms frame is split into 160 ms slots. With this assumption, as already pointed out in Section 3.2, channels can be considered constant over the entire frame duration. We consider the 3GPP TR 38.901 spatial channel model [114], which supports a wide range of frequencies, from 0.5 to 100 GHz (and including therefore our carrier frequency of 28 GHz), and can be integrated with realistic beamforming models. As such, channel matrices, and multipath fading, are computed based on the superposition of N different clusters, each of which consists of M rays that

arrive (depart) to (from) the antenna arrays with specific angles and powers. Based on [114], and using the simplifications proposed in [115], the generic entry $[\boldsymbol{A}]_{pq}$ of the channel matrix can then be computed as:

$$[\boldsymbol{A}]_{pq} = \gamma \sum_{n=1}^{N} \sqrt{\frac{P_n}{M}} \sum_{m=1}^{M} \overline{\mathbf{F}}_{rx}\left(\theta_{n,m}^{A}, \phi_{n,m}^{A}\right) \begin{bmatrix} e^{j\Phi_{n,m}^{\theta,\theta}} & \sqrt{K_{n,m}^{-1}} e^{j\Phi_{n,m}^{\theta,\phi}} \\ \sqrt{K_{n,m}^{-1}} e^{j\Phi_{n,m}^{\phi,\theta}} & e^{j\Phi_{n,m}^{\phi,\phi}} \end{bmatrix} \times \overline{\mathbf{F}}_{tx}\left(\theta_{n,m}^{D}, \phi_{n,m}^{D}\right) e^{j\overline{\mathbf{k}}_{rx,n,m}^{\mathrm{T}} \overline{\mathbf{d}}_{rx,p}} e^{j\overline{\mathbf{k}}_{tx,n,m}^{\mathrm{T}} \overline{\mathbf{d}}_{tx,q}}, \tag{3.32}$$

where γ is the large-scale fading coefficient (LSFC) of the considered link, which incorporates the path loss and shadowing terms. For a complete description of the remaining terms appearing in (3.32) we refer the interested reader to [115]. Specifically, while the BS and the IRS can be assumed to operate in line-of-sight (LoS), the path loss between a generic user k and the IRS is modeled based on the following channel conditions:

- *non-line-of-sight (NLoS)*: user k is in NLoS with the IRS;
- *deterministic line-of-sight (dLoS)*: user k is in LoS with the IRS;
- *probabilistic line-of-sight (pLoS)*: the IRS-UE k link is in LoS$\vee$NLoS with respective probabilities $p_k^{\mathrm{LoS}}(d_k) \vee 1-p_k^{\mathrm{LoS}}(d_k)$, with

$$p_k^{\mathrm{LoS}}(d_k) = \begin{cases} 1 & \text{if} \quad d_k \leq 18, \\ \frac{18}{d_k} + \left(1 - \frac{18}{d_k}\right) e^{-\frac{d_k}{36}} & \text{if} \quad d_k > 18, \end{cases} \tag{3.33}$$

  where d_k is the distance (in m) between the IRS and user k. In the considered UMi scenario, and based on 3GPP specifications [114], the average LoS probability in (3.33) is 0.35.

For each wireless link, based on the presence of the LoS component, the path loss is then derived according to [114, Table 7.4.1-1], with shadowing standard deviation set to $\sigma_{\mathrm{SF}} = 0$. For the optimal individual IRS configuration (Section 3.3.2), we set $\nu = 10^{-6}$ [bit/s/Hz].

3.5.1 TDMA Scheduling Results

In the following subsections, we present extensive simulation results to compare the performance of distance-based (KM, HC, KMed) vs. capacity-based (CWC, OSCBC, ICWC) clustering algorithms to perform TDMA scheduling in an IRS system with reconfiguration constraints. The KM clustering has been implemented with the Lloyd algorithm [108]

with a maximum number of $I_{\max}^{\mathrm{KM}} = 50$ iterations. Instead, for both CWC and ICWC, we set $\mu = 10^{-3}$ [bit/s].

As an upper bound to the system performance, we also consider an "unclustered" scheduling, wherein we assume that all users are served with their optimal IRS configuration. This scheduling clearly violates the constraint on the maximum numbers of reconfiguration per frame but can be regarded as the limit case when $Z = K$, i.e., all users belong to a cluster with cardinality one. As such, it is a suitable approach for benchmarking the performance of more practical schemes.

Performance Metrics

The performance of the proposed clustering-based scheduling techniques is evaluated in terms of average sum capacity and fairness, as a function of the numbers of both clusters and users, under different channel conditions, IRS dimensions, and degrees of quantization for the phase shifts.

Average sum capacity. It is derived from (3.7) as

$$\bar{C} = \frac{W}{K} \mathbb{E}\left[R(\mathcal{U}_1, \ldots, \mathcal{U}_Z, \mathcal{I})\right], \tag{3.34}$$

where W is the total system bandwidth and the expectation is computed across the different channel realizations. Moreover, as each user is served in its specific slot, we average over the TDMA frame length, dividing the empirical expectation by the number of users (slots) K.

Fairness. We consider the 95% percentile of the achieved individual user capacity, computed as

$$C_{95\%} = \frac{W}{K} \inf\{x : \mathrm{CDF}(x) \geq 0.95\}, \tag{3.35}$$

where $\mathrm{CDF}(\cdot)$ is the empirical cumulative distribution function of $R_k(\mathbf{\Phi}^{(z)})$, $\forall k, z$. Note that the choice of the 95% percentile in this context is a practical and meaningful way to evaluate fairness by focusing on the majority of users. Indeed, it aligns with ensuring high individual capacity for each user.

Scheduling Performance

In this section, we compare the IRS scheduling performance considering distance-based vs. capacity-based clustering, and as a function of different channel conditions, reconfiguration constraints, and degrees of quantization of the phase shifts.

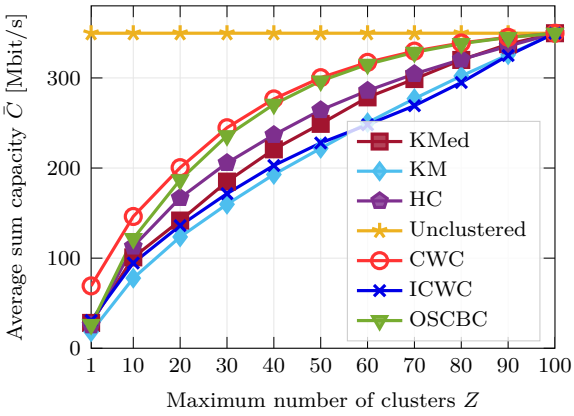

Figure 3.3: Average sum capacity as a function of the maximum number of clusters Z, for an unquantized 40H×80V IRS, and considering a pLoS channel for the IRS-UEs links.

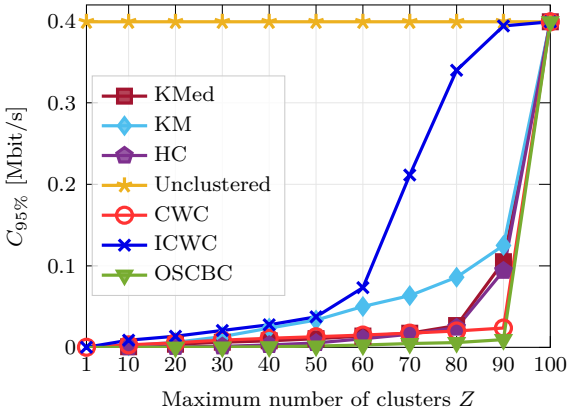

Figure 3.4: 95% percentile of the user capacity as a function of the maximum number of clusters Z, for an unquantized 40H×80V IRS, and considering a pLoS channel for the IRS-UEs links.

Impact of the clustering algorithm. First, Fig. 3.3 displays the average sum capacity $\bar{C}$ per slot as a function of the number of clusters Z, for unquantized IRS phase shifts, and considering a pLoS channel for the IRS-UEs links. It is evident that all the scheduling policies perform better as Z increases, and they all converge to the "unclustered" policy when $Z = K$. In fact, increasing the number of clusters corresponds to a smaller intra-cluster average distance, which eventually becomes zero when $Z = K$. Among the considered clustering policies, CWC and OSCBC provide the highest sum capacity, as they are designed to maximize $\bar{C}$, and choose the IRS configurations of the users that achieve the highest rate. Instead, distance-based clustering achieves worse performance as it does not exploit the knowledge of the rate achievable with different IRS configurations when building the clusters. As expected, ICWC is designed to promote fairness, thus underperforms both CWC and OSCBC in terms of sum capacity; still, it achieves similar performance as distance-based clustering. Finally, the gap between CWC and OSCBC is almost negligible: this implies that a single iteration in the clustering process is enough to achieve good sum capacity, while also promoting lower computational complexity as reported in Table 3.1, which demonstrates the good scalability of the proposed techniques.

Fig. 3.4 compares the fairness performance of the different clustering algorithms, measured as the 95% percentile of the average sum capacity $C_{95\%}$, as a function of the maximum number of clusters Z in pLoS conditions. Our results identify ICWC as the best clustering approach in terms of fairness, which comes at the cost of a lower sum capacity, as shown in Fig. 3.3. Therefore, there exists a trade-off between the achievable sum

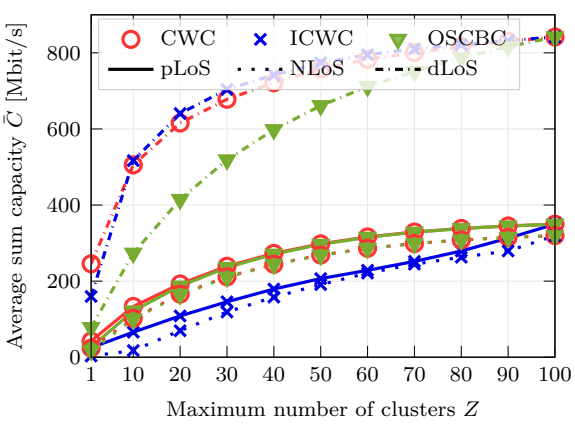

Figure 3.5: Average sum capacity as a function of the maximum number of clusters Z, for $N_{\mathrm{I}} = 3200$, unquantized phase shifts, and for different channel conditions.

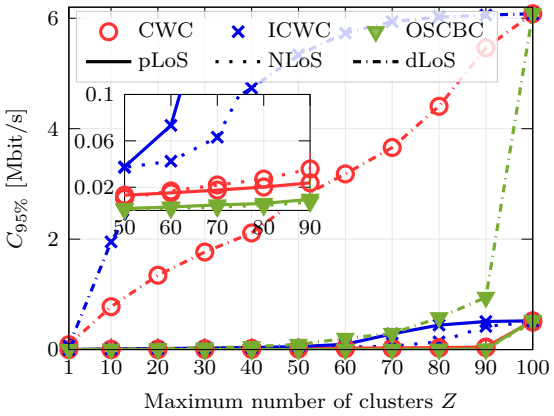

Figure 3.6: 95% percentile of the user capacity as a function of the maximum number of clusters Z, for $N_{\mathrm{I}} = 3200$, unquantized phase shifts, and for different channel conditions. The zoom inside the figure is for $50 \leq Z \leq 90$.

capacity and fairness. We also observe that OSCBC achieves very low fairness, as the users with worst channel conditions are forced to aggregate to the strongest users, thus via a sub-optimal IRS configuration. On the other hand, we see that CWC is more than acceptable in terms of fairness, and achieves comparable performance than most of the distance-based clustering algorithms. Finally, notice that $C_{95\%}$ increases as Z increases, and eventually approaches the unclustered baseline for $Z = K$. This is due to the fact that the LoS probability in the pLoS scenario increases with the number of clusters, i.e., as the inter-cluster distance becomes smaller, which permits to experience better channel conditions, thus a higher capacity, even for the worst users.

Impact of the channel. From the above results, we concluded that distance-based clustering provides lower sum capacity and fairness compared to capacity-based scheduling, so the rest of our simulation campaign has been focused on the latter. Figs. 3.5 and 3.6 display the average sum capacity and the 95% percentile, respectively, for CWC, ICWC, and OSCBC in different channel conditions. First, we observe that in the dLoS scenario, where users are in LoS with the IRS, the sum capacity is up to 2.6 (2.4) times higher than in the NLoS (pLoS) scenario for $Z = K$. This is mainly due to the fact that NLoS links experience a) a higher path loss, and b) the lack of a dominant multipath component, thus of a clear steering direction for the IRS beam, which deteriorates the link quality. In particular, in the pLoS scenario, the LoS probability decreases exponentially with the distance, therefore, the users that are far from the IRS typically operate in NLoS. For similar reasons, both CWC and ICWC in the dLoS scenario start to reach stability in

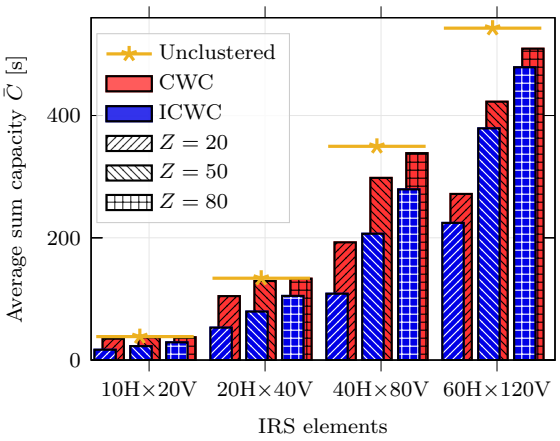

Figure 3.7: Average sum capacity for CWC and ICWC as a function of the number of reflecting elements at the IRS, for unquantized phase shifts, and considering a pLoS channel for the IRS-UEs links.

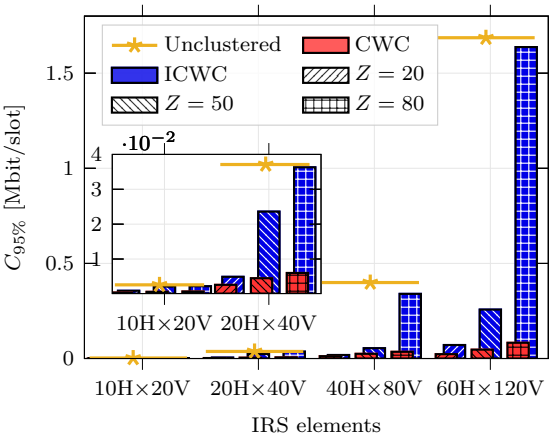

Figure 3.8: 95% percentile of the user capacity for CWC and ICWC as a function of the number of reflecting elements at the IRS, for unquantized phase shifts, and considering a pLoS channel for the IRS-UEs links. The zoom inside the figure is for $N_{\mathrm{I}} = 200$ and $N_{\mathrm{I}} = 800$.

terms of capacity with a relatively lower number of clusters than in the pLoS and NLoS scenarios.

As expected, OSCBC performs worse than its competitors, and the gap is even more significant in the dLoS scenario (around -30% in terms of sum capacity). The bad performance of OSCBC compared to CWC and ICWC is confirmed also in terms of fairness, as illustrated in Fig. 3.6 (see, in particular, the zoom for $50 \leq Z \leq 90$).

Finally, although ICWC is not explicitly designed to maximize the sum capacity, it shows similar performance (if not even slightly better) as CWC in the dLoS scenario. The rationale behind this behavior is not clear and deserves more investigation. Most likely, it is related to the fact that, in the dLoS scenario, all users have similar channel conditions, which permits ICWC to choose, on average, a good IRS configuration even among the worst users in the clusters.

Impact of the IRS configuration. Figs. 3.7 and 3.8 show the impact of the number of IRS radiating elements on the system performance when considering the CWC and ICWC clustering algorithms. As expected, both fairness (measured in terms of the 95% percentile of the average sum capacity) and sum capacity increase as the IRS is larger and operates with more reflecting elements, regardless of the number of clusters. For example, we observe that CWC is able to approach the optimal sum capacity with as few as 20 clusters for small-sized IRS, i.e., with 10H×20V or 20H×40V arrays. The same trends are shown also in Fig. 3.8 also in terms of fairness. Still, notice that $\bar{C}$ is below 100 Mbps,

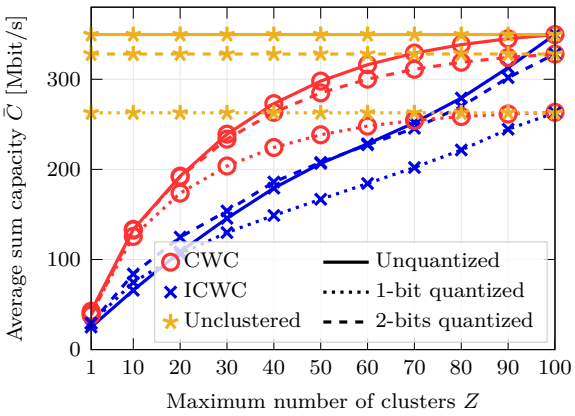

Figure 3.9: Average sum capacity as a function of the maximum number of clusters Z, for $N_{\mathrm{I}} = 3200$ and for different degrees of quantization of the phase shifts, and considering a pLoS channel for the IRS-UEs links.

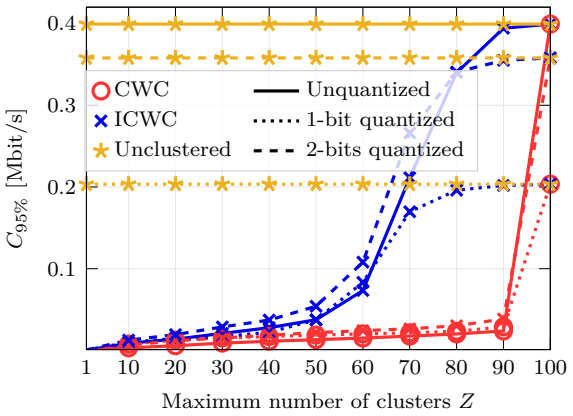

Figure 3.10: 95% percentile of the user capacity as a function of the maximum number of clusters Z, for $N_{\mathrm{I}} = 3200$ and for different degrees of quantization of the phase shifts, and considering a pLoS channel for the IRS-UEs links.

which is not compatible with the requirement of most 5G applications when the IRS is made of fewer than 200 elements, which justifies the use of larger IRS panels [**116**].

Nevertheless, we still observe that the number of reflecting elements has an impact on the number of clusters that are needed to provide maximum performance. Indeed, the number of possible IRS configurations increases as we consider larger IRS antennas. In turn, this decreases the likelihood of users having the same (or similar) ideal configurations, and therefore, it increases the probability of being associated with increasingly sub-optimal centroids if the number of clusters is small. However, if the number of phase shifters is large, the sub-optimality is mitigated by the increasing number of reconfigurations.

Impact of quantization. Figs. 3.9 and 3.10 display the average sum capacity and the 95% percentile, respectively, as a function of the maximum number of clusters Z for CWC and ICWC, and of the number of quantization bits b of the phase shifts. Notice that energy and hardware constraints pose a limit to b [117], which implies restricting the infinite set of possible IRS configurations to a finite set of cardinality $2^{bN_{\mathrm{I}}}$. Moreover, the quantization constraint affects the beamforming capabilities of the IRS [86], with negative implications for the resulting achievable sum capacity. Here, we assume that the quantization of the phase shifts is taken into account from the initial optimization stage. The results reveal that the use of non-ideal phase shifters leads to a 30% degradation in the sum capacity when using $b = 1$ at the IRS, while the performance is close to the unquantized baseline if more quantization bits are used. Furthermore, it is shown that

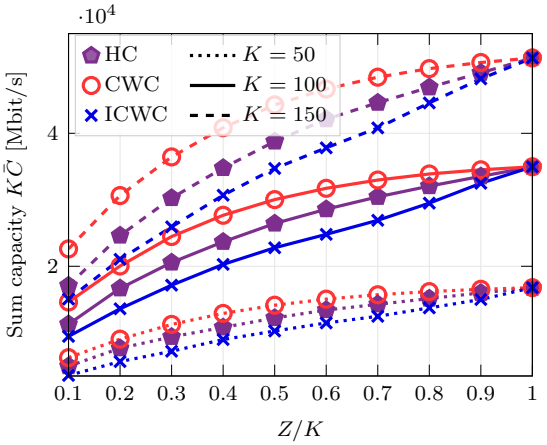

Figure 3.11: Sum capacity as a function of the maximum number of clusters over the number of users Z/K, for an unquantized 40H×80V IRS, $K = \{50, 100, 150\}$, and pLoS channels for the IRS-UEs links. For readability, the results are shown without averaging over the TDMA frame length.

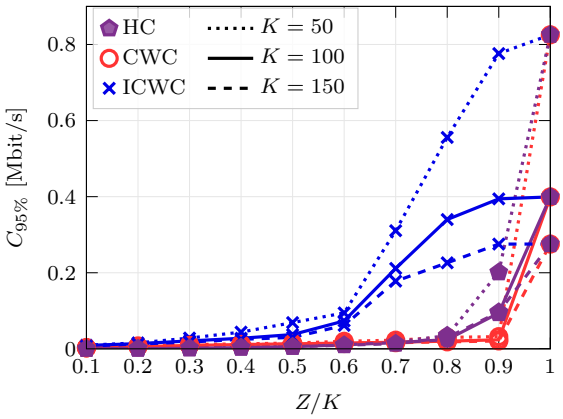

Figure 3.12: 95% of the user capacity as a function of the maximum number of clusters over the number of UEs Z/K, for an unquantized 40H×80V IRS, $K = \{50, 100, 150\}$ users, and pLoS channels for the IRS-UEs links.

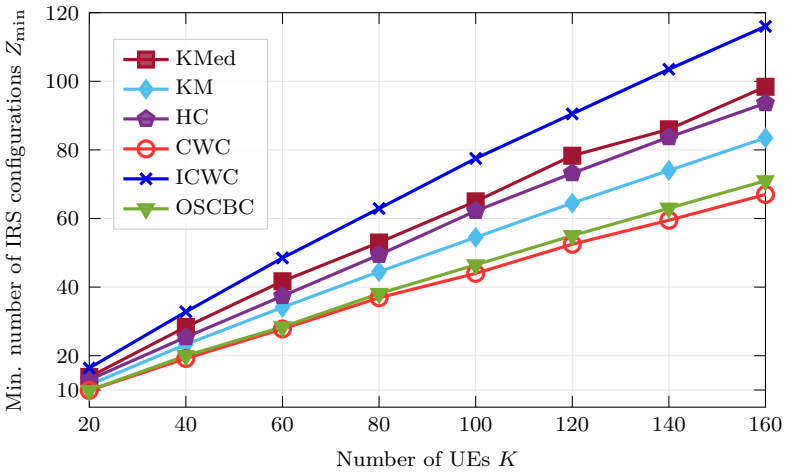

Figure 3.13: Minimum number of IRS configurations (clusters) $Z_{\min}$ to achieve 80% of the maximum achievable sum capacity, for an unquantized 40H×80V IRS, and considering a pLoS channel for the IRS-UEs links.

the gap between quantized the unquantized performance increases with Z. As a result, 1-bit quantization is sufficient to guarantee performance comparable to the unquantized case with a low number of clusters, while more quantization bits are needed to achieve higher capacity. In any case, we can conclude that our proposed capacity-based clustering algorithms are robust to phase-shift quantization.

Scalability. Finally, we prove the scalability performance of the proposed clustering algorithms. To do so, we first show the performance benefits provided by capacity-based clustering in Figs 3.11 and 3.12. In particular, we compare the performance of CWC and ICWC with HC as a function of the ratio K/N, for an unquantized 40H×80V IRS, $K = \{50, 100, 150\}$ users, and considering pLoS channels for the IRS-UEs links. Note that the achieved results match the plots in Figs 3.3 and 3.4, thus highlighting the scalability of the proposed clustering techniques for different numbers of users. Finally, Fig. 3.13 depicts the average minimum number of IRS configurations $Z_{\min}$ needed to achieve 80% of the maximum achievable sum capacity ("unclustered" baseline) as a function of the number of users K in the system. Notably, we observe that CWC and OSCBC are confirmed to be the best algorithms to optimize the sum capacity, even for a limited number of IRS configurations. For example, both solutions achieve 80% of the maximum sum capacity with less than half the number of configurations than in the "unclustered" deployment. Moreover, we recognize the same trends as in the previous results. Specifically, capacity-based clustering outperforms distance-based clustering and requires fewer IRS reconfigurations to maximize the sum capacity (up to −37% considering CWC vs. KMed). Furthermore, the gap increases as the number of users increases.

3.5.2 OFDMA Scheduling Results

For the performance evaluation of OFDMA scheduling, we consider a slightly different setup with ULA panels $N_{\mathrm{B}} = 32$ and $N_{\mathrm{U}} = 4$ antennas, while for the IRS, if not otherwise specified, we adopt a 20H×40V reflective panel ($N_{\mathrm{I}} = 800$), $b = 1$ phase shift quantization bits, and $b_{\mathrm{q}} = 14$ bits for the codebook overhead. Furthermore, we assume that RBs are equally spaced in the spectrum range $(f_{\mathrm{c}} - 10$ MHz, $f_{\mathrm{c}} + 10$ MHz). Neglecting the bandwidth, the system performance is evaluated in terms of *average sum rate*, defined as

$$\bar{R} = \mathbb{E}\left[R(\mathcal{U}_1, \ldots, \mathcal{U}_Z, \mathcal{Y}, \mathcal{I})\right], \tag{3.36}$$

where we average over multiple channel realization and randomly generated user positions.

Table 3.3: Average Sum Rate for Different IRS Sizes [bit/s/Hz]

	$b_{\mathrm{q}} = 12$	$b_{\mathrm{q}} = 14$	$b_{\mathrm{q}} = 16$	$b_{\mathrm{q}} = N_{\mathrm{I}}$
10H×20V	12.89	19.06	20.92	21.36
20H×40V	44.65	69.97	78.33	92.16
30H×60V	86.90	108.33	131.65	162.19

Compared Solutions

In the following, we compare GMAX with different resource allocation policies, under different codebook sizes.

Deterministic assignment (DA). As a baseline, in this scheduling, each user is deterministically assigned to an RB in cluster z and, upon the assignment, the IRS configuration $\mathbf{\Phi}^{(z)} \in \mathcal{C}_{\mathbf{\Phi}}$ maximizes the cluster sum rate.

Unconstrained OSCBC (UOSCBC). This is an extension to OFDMA scheduling of the OSCBC proposed in Section 3.3.4 for TDMA. The unique assignment to a particular RB, i.e., constraint (3.28d) is violated, as there is no limitation imposed in the number of users associated with each RB.

Genetic algorithm (GA). Finally, to analyze the gap between our proposed and the optimal solution of problem (3.28), GMAX is compared to a GA approach [118] with fitness function (3.28a), which initial population includes the GMAX solution. In such GA approach the population generation, crossover, and mutation functions are customized such that all the constraints (3.28b)-(3.28e) are always satisfied.

Performance Results

Firstly, Table 3.3 investigates the relationship between codebook size and system sum rate in the ideal case with $F = 1$ and each user scheduled with its optimal IRS configuration $\mathbf{\Phi}_k^*$. The results reveal the need for a large codebook to approximate the continuous case (i.e., $b_{\mathrm{q}} = N_{\mathrm{I}}$ for $b = 1$). Also, larger IRS panels are more sensitive to the codebook size, as a result of the larger number of degrees of freedom provided by the independent control of each phase shifter. For example, a 10H×20V-elements IRS achieves around 60% of the sum rate achievable with the continuous codebook with only $b_{\mathrm{q}} = 12$, and 98% for $b_{\mathrm{q}} = 16$. Instead, a 30H×60V-elements IRS requires $b_{\mathrm{q}} = 16$ to reach 81% of the sum rate achievable in the continuous case.

Fig. 3.14 depicts the average sum rate as a function of the number of clusters Z, comparing the different clustering strategies. Since each user must be scheduled once

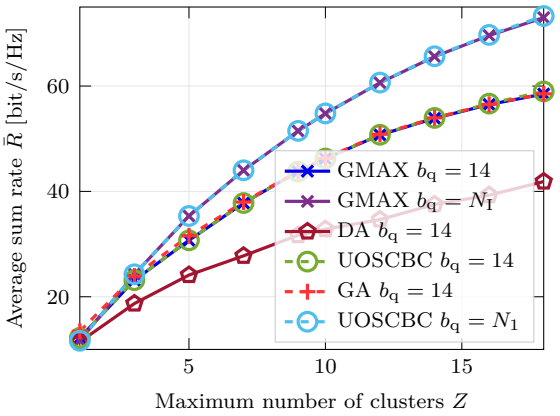

Figure 3.14: Average sum rate versus the number of clusters, for $K = 90$, $F = 5$.

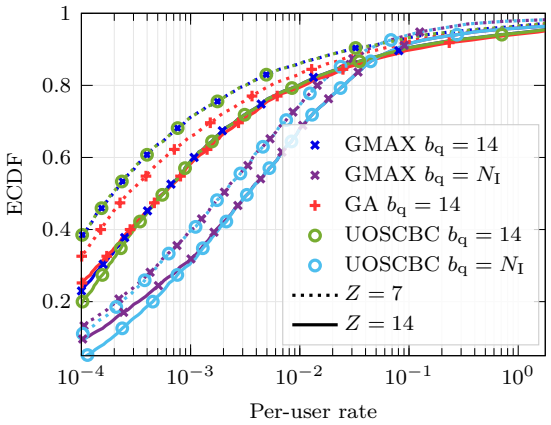

Figure 3.15: ECDF of the per-user rate, for $K = 90$, $F = 5$, and $Z \in \{7, 14\}$.

in the resource grid, Z is bounded by K/F. The results show a huge performance gap between the proposal and the DA baseline and highlight the huge performance degradation due to the codebook resolution compared to the slight impact of the frequency assignment constraints (3.28d)-(3.28e). In particular, GMAX and UOSCBC with high-resolution codebook ($b_q = N_I$) show a substantial sum rate gap with their respective low-resolution codebook case ($b_q = 14$), while the negligence of constraint (3.28d)-(3.28e) with UOSCBC does not provide any substantial benefit on the performance. Note that the proposed GMAX schedulers attain performance that is very close to the GA, which is shown to deviate very slightly from the greedy solution. Even if the GA approach cannot be considered optimal, such a negligible gap is representative of the validity of GMAX in this context. To emphasize the performance gap between the compared schemes, Fig. 3.15 shows the empirical cumulative distribution function (ECDF) of the per-user rate for fixed numbers of clusters $Z \in \{7, 14\}$. Note that, while the performance hierarchy remains invariant for almost all compared schemes, the adoption of the sum rate as the fitness function of GA may result in a different rate distribution than GMAX, promoting the users experiencing the best channel conditions and penalizing the remaining users.

Fig. 3.16 shows the average sum rate as a function of K, for $F = 3$ frequencies. Clearly, the sum rate increases with the number of users, however, it is important to notice that, for few clusters ($Z = 4$) the performance gap between GMAX with the low-resolution codebook and GMAX with $b_q = N_I$ becomes negligible for a large number of users, as the configurations associated to each cluster are sub-optimal in maximizing the sum rate in both cases.

Finally, to analyze the impact of the number of frequencies, Fig. 3.17 shows the sum

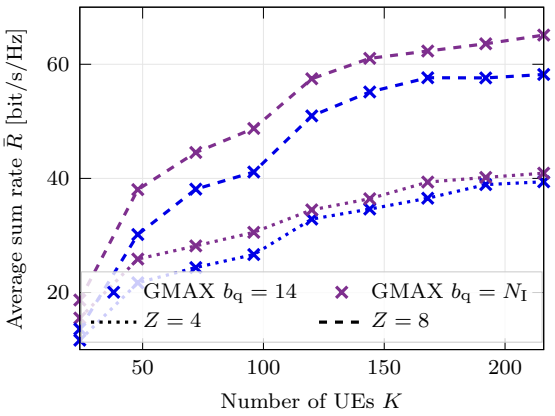

Figure 3.16: Average sum rate versus the number of users, for $F = 3$, and $Z \in \{4, 8\}$.

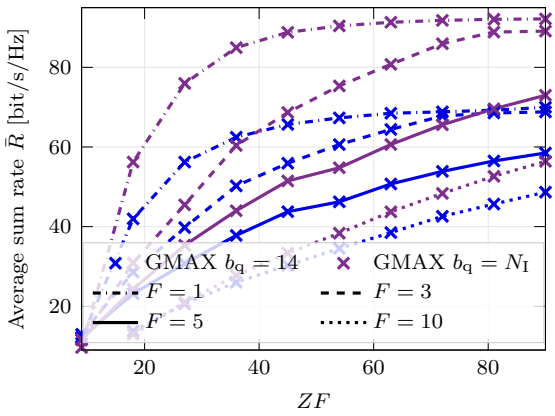

Figure 3.17: Average sum rate versus ZF, for $K = 90$ users, $F \in \{1, 3, 5, 10\}$.

rate as a function of and ZF. Since $1 \leq Z \leq KF$, the best performance is achievable for fewer frequencies, allowing for more frequent reconfigurations. Moreover, it is shown that for large Z the cases $F = \{1, 3\}$ exhibit very similar performance. This peculiar behavior is a direct consequence of the considered UMi cell, wherein $\sim 33\%$ of the users on average exhibit a LoS channel component. The channel gain experienced by such users is significantly larger than the gains of the user in NLoS. For $Z = K/3$, such users are allocated in different clusters and their optimal configurations are therefore chosen to serve their respective clusters. Thus, $Z = K/3$ is enough to obtain a high sum rate performance.

3.6 Summary

In this chapter, our investigation focused on a MIMO cellular network, where the BS experiences deep blockage in serving the associated users. To overcome such blockage, an IRS is used for the downlink transmissions to the users. We first developed and implemented a TDMA-based transmission strategy, aiming to optimize the average sum capacity within the constraints of IRS reconfigurations in each time frame. Our approach initially involved an iterative algorithm to identify the optimal IRS configuration for each user. Then, we introduced a novel clustering-based scheduling technique, which grouped users based on either distance or achievable rate metrics, ensuring similar IRS configurations within each cluster. This strategy significantly reduced the IRS reconfigurations, as users in the same cluster shared identical IRS settings. Through extensive simulations, we evaluated the effectiveness of our clustering algorithms in terms of computational com-

plexity, sum capacity, and fairness, under different channel conditions of the IRS-users links.

Furthermore, we extended the work to the OFDMA downlink scheduling. We framed the challenge of maximizing the sum rate as an NP-complete generalized multi-knapsack problem and proposed a heuristic solution for simultaneous IRS configuration and resource distribution. This solution closely matched the maximum sum rate achievable by a more intricate GA-based method, thus confirming its practical applicability in such network scenarios.

Notably, our methods reduced the IRS reconfigurations per time frame, thus lowering overhead and boosting communication efficiency.

4

Uplink Non-Orthogonal Multiple Access

In this part of the thesis, we discuss the NOMA uplink transmissions in the context of MRA. In particular, the chapter focuses on unsourced random access (URA). Firstly, the main state-of-the-art URA schemes are presented in Section 4.1. Then, the considered URA scenario is discussed in Section 4.2. A detailed description of tensor-based modulation (TBM) is firstly presented in Section 4.3. Differently from the initial scheme originally proposed in [119], TBM is here combined with SIC and log-likelihood ratio (LLR)-based soft decoding, which both significantly improves the robustness and the decoding capability at the BS. Then, a novel scheme combining TBM and conventional power-domain NOMA, denoted as tensor-based plus coherent modulation (TBMC) **[29]**, is presented in Section 4.4. An analysis of the achievable degrees of freedom (DoF) of TBM and TBMC is presented in Section 4.5, and a performance comparison with the state-of-the-art MIMO-aided URA solutions is assessed in Section 4.6. Finally, Section 4.7 summarizes the chapter.

4.1 Unsourced Random Access Background

URA [18], [120] represents a shift from conventional managed and scheduled access methods to a more flexible and scalable approach, catering to the needs of emerging wireless communication scenarios with a vast number of connected devices. Differently from conventional multiple access paradigms URA focuses on the case of users transmitting very short payloads, leading to finite blocklength effects [121]. Only a small fraction of users are active at any given time, but the total number of active users can still be comparable

with the overall blocklength. Moreover, users transmit their messages in a NOMA GF fashion. The core concept of URA involves all potential users sharing a common codebook, which greatly simplifies the process at the BS as it only needs to decode a list of messages instead of identifying active users' identities, which are not linked to specific waveforms at the physical layer. This approach is particularly beneficial in scenarios where only a subset of a large set of potential users is active at any given time. Note that, in general, the URA setting is *non-coherent* [122] by definition, as the non-identification of the users implies the absence of each user's CSI at the BS. One of the key challenges in URA is the development of effective decoding algorithms, as the process involves the joint channel estimation and decoding of a large number of messages transmitted by multiple users over a shared medium. This process can be complex due to the interference among the signals from different users and the lack of prior knowledge about which users are active.

Within this framework, a variety of practical strategies have been proposed in the literature. Some URA solutions propose to split the channel resources into multiple slots in which a sub-message is encoded using an inner compressed sensing code. The sub-messages are then concatenated and further encoded using an outer code [123]–[126]. The decoder then combines an inner decoder solving a compressed sensing problem (using, e.g., approximate message passing (AMP) algorithms that are commonly adopted for the activity detection task [127]–[129]) and an outer decoder. A different class of approaches that are usually referred to as *pilot*-based schemes proposes to split the transmission resources into two parts. The first part contains a pilot sequence encoding a small part of the payload that is used at the decoder to estimate the active users' channels while the second part sees a modulation scheme whose decoder assumes the users' channels as known. Note that, in contrast to typical multiple access schemes, wherein pilots are associated with the user identities, pilot bits in URA are part of the payload, thus no additional overhead is required for pilot sequences. To avoid misunderstandings, we will refer in the sequel to such symbols as *unsourced signals*. Different decoding strategies for pilot-based schemes have been also proposed. For example, [130] uses an AMP algorithm to decode the unsourced signal and relies on a maximum-ratio combining (MRC) equalizer and a low rate forward error correction (FEC) for the second sub-slot. Alternatively, Gkagkos et al. use in their FASURA scheme [131] a simple energy detector to decode the unsourced signal and a scheme combining random spreading and single-user coding for the second slot. Moreover, the decoder uses interference cancellation in order to improve the decoding performance.

A different URA philosophy has been adopted in the TBM, initially proposed in [119]. In TBM, the transmitted symbols are rank-1 tensors so that the combination of the

superimposed signals at the BS becomes a tensor whose rank is equal to the number of active transmitting users. Additionally, the coded bits of each user are modulated by using Grassmanian sub-modulations in each tensor dimension of the rank-1 tensor. The main advantage of the TBM decoder is that the user separation can be efficiently carried out using tensor decomposition approaches and without relying on pilot sequences. Unfortunately, under practical constraints, the TBM receiver suffers from performance degradation due to the approximations needed to compute the LLR of the coded bits when the payload is much larger than the tensor sizes.

4.2 Unsourced Random Access Scenario

We consider K single-antenna devices, out of which only a subset of $K_\mathrm{a} \ll K$ are active simultaneously and aim at transmitting in the uplink to a common BS equipped with M antennas. Without loss of generality, we assume that the indices of active devices take values in the set $\{1, \ldots, K_\mathrm{a}\}$. Each active device $k \in \{1, \ldots, K_\mathrm{a}\}$ transmits a message $\boldsymbol{m}_k$ of length B bits. [1] Furthermore, we adopt a quasi-static Rayleigh fading model with uncorrelated channel coefficients between both users and receiving antennas that remain constant over the n channel resources (blocklength) used for the simultaneous transmissions.

Let $\boldsymbol{x}_k \in \mathbb{C}^n$ be the encoded and modulated transmit signal of user k normalized to have power $\|\boldsymbol{x}_k\|^2 = n$. Then, the received signal at the BS is

$$\boldsymbol{Y} = \sum_{k=1}^{K_\mathrm{a}} \boldsymbol{x}_k \boldsymbol{h}_k^\mathrm{T} + \boldsymbol{Z} = \boldsymbol{X}\boldsymbol{H}^\mathrm{T} + \boldsymbol{Z}, \tag{4.1}$$

where $\boldsymbol{Z} \in \mathbb{C}^{n \times M}$ is the AWGN matrix, whose entries are drawn independently from a circularly symmetric complex Gaussian distribution $\mathcal{CN}(0, \sigma_z^2)$, $\boldsymbol{h}_k \in \mathbb{C}^M$ captures the channel coefficients between user k and each antenna at the BS, which under the assumption of Rayleigh fading are distributed as $\mathcal{CN}(0, \gamma_k)$, where γ_k denotes the LSFC. In matrix form, symbols and channel vectors are stacked into matrices $\boldsymbol{X} = [\boldsymbol{x}_1, \ldots, \boldsymbol{x}_{K_\mathrm{a}}]$ and $\boldsymbol{H} = [\boldsymbol{h}_1, \ldots, \boldsymbol{h}_{K_\mathrm{a}}]$.

The performance of URA schemes is measured by the BS decoding capability. Upon the uplink transmissions, the BS produces a list $\hat{\mathcal{L}} = \{\hat{\boldsymbol{m}}_k : k = 1, \ldots, \hat{K}_\mathrm{a}\}$ of $\hat{K}_\mathrm{a}$ decoded

[1] Note that, in the URA framework, the number of active users accessing the medium simultaneously is typically assumed to be known. Only recently, URA with random activity has been analyzed from the information-theoretical perspective in [132]. Furthermore, asynchronous URA, wherein the users may overlap the transmissions only partially is recently gaining attraction [133], [134].

messages, which hopefully matches the list of transmitted packets $\mathcal{L}$. The misdetection and false alarm probabilities are defined, respectively, as

$$p_{\mathrm{md}} = \mathbb{E}\left[\frac{|\mathcal{L} \setminus \hat{\mathcal{L}}|}{K_{\mathrm{a}}}\right], \quad p_{\mathrm{fa}} = \mathbb{E}\left[\frac{|\hat{\mathcal{L}} \setminus \mathcal{L}|}{|\hat{\mathcal{L}}|}\right]. \tag{4.2}$$

In the following, we assume that the number of active users is known at the BS. The goal of the modulation design is to minimize the energy-per-bit to noise ratio $E_{\mathrm{b}}/N_0 = \frac{||\boldsymbol{x}_k||^2}{B\sigma_z^2}$ such that the decoding error probability P_{e} satisfies

$$P_{\mathrm{e}} \ = \min\{p_{\mathrm{md}} + p_{\mathrm{fa}}, 1\} \leq \epsilon, \tag{4.3}$$

for given n, K_{a}, B, M, and ϵ.

Note that the identity of the transmitting user can be included in the message with a total overhead $\lceil \log_2 K \rceil$ bits. In that case, the number of users K has an impact on the achieved spectral efficiency since the data payload is reduced to $B - \lceil \log_2 K \rceil$ per user. In the URA framework, such an aspect is ignored. Moreover, we stress that the number of active users K_{a} is known at the receiver, as commonly assumed in the URA literature.

4.3 Tensor Based Modulation

In TBM, each user's transmission corresponds to a rank-1 tensor. In this chapter, we merely consider tensors to be multi-dimensional data structures, which can be seen as the generalization of matrices to dimensions greater than 2. [2]

Tensor Order and Rank. The order (or mode, dimension) refers to the number of indices required to describe the tensor, which corresponds to the number of dimensions in the array representation of the tensor. For example, a scalar is a tensor of order 0, a vector is a tensor of order 1, and a matrix is a tensor of order 2. Instead, by definition, a tensor is said to be rank-r whenever r is the smallest integer such that the tensor can be written as a sum of r rank-1 tensors [136].

The TBM receiver observes a linear combination of the transmitted rank-1 tensors, each weighted by the channel coefficients between the users and the BS. This combination can be conceptualized as a tensor which is the sum of several rank-1 components, the number of which equals the count of active users, K_{a}. This tensor-based structure enables the receiver to distinguish between users via conventional tensor decomposition techniques,

[2]The exact tensor definition tensor requires the additional mathematical, such as covectors and multi-linearity, see [135] for a detailed introduction.

such as canonical polyadic decomposition (CPD), obviating the need for separate steps for activity detection or channel estimation. Indeed, the channels are jointly estimated by the receiver with the data.

The primary advantages of TBM include:

- The receiver can separate users without relying on pilot sequences. This approach effectively bypasses the complex task of designing pilot sequences for grant-free access and does not require knowledge about the discrete nature of the modulation.

- This scheme applies to a wide range of multiple-access channels, including AWGN and block-fading, and extends to multiple-antenna receivers. It benefits from spatial diversity without depending on specific assumptions about the fading distribution.

4.3.1 TBM Encoder

In the TBM scheme introduced in [119], the unsourced message $\boldsymbol{m}_k$ is first encoded with a FEC code and then modulated with TBM as follows. We stress that we treat tensors as multi-dimensional data structures. Specifically, let us consider a complex-valued tensor of order D (i.e., a D-dimensional matrix of complex scalars) of dimensions $n_1, \ldots, n_D$. Note that $\prod_{i=1}^{D} n_i$ scalars forming the tensor can also be stored sequentially in a vector [136, Sec. 2.4]. Indeed, the corresponding vectorization operator defines an isomorphism between the space of $(T_1, \ldots, T_D)$-dimensional tensors and the space of $\left(\prod_{i=1}^{D} T_i\right)$-dimensional vectors. For notational convenience, in the following, we use the vectorized representation while referring to algebraic arguments applying in the space of tensors.

Let us define $\boldsymbol{z} = \mathrm{vec}(\boldsymbol{Z}) \in \mathbb{C}^{Mn}$. The signal received at the BS with the n channel resources (4.1) can be rewritten in its vectorized form as

$$\boldsymbol{y} = \mathrm{vec}(\boldsymbol{Y}) = \sum_{k=1}^{K_\mathrm{a}} \boldsymbol{x}_k \otimes \boldsymbol{h}_k + \boldsymbol{z}. \tag{4.4}$$

Let us assume that n can be factorized as $n = \prod_{i=1}^{D} n_i$ for some $D \geq 2$ and $n_1, \ldots, n_D \geq 2$. The transmitted unsourced signal $\boldsymbol{x}_k$ is obtained as the vectorized representation of a rank-1 tensor of dimensions $n_1, \ldots, n_D$:

$$\boldsymbol{x}_k = \boldsymbol{a}_{k,1} \otimes \cdots \otimes \boldsymbol{a}_{k,D} \in \mathbb{C}^n \tag{4.5}$$

where each vector $\boldsymbol{a}_{k,i}$ belongs to a *sub-constellation*, i.e., a codebook of complex vectors satisfying some specific properties, denoted by $\mathcal{C}_i \subset \mathbb{C}^{n_i}$. Note that the resulting vector

constellation $\mathcal{C}$ is the discrete set

$$\mathcal{C} = \{\boldsymbol{a}_1 \otimes \ldots \otimes \boldsymbol{a}_D \text{ s.t. } \boldsymbol{a}_1 \in \mathcal{C}_1, \ldots, \boldsymbol{a}_D \in \mathcal{C}_D\}. \tag{4.6}$$

The noise-free received signal at the BS is

$$\boldsymbol{y}_0 = \sum_{k=1}^{K_\mathrm{a}} \boldsymbol{x}_k \otimes \boldsymbol{h}_k. \tag{4.7}$$

This formulation allows for the application of several tensor properties and decomposition techniques, as described in the following.

4.3.2 Tensor Decomposition and Discrete Identifiability

In TBM each user transmits a rank-1 tensor of order D, while $\boldsymbol{y}_0$ is the vector representation of a tensor of order $D+1$ and dimensions $n_1, \ldots, n_D, M$. From the tensor rank definition [136], $\boldsymbol{y}_0$ has rank at most K_a. TBM is motivated by the fact that the decomposition of a tensor into a sum of rank-1 components (known as the CPD) is unique up to a permutation over the components under mild conditions. Furthermore, tensors of order 3 or more can attain high rank even for moderate tensor sizes. Therefore, TBM can achieve a high degree of multiplexing while using the CPD to separate the signal components related to each user.

To support the effectiveness of the proposed encoding scheme, we now introduce the properties of *CPD uniqueness* and *discrete identifiability* of the noise-free tensor $\boldsymbol{y}_0$.

CPD Uniqueness and Rank. The $(n_1, \ldots, n_D, M)$-dimensional tensor represented by $\boldsymbol{y}_0$ admits a unique rank-K_a CPD if for any set $\{\boldsymbol{a}'_{k,1} \in \mathbb{C}^{n_1}, \ldots, \boldsymbol{a}'_{k,D} \in \mathbb{C}^{n_D}, \boldsymbol{h}'_k \in \mathbb{C}^M, 1 \leq k \leq K'_\mathrm{a}\}$ with $K'_\mathrm{a} \leq K_\mathrm{a}$ such that

$$\sum_{k=1}^{K'_\mathrm{a}} \boldsymbol{a}'_{k,1} \otimes \cdots \otimes \boldsymbol{a}'_{k,D} \otimes \boldsymbol{h}'_k = \boldsymbol{y}_0, \tag{4.8}$$

then we have $K'_\mathrm{a} = K_\mathrm{a}$ and there exists a permutation σ such that $\boldsymbol{a}'_{k,1} \otimes \cdots \otimes \boldsymbol{a}'_{k,D} \otimes \boldsymbol{h}'_k = \boldsymbol{a}_{\sigma(k),1} \otimes \cdots \otimes \boldsymbol{a}_{\sigma(k),D} \otimes \boldsymbol{h}_{\sigma(k)}$.

According to [137, Th. 1.1], there exists an upper bound $\bar{R}$ to the rank of uniquely decomposable tensors, in the sense that the set of rank- K_a tensors for which the CPD is not unique has measure zero if $K_\mathrm{a} < \bar{R}$. Let us restate the main result of [137] using our notations. For tensors of size $n_1, \ldots, n_D, M$, let us assume without loss of generality that

$n_1 \geq n_2 \geq \cdots \geq n_D$ and define the *expected generic rank* [20], [137] as

$$R^0 = \left\lceil \frac{nM}{M + \sum_{i=1}^{D} (n_i - 1)} \right\rceil, \tag{4.9}$$

and

$$\begin{aligned} R^1 &= 2 - M + M \prod_{i=2}^{D} n_i - \sum_{i=2}^{D} (n_i - 1), \\ R^2 &= 1 + n - \sum_{i=1}^{D} (n_i - 1). \end{aligned} \tag{4.10}$$

According to [137, Th. 1.1], we have

$$\bar{R} = \begin{cases} R^1 - 1 & \text{for } n_1 \geq R^1 \\ R^2 - 1 & \text{for } M \geq R^2 \\ R^0 & \text{otherwise.} \end{cases} \tag{4.11}$$

Note that the tensor decomposition is here considered in a continuous domain, i.e., $\boldsymbol{a}_{k,i} \in \mathbb{C}^{n_i}$. To take into account takes into account the discrete nature of the $\mathcal{C}_i$, we refer to the discrete identifiability property.

Discrete identifiability. The noise-free received tensor is said to be *identifiable in the discrete case* [137] if for any set $\{\boldsymbol{a}'_{k,1} \otimes \cdots \otimes \boldsymbol{a}'_{k,D} \in \mathcal{C}, \boldsymbol{h}'_k \in \mathbb{C}^M, 1 \leq k \leq K'_{\mathrm{a}}\}$ with $K'_{\mathrm{a}} \leq K_{\mathrm{a}}$ and

$$\sum_{k=1}^{K'_{\mathrm{a}}} \boldsymbol{a}'_{k,1} \otimes \cdots \otimes \boldsymbol{a}'_{k,D} \otimes \boldsymbol{h}'_k = \boldsymbol{y}_0 \tag{4.12}$$

then it holds that $K'_{\mathrm{a}} = K_{\mathrm{a}}$ and there exists a permutation σ such that $\boldsymbol{a}'_{k,i} = \boldsymbol{a}_{\sigma(k),i}$ and $\boldsymbol{h}'_k = \boldsymbol{h}_{\sigma(k)}$.

Design of the Sub-Constellations. We now discuss the design of the information-bearing sub-constellations $\mathcal{C}_1, \ldots, \mathcal{C}_D$. Observe that the rank-1 tensor

$$\boldsymbol{a}_{k,1} \otimes \cdots \otimes \boldsymbol{a}_{k,D} \otimes \boldsymbol{h}_k = \alpha_1 \boldsymbol{a}_{k,1} \otimes \cdots \otimes \alpha_D \boldsymbol{a}_{k,D} \otimes \alpha_{D+1} \boldsymbol{h}_k, \tag{4.13}$$

with $\alpha_1, \ldots, \alpha_{D+1} \in \mathbb{C}$ whenever $\prod_{i=1}^{D+1} \alpha_i = 1$. This indicates that, even if the CPD perfectly recovers the rank-1 component associated with each transmitter, the information-bearing components $\boldsymbol{a}_{k,1}, \ldots, \boldsymbol{a}_{k,D}$ can only be retrieved up to a set of D complex scalar multiplicative coefficients, effectively providing D parallel (non-interfering) non-coherent

SISO blockfading channels to each active user. To account for this scalar indeterminacy, each sub-constellation $\mathcal{C}_i$ can either i) embed at least one reference symbol, or ii) rely on a Grassmannian codebook design suitable for the single-user non-coherent block-fading case [138], [139]. In particular, as the original TBM scheme described in [119], here we adopt the so-called cube-split modulation introduced in [139]. The cube-split vector constellation involves dividing the Grassmannian of lines using bent cubes and mapping Euclidean coordinates onto these cubes. Its advantages include high packing efficiency with larger minimum distance than existing structures, comparable to theoretical limits and it supports accurate LLR approximation. We refer the reader to [139] for details.

We remark that because of the unsourced nature of the scheme, the case of several users transmitting the same payload leads to a failure in the discrete identifiability of $\boldsymbol{y}_0$. However, as noted in [18], this occurs with low probability when the payload size B is large and can be completely avoided if the payload includes a unique user identifier.

Moreover, the discrete identifiability condition is more appropriate for the communications problem at hand, while the CPD uniqueness condition is unnecessarily strong, as there might be tensors that are discretely identifiable but do not admit a unique CPD. Still, the CPD uniqueness is relevant since i) it constitutes a sufficient condition for discrete identifiability, and ii) it is independent from the design of the discrete constellation $\mathcal{C}$.

4.3.3 TBM Decoder

When K_a is known at the receiver, the joint maximum likelihood (ML) multi-user detection and channel estimation problem of the unsourced transmissions is defined as

$$\{\hat{\boldsymbol{a}}_{k,i}, \hat{\boldsymbol{h}}_k\} = \underset{\substack{\{\boldsymbol{a}_{k,i}\in\mathcal{C}_i\}\\ \boldsymbol{h}_k\in\mathbb{C}^M}}{\operatorname{argmin}} \left\| \boldsymbol{y} - \sum_{k=1}^{K_\mathrm{a}} \boldsymbol{x}_k \otimes \boldsymbol{h}_k \right\|^2. \tag{4.14}$$

Solving (4.14) directly requires an exhaustive search with 2^{BK_a} evaluations of the objective function, thus the exhaustive search is unfeasible for practical values of K_a. To reduce the computational complexity, we split (4.14) into the *user separation* and the *single-user decoding* tasks. Let us first consider the continuous relaxation of problem (4.14), wherein $\boldsymbol{a}'_{k,1}, \ldots, \boldsymbol{a}'_{k,D}$ are not chosen from the discrete constellation but from $\mathbb{C}^{n_1}, \ldots, \mathbb{C}^{n_D}$, re-

spectively. We have

$$\{\hat{\boldsymbol{a}}'_{k,i}, \hat{\boldsymbol{h}}_k\} = \underset{\substack{\boldsymbol{a}'_{k,i}\in\mathbb{C}^{n_i} \\ \boldsymbol{h}_k\in\mathbb{C}^M}}{\operatorname{argmin}} \left\| \boldsymbol{y} - \sum_{k=1}^{K_\mathrm{a}} \boldsymbol{a}'_{k,1} \otimes \ldots \otimes \boldsymbol{a}'_{k,D} \otimes \boldsymbol{h}_k \right\|^2 \tag{4.15}$$

where $i = 1, \ldots, D$. The user separation problem (4.15) can be tackled with an approximate CPD algorithm to decompose the K_a-rank tensor $\boldsymbol{y}$ into K_a rank-1 tensors. Once the rank-1 components are separated, we can perform, independently for each user k, single-user decoding of all $\hat{\boldsymbol{a}}'_{k,i} \in \mathbb{C}^{n_i}$, $i = 1, ..., D$. To this end, we use soft demapping by computing the LLRs, which, assuming that the ℓ-th coded bit of user k, denoted by $b_{k,\ell}$, is among the set of bits mapped into $\boldsymbol{a}_{k,i}$, are defined as

$$\mathrm{LLR}_{k,\ell} = \log \frac{\mathbb{P}(b_{k,\ell} = 1 | \hat{\boldsymbol{a}}'_{k,i})}{\mathbb{P}(b_{k,\ell} = 0 | \hat{\boldsymbol{a}}'_{k,i})}. \tag{4.16}$$

An approximated closed-form expression for the LLRs in (4.16) has been derived in [140] and it is further simplified here as

$$\mathrm{LLR}_{k,\ell} \approx \begin{cases} \left(|\hat{\boldsymbol{a}}'^{\dagger}_{k,i} \hat{\boldsymbol{a}}_{k,i}| - |\hat{\boldsymbol{a}}'^{\dagger}_{k,i} \hat{\boldsymbol{a}}^{\mathrm{flip},\ell}_{k,i}| \right) \hat{\eta}_{k,i} & \text{if } \hat{b}_{k,\ell} = 1, \\ \left(|\hat{\boldsymbol{a}}'^{\dagger}_{k,i} \hat{\boldsymbol{a}}^{\mathrm{flip},\ell}_{k,i}| - |\hat{\boldsymbol{a}}'^{\dagger}_{k,i} \hat{\boldsymbol{a}}_{k,i}| \right) \hat{\eta}_{k,i} & \text{if } \hat{b}_{k,\ell} = 0, \end{cases} \tag{4.17}$$

where $\hat{\boldsymbol{a}}_{k,i} = \arg\max_{\boldsymbol{a}_i \in \mathcal{C}_i} |\hat{\boldsymbol{a}}'^{\dagger}_{k,i} \boldsymbol{a}_i|$ is the closest codeword to $\hat{\boldsymbol{a}}'_{k,i}$, $\hat{b}_{k,\ell}$ is the ℓ-th bit corresponding to $\hat{\boldsymbol{a}}'_{k,i}$ and $\hat{\boldsymbol{a}}^{\mathrm{flip},\ell}_{k,i}$ is the codeword corresponding to the estimated bit sequence with a flipped ℓ-th bit. Moreover, $\hat{\eta}_{k,i}$ denotes an approximated inverse of the variance computed as (see [140])

$$\hat{\eta}_{k,i} = \frac{||\hat{\boldsymbol{h}}_k||^2 n}{(n_i - 1)\sigma_z^2}. \tag{4.18}$$

The FEC decoder of user k takes as input all the terms $\mathrm{LLR}_{k,\ell}, 1 \leq \ell \leq B_c$ and gives as output the estimated messages. Messages with invalid cyclic redundancy check (CRC) are discarded from the estimated messages set. In general, at iteration l, $\hat{K}_{\mathrm{a},l} \leq K_\mathrm{a}$ messages are correctly decoded in the n unsourced signals resources. Each decoded bit sequence is subsequently re-encoded and modulated as in (4.5). If $\hat{K}_{\mathrm{a},l} < K_\mathrm{a}$ the SIC step detailed in Section 4.4.3 is applied to obtain $\boldsymbol{y}^{l+1}$ and the procedure is repeated while $l \leq l^{\max}$. If, instead, $\hat{K}_{\mathrm{a},l} = K_\mathrm{a}$, the TBM inner decoding loop is stopped, and the estimated channels and messages are passed to the coherent signals decoder.

4.4 Tensor Based Plus Coherent Modulation

The main drawback of TBM is that, under practical constraints, the receiver suffers from performance degradation due to the approximations needed to compute the LLR of the coded bits when the payload is much larger than the tensor sizes. To overcome these limitations, we present the novel TBMC scheme, which allows to overcome the payload size limitations of the original TBM and, thus, extends its applicability to a wider range of scenarios. TBMC results from the concatenation of two signals:

- a first *unsourced signal* encoded as a TBM vector symbol responsible for the channel estimation, and carrying a fraction of the message,
- a second *coherent signal* encoded and transmitted using a NOMA scheme that carries the remaining fraction of the user message and is decoded after channel estimation.

Observe that the above structure is similar to that of pilot-based schemes with the particularity that the unsourced signal is a TBM vector symbol. In the following, we discuss in detail the TBMC encoder and decoder.

4.4.1 TBMC Encoder

First, the encoder divides the resource block into a first sub-block of n_{u} resources for the unsourced transmissions and a second sub-block of n_{c} resources for coherent signals transmissions, such that $n = n_{\mathrm{u}} + n_{\mathrm{c}}$. Accordingly, the bit sequence to be transmitted by user k is split into two parts $\boldsymbol{m}_k^{\mathrm{u}}$ and $\boldsymbol{m}_k^{\mathrm{c}}$, of length B_{u} and B_{c}, respectively (so that $B_{\mathrm{u}} + B_{\mathrm{c}} = B$). The messages $\boldsymbol{m}_k^{\mathrm{u}}$ and $\boldsymbol{m}_k^{\mathrm{c}}$ are then encoded into the symbol vectors $\boldsymbol{x}_k^{\mathrm{u}}$ and $\boldsymbol{x}_k^{\mathrm{c}}$, respectively. Finally, the transmitted signal $\boldsymbol{x}_k$ is given by the concatenation of the unsourced and coherent signals, i.e.,

$$\boldsymbol{x}_k = \begin{bmatrix} \boldsymbol{x}_k^{\mathrm{u}} \\ \boldsymbol{x}_k^{\mathrm{c}} \end{bmatrix} \in \mathbb{C}^n \quad \text{with} \quad \boldsymbol{x}_k^{\mathrm{u}} \in \mathbb{C}^{n_{\mathrm{u}}}, \quad \boldsymbol{x}_k^{\mathrm{c}} \in \mathbb{C}^{n_{\mathrm{c}}}. \tag{4.19}$$

Therefore, the received signal in (4.1) can be rewritten as the concatenation of the two signals:

$$\boldsymbol{Y} = \begin{bmatrix} \boldsymbol{Y}^{\mathrm{u}} \\ \boldsymbol{Y}^{\mathrm{c}} \end{bmatrix} = \sum_{k=1}^{K_{\mathrm{a}}} \begin{bmatrix} \boldsymbol{x}_k^{\mathrm{u}} \\ \boldsymbol{x}_k^{\mathrm{c}} \end{bmatrix} \boldsymbol{h}_k^{\mathrm{T}} + \begin{bmatrix} \boldsymbol{Z}^{\mathrm{u}} \\ \boldsymbol{Z}^{\mathrm{c}} \end{bmatrix}, \tag{4.20}$$

where $\boldsymbol{Z}^{\mathrm{u}}$ and $\boldsymbol{Z}^{\mathrm{c}}$ are the AWGN components affecting the unsourced and coherent received signals, respectively.

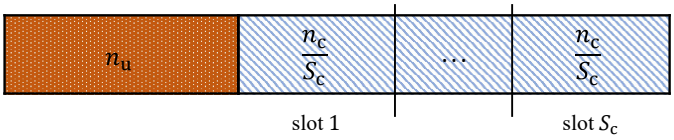

Figure 4.1: TBMC resource block splitting.

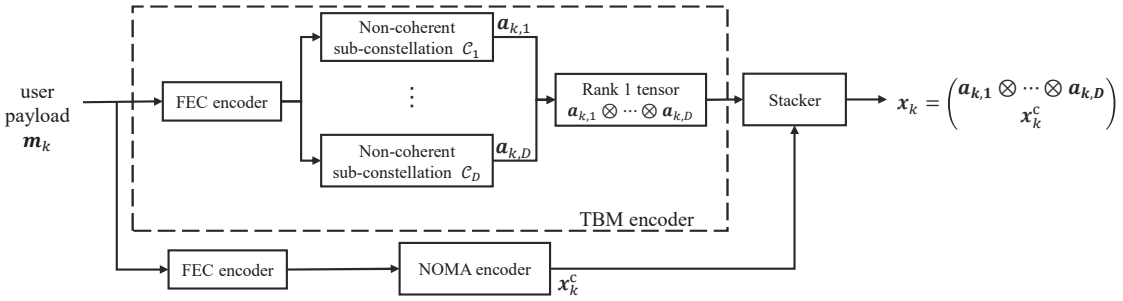

Figure 4.2: TBMC encoder structure. The payload bits are first split into unsourced and coherent bits. Both the bits sequences are independently encoded with a FEC code. The unsourced part is encoded according to TBM, and the coherent bits are instead encoded with the coherent NOMA encoder. The obtained complex symbols a recombined and transmitted over the channel.

Let us define $\boldsymbol{z}^\mathrm{u} = \mathrm{vec}(\boldsymbol{Z}^\mathrm{u}) \in \mathbb{C}^{Mn_\mathrm{u}}$. For convenience, we reformulate the signal received at the BS in the first sub-block with the n_u channel resources reserved for the unsourced signals in its vectorized form as

$$\boldsymbol{y}^\mathrm{u} = \mathrm{vec}(\boldsymbol{Y}^\mathrm{u}) = \sum_{k=1}^{K_\mathrm{a}} \boldsymbol{x}_k^\mathrm{u} \otimes \boldsymbol{h}_k + \boldsymbol{z}^\mathrm{u}. \tag{4.21}$$

On the other hand, the received signal in the second sub-block with the remaining n_c resources, can be rearranged in matrix form as

$$\boldsymbol{Y}^\mathrm{c} = \boldsymbol{X}^\mathrm{c} \boldsymbol{H}^\mathrm{T} + \boldsymbol{Z}^\mathrm{c}. \tag{4.22}$$

NOMA Encoder for Coherent Signals. For the coherent part we resort to the unified NOMA framework introduced in [17], wherein data bits are first encoded with a FEC code and then modulated according to an arbitrary coherent modulation. Specifically, we assume that the set of resources for coherent transmissions is split into S_c slots of equal size $n_\mathrm{s} = n_\mathrm{c}/S_\mathrm{c}$. Then, user k selects the slot for transmission based on the unsourced messages as $s_k = \delta(\boldsymbol{m}_k^\mathrm{u})$, where $\delta : \{0,1\}^{B_\mathrm{u}} \to [S_\mathrm{c}]$ is a map such that the sets $\delta^{-1}(\{s\})$ are of equal size for all $s = 1, \ldots, S_\mathrm{c}$. Finally, the coherent part of the message $\boldsymbol{m}_k^c$ is encoded with a FEC code and modulated using quadrature amplitude modulation (QAM).

Let $\boldsymbol{q}_k$ denote the n_s-dimensional vector collecting the QAM symbols from user k, then the transmitted coherent signal takes the form

$$\boldsymbol{x}_k^\mathrm{c} = (\boldsymbol{e}_{s_k} \otimes \boldsymbol{I}_{n_\mathrm{s}})\boldsymbol{q}_k, \tag{4.23}$$

where $\boldsymbol{e}_{s_k} \in \mathbb{R}^{S_\mathrm{c}}$ is a vector with 1 in position s_k and 0 elsewhere.

A representation of the resulting TBMC resource block is depicted in Fig 4.1. The resources for unsourced signals are orange-colored with a dotted pattern. The blue part with parallel diagonal lines pattern represents the resources for NOMA coherent transmissions, split in S_c slots of equal size. Fig. 4.2 shows a block diagram summarizing the encoding procedure performed at each user.

4.4.2 TBMC Decoder

The BS decoding task is carried out iteratively, performing a sequence of sub-tasks. First, the received unsourced signal is decoded performing a CPD-based user separation (which also allows for the channel estimation), followed by a LLR-based FEC decoding and SIC steps. The decoded unsourced signals and the estimated channel vectors are used as input to the NOMA decoder, which performs linear minimum mean squared error (LMMSE) estimation of the received symbols, as well as FEC decoding and SIC. Finally, the messages are re-combined and re-encoded to obtain the channel inputs and perform a final SIC step. This procedure is repeated until the decoder either reaches a maximum number of performed iterations or decodes exactly K_a messages. Overall, the decoder implements three SIC iterative procedures: one for the unsourced signals, one for the coherent signals transmissions, and an outer iterative procedure nesting such loops. In the following, we denote the corresponding iterations indices as l_u, l_c, and l, respectively.

NOMA Decoder for Coherent Signals. Upon the decoding of the unsourced messages, the NOMA decoder aims at obtaining the transmitted coherent messages, given the estimated channel vectors $\hat{\boldsymbol{h}}_k$ and the already decoded unsourced messages $\hat{\boldsymbol{m}}_k^\mathrm{u}$, $k = 1, \ldots, \hat{K}_{\mathrm{a},l_\mathrm{u}}$ at the last iteration performed by the TBM decoder. The estimated slots used for the coherent signals transmissions $\hat{s}_k$, $k = 1, \ldots, \hat{K}_{\mathrm{a},l_\mathrm{u}}$ are obtained from the already decoded unsourced messages as $\hat{s}_k = \delta(\hat{\boldsymbol{m}}_k^\mathrm{u})$, $k = 1, \ldots, \hat{K}_{\mathrm{a},l_\mathrm{u}}$. Let s be a generic slot index, and $\hat{\boldsymbol{H}}_s$ the matrix whose columns are the channel vectors $\hat{\boldsymbol{h}}_k$ such that $\hat{s}_k = s$. An LMMSE filter is applied to retrieve the QAM symbols transmitted by each active user in each slot s as

$$[\hat{\boldsymbol{x}}_1^\mathrm{c}, \cdots, \hat{\boldsymbol{x}}_{\hat{k}_s}^\mathrm{c}]^\mathrm{T} = (\hat{\boldsymbol{H}}_s^\dagger \hat{\boldsymbol{H}}_s + \sigma_z^2 \boldsymbol{I}_{\hat{k}_s})^{-1} \hat{\boldsymbol{H}}_s^\dagger \boldsymbol{Y}_s^\mathrm{c}, \tag{4.24}$$

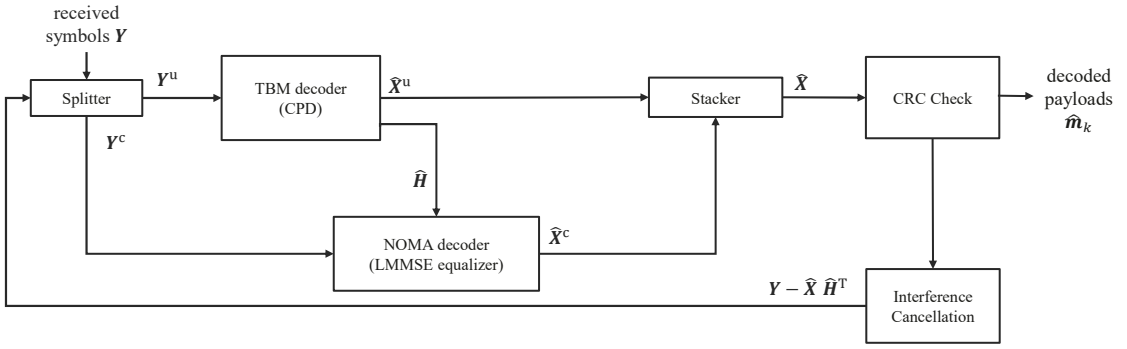

Figure 4.3: TBMC decoder structure. The received signal is firstly split into an unsourced and a coherent part. While the former is processed with an iterative TBM decoder, the latter is passed to the coherent NOMA decoder which also takes as inputs the channels estimated with the unsourced part decoding. The signal is finally recombined, and the interference cancellation step is applied.

where $\hat{k_s}$ is the estimated number of users transmitting in slot s and $\boldsymbol{Y}_s^{\mathrm{c}}$ is the coherent part of the signal received in slot s. Similarly to the TBM decoder, the symbols in (4.24) are passed to a LLR-based FEC decoder that outputs the estimated coherent messages $\hat{\boldsymbol{m}}_k^{\mathrm{c}}$, $k = 1, \ldots, \hat{K}_{\mathrm{a},l_{\mathrm{c}}}$, with $\hat{K}_{\mathrm{a},l_{\mathrm{c}}} \leq \hat{K}_{\mathrm{a},l_{\mathrm{u}}}$. Once again, interference cancellation (see Section 4.4.3) is applied to obtain $\boldsymbol{Y}_{l_{\mathrm{u}}+1}^{\mathrm{c}}$ if $\hat{K}_{\mathrm{a},l_{\mathrm{c}}} < \hat{K}_{\mathrm{a},l_{\mathrm{u}}}$. The decoding loop is stopped when the number of decoded unsourced and coherent messages coincides, or the maximum number of iterations $l_{\mathrm{c}}^{\max}$ is reached.

Final Concatenation and SIC. At each iteration of the outer loop l, upon the decoding of both the unsourced and coherent parts a list of messages $\hat{\boldsymbol{m}}_k = [\hat{\boldsymbol{m}}_k^{\mathrm{u}}, \hat{\boldsymbol{m}}_k^{\mathrm{c}}]$, for $k = 1, \ldots, \hat{K}_{\mathrm{a},l_{\mathrm{c}}}$, is built. If $\hat{K}_{\mathrm{a},l_{\mathrm{c}}^{max}} < \hat{K}_{\mathrm{a},l_{\mathrm{u}}}$, one or more coherent signals were not decoded. In this case, the respective unsourced bit messages are dropped. As a final step SIC is applied to the combined received signals to obtain $\boldsymbol{Y}_{l+1}$, and the outer loop keeps iterating until $l = l^{\max}$ or K_{a} messages are decoded.

The decoding procedure is summarized in the scheme of Fig. 4.3.

4.4.3 Successive Interference Cancellation

Recall that an interference cancellation step is applied at each iteration of each loop in the decoding process. At given generic iteration ν, a set of $\hat{K}_{\mathrm{a},\nu}$ messages are decoded. Those messages are re-encoded with the same FEC and modulated according to the procedures explained in Section 4.4.1 to obtain the generic channel input $\hat{\boldsymbol{X}}$. Then, the channels are estimated with LMMSE as

$$\hat{\boldsymbol{H}} = (\hat{\boldsymbol{X}}\hat{\boldsymbol{X}}^{\dagger} + \sigma_z^2 \boldsymbol{I}_M)^{-1} \hat{\boldsymbol{X}}^{\dagger} \boldsymbol{Y} \tag{4.25}$$

Algorithm 4.1 TBMC iterative decoder

Require: $\boldsymbol{Y}$
Ensure: $\hat{\boldsymbol{h}}_k$, $\hat{\boldsymbol{x}}_k$, $\hat{\boldsymbol{m}}_k$, $\forall k$

for $l = 1, \ldots, l^{\max}$
  for $l_{\mathrm{u}} = 1, \ldots, l_{\mathrm{u}}^{\max}$
    $\{\hat{\boldsymbol{v}}_{k,i}, \hat{\boldsymbol{h}}_k\} \leftarrow$ CPD on $\boldsymbol{y}_{l_{\mathrm{u}}}^{\mathrm{u}}$ to solve (4.15)
    $\hat{\boldsymbol{m}}_k^{\mathrm{u}}$, $k = 1, \ldots, \hat{K}_{\mathrm{a},l_{\mathrm{u}}} \leftarrow$ FEC decoding on $\{\hat{\boldsymbol{v}}_{k,i}\}$
    if $\hat{K}_{\mathrm{a},l_{\mathrm{u}}} = K_{\mathrm{a}}$
      STOP inner loop
    else
      $\boldsymbol{Y}_{l_{\mathrm{c}}+1}^{\mathrm{c}} \leftarrow$ SIC step
    end if
  end for
  compute $\hat{s}_k = \delta(\hat{\boldsymbol{m}}_k^{\mathrm{u}})$, for $k = 1, \ldots, \hat{K}_{\mathrm{a},l}$
  for $l_{\mathrm{c}} = 1, \ldots, l_{\mathrm{c}}^{\max}$
    for $s = 1, \ldots, S_{\mathrm{c}}$
      $\hat{\boldsymbol{x}}_k^{\mathrm{c}} \leftarrow$ LMMSE estimate (4.24) for $k: \ s = s_k$
    end for
    $\hat{\boldsymbol{m}}_k^{\mathrm{c}}$, $k = 1, \ldots, \hat{K}_{\mathrm{a},l_{\mathrm{c}}} \leftarrow$ FEC decoding on $\hat{\boldsymbol{x}}_k^{\mathrm{c}}$
    if $\hat{K}_{\mathrm{a},l_{\mathrm{c}}} = \hat{K}_{\mathrm{a},l_{\mathrm{u}}}$
      STOP inner loop
    else
      $\boldsymbol{Y}_{l_{\mathrm{c}}+1}^{\mathrm{c}} \leftarrow$ SIC step
    end if
  end for
  $\hat{\boldsymbol{m}}_k \leftarrow [\hat{\boldsymbol{m}}_k^{\mathrm{u}}, \hat{\boldsymbol{m}}_k^{\mathrm{c}}]$, for $k = 1, \ldots, \hat{K}_{\mathrm{a},l_{\mathrm{c}}}$
  $\boldsymbol{Y}_{l_{\mathrm{c}}+1}^{\mathrm{c}} \leftarrow$ SIC step
end for

and the interference is mitigated by subtracting the contribution of the users being already decoded as

$$\boldsymbol{Y}_{\nu+1} = \boldsymbol{Y}_{\nu} - \hat{\boldsymbol{X}}\hat{\boldsymbol{H}}^{\mathrm{T}}. \tag{4.26}$$

The SIC-based decoding procedure is summarized in Algorithm 4.1.

4.5 Degrees of Freedom Analysis

The concept of DoF in the context of MIMO systems refers to the maximum number of independent data streams that can be simultaneously transmitted and received over a communication channel. To establish the number of DoF achievable by TBM and TBMC, let us consider the case of asymptotically high SNR, assuming that $\boldsymbol{y}_0$ is available at the receiver. The DoF achievability proof relies on a random coding argument, in the sense that we assume that the elements of the sub-constellations $\mathcal{C}_i$ and channel realizations $\boldsymbol{h}_k$ are independently drawn from absolutely continuous distributions. These two assumptions ensure that the received tensor is generic, for which case the CPD is almost surely unique whenever $K_{\mathrm{a}} < \bar{R}$. As a consequence, under these ideal assumptions, CPD allows to recover all the tensor components at the first decoding step, thus the decoding procedure does not affect the following DoF analysis.

Per-User DoF in the Unsourced Part. Focusing on the non-coherent TBM resources, note that the uniqueness of the CPD is defined in terms of the rank-1 components, however each factor $\boldsymbol{a}_{k,i}$ can only be recovered up to a complex scalar coefficient. Nonetheless, the uniqueness result can be extended to the sub-constellations by considering that the $\boldsymbol{a}_{k,i}$ are representatives of Grassmannian variables. More specifically, for all $1 \leq i \leq D$, let $G(n_i, 1)$ denote the Grassmannian of lines in dimension n_i, i.e., the set of 1-dimensional linear subspaces of $\mathbb{C}^{n_i}$, and let us consider x_i as a representative of the corresponding point in $G(n_i, 1)$. Note that every rank-1 component $\boldsymbol{a}_{k,1} \otimes \cdots \otimes \boldsymbol{a}_{k,D} \otimes \boldsymbol{h}_k$ maps to a unique point of $G(n_1, 1) \times \cdots \times G(n_D, 1) \times G(M, 1)$. Consequently, whenever $K_{\mathrm{a}} < \bar{R}$, the proposed scheme allows the noise-free communication of d complex Grassmannian variables in $G(n_1, 1) \dots G(n_D, 1)$ respectively, for each active user (the component in $G(M, 1)$ corresponds to the channel, and does not carry information). As shown in [138], a variable in $G(m, 1)$ has $m - 1$ DoF. Summing across the sub-constellations indicates that the TBM approach allows the noise-free communication of $\sum_{i=1}^{D}(n_i - 1)$ DoF per active user.

The total DoF achieved in the system is obtained by summing up the per-user DoF; therefore, it is a function of K_{a}. Since every active user contributes $\sum_{i=1}^{D}(n_i - 1)$ DoF

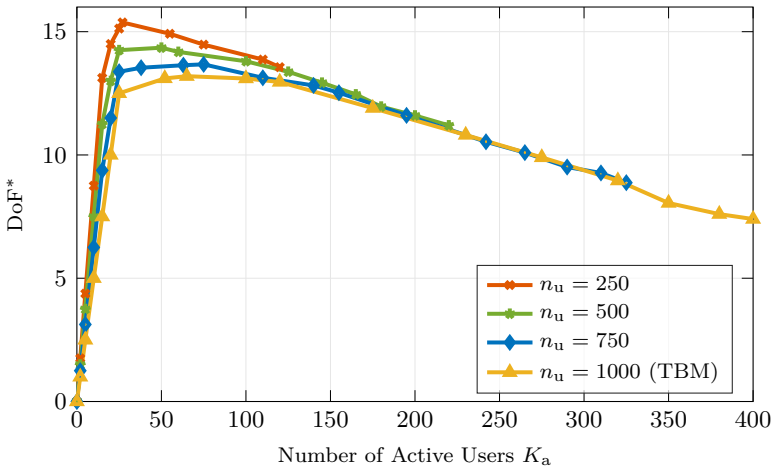

Figure 4.4: Sum-DoF per channel use, for TBM and TBMC, $n = 1000$ and $M = 16$.

up to the maximum number of users for which the rank- K_a tensor is almost surely identifiable in the discrete case, the sum-DoF is

$$\mathrm{DoF}_{\mathrm{TBM}}(K_a, n_1, \ldots, n_D) = K_a \sum_{i=1}^{D} (n_i - 1) \quad \text{for} \quad K_a \leq \bar{R} - 1. \tag{4.27}$$

Clearly, the highest sum-DoF is attained for $K_a = \bar{R}-1$, and is equal to $(\bar{R}-1)\sum_{i=1}^{D}(n_i - 1)$. Moreover, using the fact that

$$K_a \leq \bar{R} - 1 \leq R^0 - 1 < \frac{nM}{M + \sum_{i=1}^{d}(n_i - 1)}, \tag{4.28}$$

we can upper bound the DoF independently from the tensor size by

$$\mathrm{DoF}_{\mathrm{TBM}}(K_a, n_1, \ldots, n_D) < M(n - K_a). \tag{4.29}$$

Per-User DoF in the Coherent Part. In the multi-user single input-multiple output (SIMO) coherent setting, the DoF in a MIMO system is limited by the minimum between the number of receiver antennas and the number of transmitting users as

$$\mathrm{DoF}_{\mathrm{NOMA}}(K_a) = n_c \min(K_a, M). \tag{4.30}$$

The sum-DoF of TBMC is therefore given by,

$$\begin{aligned}\mathrm{DoF}_{\mathrm{TBMC}}(K_{\mathrm{a}}, n_1, \ldots, n_D) &= \mathrm{DoF}_{\mathrm{NOMA}}(K_{\mathrm{a}}) + \mathrm{DoF}_{\mathrm{TBM}}(K_{\mathrm{a}} n_1, \ldots, n_D) \\ &= n_{\mathrm{c}} \min(K_{\mathrm{a}}, M) + K_{\mathrm{a}} \sum_{i=1}^{D} (n_i - 1)\end{aligned} \tag{4.31}$$

which is bounded by $\bar{R} - 1$, as the coherent part depends on the channel estimation performed with TBM in the unsourced part.

Depending on the number of active users, antennas, and the number of resources, different tensor dimensions $n_1, \ldots, n_D$ should be considered to maximize the overall sum-DoF. Let

$$\mathrm{DoF}^*(K_{\mathrm{a}}) = \max_{n_1,\ldots,n_D} \mathrm{DoF}_{\mathrm{TBMC}}(K_{\mathrm{a}}, n_1, \ldots, n_D)/n, \tag{4.32}$$

be the maximum sum-DoF per channel use.

Fig. 4.4 shows the maximum sum-DoF per channel use for different resource splitting between unsourced and coherent resources. Note that, in the case $n_{\mathrm{u}} = 1000 = n$, TBMC coincides to TBM. Moreover, the shorter TBM section corresponds to a larger sum-DoF but a lower maximum supported number of active users. For this reason, depending on the number of available resources (blocklength) and the number of active users to support simultaneously, a different resource-splitting policy should be adopted. We remark that the optimality of the resource and payload splitting needs further investigation, as the analysis of the sum-DoF is limited to the balance between unsourced and coherent channel resources. Indeed, FEC, SIC, and soft decoding are not considered in the DoF analysis, and high sum-DoF performance may not correspond to a low decoding error probability.

4.6 Numerical Results

This section presents the numerical results comparing TBM and TBMC with two state-of-the-art URA solutions. We assume that the BS is equipped with $M = 16$ antennas and each active user transmits a message of $B = 200$ bits in a block of $n = 1000$ channel resources. In addition to the proposed TBMC strategy, we also consider the original TBM scheme in [119] using the TBM decoder described in Section 4.4.2. Note that this corresponds to TBMC with $n_{\mathrm{u}} = n$ and $B_{\mathrm{u}} = B$.

For completeness, we further include the pilot-based scheme in [130] and the FASURA scheme [131] in our numerical analysis, which are summarized as follows

Pilot-Based Scheme. In the pilot-based scheme of [130], the users' messages are divided into two sub-messages. The first B_{u}-bit sub-message is mapped to a complex codeword

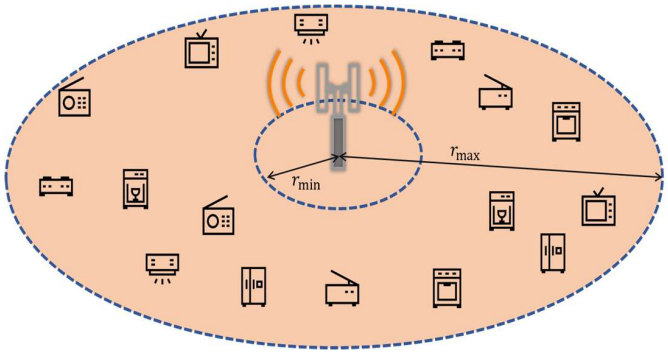

Figure 4.5: URA simulation setup. Users are uniformly spread in a disk with the BS at its center, with inner radius $r_{\min}$ and outer radius r_{out}.

chosen from a codebook of $2^{B_{\text{u}}}$ entries and length n_{u} (unsourced signal). The second sub-message, instead, is encoded with a low-rate polar code and modulated with a QPSK modulation. At the decoder, AMP is adopted for the unsourced signals, with ML estimation of the LSFCs performed in each multiple measurement vector (MMV)-AMP iteration. An LMMSE estimator is applied to estimate the channels of the active users. Then, in the second block MRC and successive cancellation list (SCL) polar decoding is adopted to recover the QPSK symbols.

FASURA Scheme. The FASURA scheme [131], from fading spread URA, consists of a pilot-based scheme combining spreading and single-user polar coding. FASURA divides the users' messages into two parts. The first B_{u}-bits are used to select operational parameters, such as the frozen bits and the interleaving pattern, while the second is encoded using a single-user code, depending on the first sub-message. Then, each symbol is spread before transmission. At the decoder, a simple energy detector is adopted, moreover, the spreading enables the computation of a LMMSE estimate of the coded unsourced signals, leveraging the active spreading sequences to mitigate interference during the decoding process. To enhance channel estimation, FASURA adopts noisy pilot channel estimation (NOPICE), which estimates the channel by utilizing both pilot signals and preliminary decisions about the coded symbols. Embedded within an iterative loop, this estimation technique progressively improves the accuracy of channel estimates when parameters are carefully selected.

FEC Code Details. All messages are encoded with a polar code [141] comprising CRC. At the receiver, the FEC decoder uses SCL decoding with a list of candidate codewords of length 32. A CRC validation step is applied to each codeword in the list and the most likely message among the ones succeeding the CRC check is returned. If no messages with

valid CRC are found in the list, no messages are outputted. The coding rate depends on the modulation specifications. On one hand, the TBM unsourced signals are adapted to the number of bits modulated with cube-split [139] in each tensor dimension. On the other hand, for the coherent signals, the code length is constrained by the number of resources per slot $n_{\mathrm{c}}/S_{\mathrm{c}}$.

URA Schemes Details. For TBMC we consider $n_{\mathrm{u}} = 500$, and $(n_1, n_2, n_3, n_4) = (5, 5, 5, 4)$ with 4 coded bits-per-dimension, i.e., 4 bits are mapped to a point in sub-constellation $\mathcal{C}_i$ (see [119], [139] for details). The number of bits encoded for unsourced signals is $B_{\mathrm{u}} = 40$. The sub-block of coherent signals resources for NOMA is split into $S_{\mathrm{c}} = 2$ slots and the QAM constellation size is set to 4. The TBM scheme is configured with $D = 2$ and $(n_1, n_2) = (40, 25)$ and 4 coded bits-per-real-dimension. The choice of this configuration was guided by the following remark. As shown in [119], TBM with smaller tensor dimensions can support more users, however, we are constrained by the payload size. The decoding performance drops significantly due to the approximation in the LLR computation as the sub-constellations become denser. We have observed in numerical results that Grassmannian constellations cannot support more than 4 coded bits per real dimension. For the pilot-based scheme proposed in [130], we consider 16 pilot bits, 360 pilot resources, a code length of 1280, and a SCL list of length 32. Finally, the FASURA scheme is configured with 16 pilot bits, 360 pilot resources, a code length of 256, a SCL list of length 64, and spreading sequences of length 5. The aforementioned URA solutions are also compared to the achievability bound derived in [142].

Decoder Complexity Comparison. In addition to the decoding performance, the decoding complexity plays a crucial role in URA, and therefore it has to be discussed. All the considered decoding algorithms implement SCL-based FEC decoders and, thus, its complexity can be excluded from the comparison. Moreover, all the compared algorithms require a different, but limited, number of iterations either for performing SIC, MMV-AMP, or CPD. In the comparison, we neglect this aspect for the sake of conciseness. For tensor-based schemes, the complexity is mainly dominated by the user separation task. The approximate CPD for both TBMC and TBM is here implemented using the Gauss-Newton algorithm with dog-leg trust region [143], which provides a complexity of $O(n_{\mathrm{u}}M + K_{\mathrm{a}}^3)$ and $O(nM + K_{\mathrm{a}}^3)$, respectively. Additionally, TBMC computes the LMMSE estimator for each NOMA slot, adding a complexity of $O(K_{\mathrm{a}}^3/S_{\mathrm{c}}^2)$. Instead, the complexity of the pilot-based scheme [130] is dominated by the MMV-AMP algorithm, which has complexity $O(n_{\mathrm{u}}M2^{B_{\mathrm{u}}})$ due to the matrix multiplication between the received symbol and the codebook matrix. Moreover, LMMSE is applied to estimate the channels

Table 4.1: Complexity comparison of MIMO-aided URA solutions

	Unsourced	Coherent
Pilot-based	$O(n_{\mathrm{u}}M2^{B_{\mathrm{u}}})$	$O(n_{\mathrm{c}}MK_{\mathrm{a}})$
FASURA	$O(K_{\mathrm{a}}^3)$	$O(T_{\mathrm{spread}}K_{\mathrm{a}}^3)$
TBM	$O(nM + K_{\mathrm{a}}^3)$	$O(1)$
TBMC	$O(n_{\mathrm{u}}M + K_{\mathrm{a}}^3)$	$O(K_{\mathrm{a}}^3/S_{\mathrm{c}}^2)$

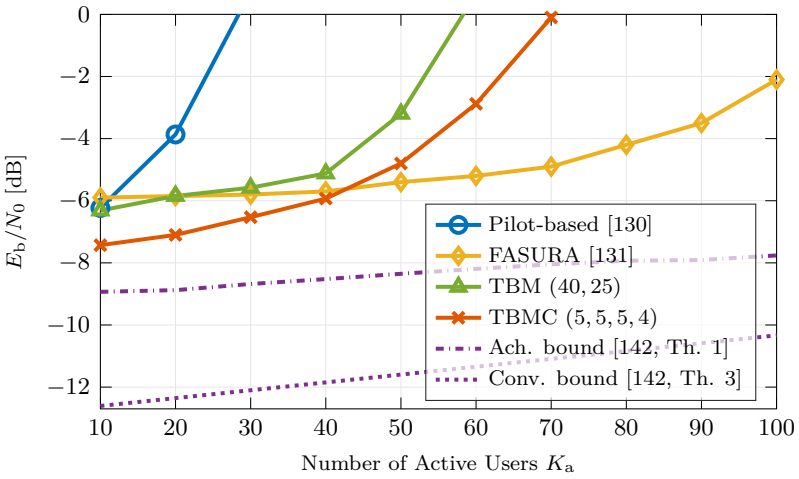

Figure 4.6: Average minimum E_{b}/N_0 required to achieve $P_{\mathrm{e}} \leq 0.1$ versus K_{a}, for $n = 1000$ and $M = 16$.

and maximum-ratio combining to recover the coherent signals. While the former requires singular value decomposition with a complexity of $O(n_{\mathrm{u}}^3)$, the latter is a product of three matrices, having complexity $O(n_{\mathrm{c}}MK_{\mathrm{a}})$. Note that the complexity of MMV-AMP can be reduced to $O(n_{\mathrm{u}}MB_{\mathrm{u}})$ by adopting a DFT codebook. Finally, for FASURA, the complexity is dominated by the symbol estimator. The decoder performs an LMMSE for each spreading sequence matrix, leading to a total complexity of $O(T_{\mathrm{spread}}K_{\mathrm{a}}^3)$, where T_{spread} is the number of spreading sequence matrices.

In Table 4.1, we summarize the complexity of each of the compared schemes, distinguishing the complexity of the decoding task for the unsourced and the coherent resources. On one hand, we observe that the complexity of TBM, TBMC, and the pilot-based scheme is mainly due to the decoding of the unsourced signals. On the other hand, the FASURA scheme, for which T_{spread} is proportional to the number of coded bits, has higher complexity in the NOMA decoding. Note that the decoder complexity strictly depends on the application and the considered parameters, therefore it is not easy to declare which of the considered schemes has the lowest complexity.

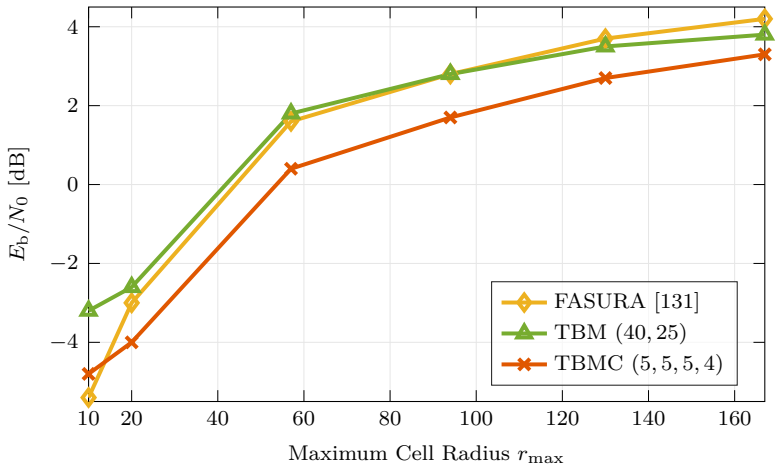

Figure 4.7: Average minimum E_b/N_0 required to achieve $P_e \leq 0.1$ versus r_{max}, for $n = 1000$ and $M = 16$.

Energy Efficiency Performance. The energy efficiency of the URA schemes is measured as the minimum E_b/N_0 required to satisfy the P_e constraint in (4.3). Fig. 4.6 shows the empirical average minimum E_b/N_0 required to satisfy this constraint for $\epsilon = 0.1$ as a function of the number of active users K_a. All LSFCs γ_k are set to 1, for all k. Firstly, we observe that the $(5, 5, 5, 4)$ TBMC outperforms TBM in all activation conditions, while the $(25, 20)$ is a valid solution only if few users are active simultaneously. In comparison with FASURA, we observe that the proposed scheme allows greater energy efficiency for low numbers of active users, while FASURA seems to be more efficient in case of high system load. Indeed, the limitations of tensor-based schemes, when the number of users is large, come from the tensor decomposition that is held in the continuous domain. Gains are therefore expected by taking into account the constellation knowledge. Such study is left as future work. However, it is important to highlight that, while the gap between FASURA and the achievability bound of [142] is large over all the range of considered K_a values, TBMC is 1.5 dB away from the achievability lower bound for $K_a < 20$. Finally, we observe that the gap between all the considered schemes and the achievability bound is growing with the number of active users, suggesting that there is still room for improvement in that regime.

Fading Robustness. We now assess the robustness to large-scale fading. The LSFCs are derived as

$$\gamma_k^{[\mathrm{dB}]} = \alpha^{[\mathrm{dB}]} - \beta \log_{10}(r_k) \tag{4.33}$$

where r_k is the distance between user k and the BS in meters, β is the path loss exponent, and $\alpha^{[\mathrm{dB}]}$ is an additive control term. According to Fig. 4.5, we consider the users to

be uniformly distributed in a disk of inner radius $r_{\min}$ and outer radius $r_{\max}$, thus r_k is distributed as $\mathcal{U}(r_{\min}, r_{\max})$. The parameter $\alpha^{[\mathrm{dB}]}$ is chosen so that the expected received power is equal to 0 dB, i.e. $\alpha^{[\mathrm{dB}]} = \beta\mathbb{E}[\log_{10}(r_k)]$. Both the path loss exponent and the minimum distance are chosen according to the non-line-of-sight UMi scenario [114] as $\beta = 35.3$ and $r_{\min} = 10$.

Fig. 4.7 depicts the minimum E_{b}/N_0 guaranteeing $P_{\mathrm{e}} \leq 0.1$ as a function of the cell radius, for $K_{\mathrm{a}} = 50$ active users and $M = 16$ antennas. The cell radius $r_{\max}$ takes values in the range $(r_{\min}, 167)$ m, where the upper bound of the interval is the cell radius of a typical UMi cell deployment with an inter-site distance of 250 m. Note that, the case $r_{\max} = r_{\min}$ corresponds to the scenario in Fig. 4.6 with $\gamma_k = 1$ for all k. Note also that, as the cell radius gets increased, the variance of the received power and therefore the probability of having a relevant fraction of active users exhibiting very poor channel characteristics becomes larger. We observe that TBMC is the most robust scheme with respect to the received power variance. Instead, despite achieving great performance for 50 users when the received power is equal for all users (see Fig 4.6), the FASURA scheme is shown to be more sensitive to the received power variance, especially for $20 \leq r_{\max} \leq 60$. This aspect, which should be further investigated, is most likely related to the energy detection phase, which is carried out as the first step at the decoder. Moreover, as shown in Fig 4.6, the pilot-based scheme achieves very poor performance for 50 users and $\gamma_k = 1$ for all k. For this reason, its results are not reported in Fig. 4.7.

4.7 Summary

In this chapter, we investigated TBM and TBMC for the URA use case. At first, the state-of-the-art URA solutions have been discussed, with a particular focus on the case of MIMO receivers. Then, we discussed an enhanced TBM design making use of powerful FEC. soft-decoding and SIC, and introducing the TBMC scheme. In TBMC, the users' payloads and the channel resources are split into two sub-blocks for unsourced and coherent signal transmissions, respectively. For the unsourced signals, TBM with state-of-the-art FEC coding is used to encode a fraction of the message. Then, a NOMA scheme is used for the coherent signal transmissions. At the receiver, soft decoding and SIC are adopted to mitigate the interference effects. We analyze the DoF achievable with both TBM and TBMC under different resource splitting policies and assessed the energy efficiency of such schemes. Numerical results show that with respect to TBM, the TBMC scheme achieves better energy efficiency, approaching the achievability bound for a moderate number of active users. Finally, in a comparison with state-of-the-art solutions, TBMC is shown to

be more robust to large-scale fading effects.

5 Conclusions

In this thesis, we have presented significant advancements in multiple access schemes for future wireless communication systems, in both the contexts of MTC and IRS-aided cellular networks.

After an introduction to OMA and NOMA approaches for both uplink and downlink transmissions, our exploration began with the introduction of PIMA, a novel semi-GF multiple access protocol designed for short packet transmissions in uplink OMA systems. We provided analytical solutions for scheduling optimality in the case of i.i.d. user activations, which were supported by the numerical results. Our theoretical analysis extended to correlated user activations, modeling PIMA as a PO-MDP, and optimizing the scheduling using the GFEO algorithm. The results demonstrated PIMA's superior performance in reducing latency and adapting to different traffic conditions, outperforming existing OMA solutions. Further, we delved into correlated packet generations, proposing a distributed learning-based scheduler. By modeling users in a Markov game of incomplete information and applying the LRI algorithm, we derived strategies leading to pure Nash equilibria. This approach significantly outperformed contemporary correlation-based OMA schemes in terms of throughput, especially under moderate traffic correlation and intensity.

Our focus then turned to a MIMO cellular network, exploring the integration of an IRS to counteract deep blockage issues. We developed an optimized TDMA scheduling strategy for downlink transmissions constrained by the IRS reconfiguration limits. Through innovative clustering-based scheduling policies, we successfully reduced reconfiguration needs while maximizing average sum capacity. Our findings showed that capacity-based clustering was superior, achieving notable efficiencies in reconfiguration and communi-

cation. Then, we examined OFDMA downlink scheduling in an IRS-assisted multi-user MIMO system. Facing again the challenge of limited IRS reconfigurations, we formulated the problem as a generalized multi-knapsack problem. Our heuristic approach for joint IRS configuration and resource allocation demonstrated remarkable effectiveness, nearly reaching the optimal sum rate achieved by a GA-based strategy.

Lastly, our investigation shifted to NOMA, and, in particular, to the URA framework. We presented TBM and TBMC in the context of URA, highlighting advancements in MIMO receivers. We introduced an enhanced TBM design incorporating state-of-the-art FEC, soft-decoding, and SIC. Then, we proposed TBMC, a hybrid approach leveraging both TBM and NOMA, which efficiently splits resources for unsourced and coherent signal transmissions. TBMC energy efficiency and robustness against large-scale fading effects marked a significant improvement over traditional TBM and other state-of-the-art URA solutions, approaching the theoretical bounds for moderate numbers of active users.

Future Research Directions. Future research should focus on several key areas to further advance the field of multiple access. Firstly, there is a crucial need for the exploration and development of advanced learning algorithms tailored to handle correlated user activations. As wireless networks become increasingly dense and interconnected, effectively managing the behavior of correlated user activations is pivotal. Sophisticated machine learning techniques, such as deep learning and reinforcement learning, could help to accurately predict and dynamically adjust the scheduling to correlated user patterns. These algorithms must be capable of adapting to both uplink OMA and NOMA systems, where the challenges of interference mitigation and resource allocation differ significantly. Secondly, the integration of NOMA scheduling in multi-user IRS-aided communication is a promising research direction. Particularly in dense urban environments or areas with challenging propagation conditions, leveraging NOMA alongside IRS can significantly enhance spectral efficiency and coverage. Investigating the optimal deployment strategies, beamforming techniques, and resource allocation algorithms in such scenarios is crucial for unlocking the full potential of NOMA-IRS synergy. Thirdly, other advances for the tensor-based approaches for URA should be discussed. In particular, the optimality of the resource and payload split in TBM as well as the adoption of code-domain NOMA for the coherent transmissions are still a subject of debate. Theoretical studies are needed to elucidate the trade-offs and performance bounds associated with these approaches. Additionally, ensuring the scalability of TBM and TBMC is essential to accommodate the diverse requirements of modern wireless networks. This entails addressing the challenges posed by a large number of devices, varying traffic patterns, and fluctuating payload sizes while maintaining efficiency and fairness. Finally, for all the aforementioned future

research directions at the physical layer, the interaction between physical and higher network layers protocols could lead to more integrated and efficient network operations. By jointly optimizing parameters across different layers, such as modulation schemes, resource allocation, and routing protocols, network performance can maximized while satisfying diverse quality-of-service requirements. This approach holds the potential to unlock new insights and innovations ensuring greater efficiency and reliability.

References

[1] Huawei Technologies Co., Ltd., "6G: The next horizon, from connected people and things to connected intelligence," *White Paper*, 2022.

[2] N. Benvenuto and M. Zorzi, *Principles of communications Networks and Systems*. John Wiley & Sons, 2011.

[3] S. Prasad, C. Shukla, and R. F. Chisab, "Performance analysis of OFDMA in LTE," in *Proc. ICCCNT*, 2012, pp. 1–7.

[4] N. Abu-Ali, A.-E. M. Taha, M. Salah, and H. Hassanein, "Uplink scheduling in LTE and LTE-advanced: Tutorial, survey and evaluation framework," *IEEE Commun. Surveys Tuts.*, vol. 16, no. 3, pp. 1239–1265, 2014.

[5] E. Bjornson, O. Ozdogan, and E. G. Larsson, "Intelligent reflecting surface versus decode-and-forward: How large surfaces are needed to beat relaying?" *IEEE Commun. Lett.*, vol. 9, no. 2, pp. 244–248, 2020.

[6] R. Flamini, D. De Donno, J. Gambini, F. Giuppi, C. Mazzucco, A. Milani, and L. Resteghini, "Towards a heterogeneous smart electromagnetic environment for millimeter-wave communications: An industrial viewpoint," *IEEE Trans. Antennas Propag.*, vol. 70, no. 10, pp. 8898–8910, 2022.

[7] N. Jiang, Y. Deng, and A. Nallanathan, "Traffic prediction and random access control optimization: Learning and non-learning-based approaches," *IEEE Commun. Mag.*, vol. 59, no. 3, pp. 16–22, 2021.

[8] 3GPP, "Study on RAN improvements for machine-type communications," 3rd Generation Partnership Project (3GPP), Technical Report (TR) 37.868, Oct. 2014, Version v.0.8.1.

[9] M. Laner, P. Svoboda, N. Nikaein, and M. Rupp, "Traffic models for machine type communications," in *Proc. ISWCS*, 2013, pp. 1–5.

[10] A. E. Kalør, O. A. Hanna, and P. Popovski, "Random access schemes in wireless systems with correlated user activity," in *Proc. IEEE SPAWC*, 2018, pp. 1–5.

[11] M. Shehab, A. K. Hagelskjar, A. E. Kalør, P. Popovski, and H. Alves, "Traffic prediction based fast uplink grant for massive IoT," in *Proc. IEEE PIMRC*, 2020, pp. 1–6.

[12] M. B. Shahab, R. Abbas, M. Shirvanimoghaddam, and S. J. Johnson, "Grant-free non-orthogonal multiple access for IoT: A survey," *IEEE Commun. Surveys Tuts.*, vol. 22, no. 3, pp. 1805–1838, 2020.

[13] Y. Saito, Y. Kishiyama, A. Benjebbour, T. Nakamura, A. Li, and K. Higuchi, "Non-orthogonal multiple access (NOMA) for cellular future radio access," in *Proc. IEEE VTC Spring*, 2013, pp. 1–5.

[14] H. Tabassum, M. S. Ali, E. Hossain, M. J. Hossain, and D. I. Kim, "Uplink vs. downlink NOMA in cellular networks: Challenges and research directions," in *Proc. IEEE VTC Spring*, 2017, pp. 1–7.

[15] L. Dai, B. Wang, Z. Ding, Z. Wang, S. Chen, and L. Hanzo, "A survey of non-orthogonal multiple access for 5G," *IEEE Commun. Surveys Tuts.*, vol. 20, no. 3, pp. 2294–2323, 2018.

[16] Y. Chen, A. Bayesteh, Y. Wu, B. Ren, S. Kang, S. Sun, Q. Xiong, C. Qian, B. Yu, Z. Ding, S. Wang, S. Han, X. Hou, H. Lin, R. Visoz, and R. Razavi, "Toward the standardization of non-orthogonal multiple access for next generation wireless networks," *IEEE Commun. Mag.*, vol. 56, no. 3, pp. 19–27, 2018.

[17] X. Meng, L. Zhang, C. Wang, L. Wang, Y. Wu, Y. Chen, and W. Wang, "Advanced NOMA receivers from a unified variational inference perspective," *IEEE J. Sel. Areas Commun.*, vol. 39, no. 4, pp. 934–948, 2021.

[18] Y. Polyanskiy, "A perspective on massive random-access," in *Proc. IEEE ISIT*, 2017, pp. 2523–2527.

[19] A. Fengler, S. Haghighatshoar, P. Jung, and G. Caire, "Non-bayesian activity detection, large-scale fading coefficient estimation, and unsourced random access with a massive MIMO receiver," *IEEE Trans. Inf. Theory*, vol. 67, no. 5, pp. 2925–2951, 2021.

[20] A. Decurninge, I. Land, and M. Guillaud, "Tensor-based modulation for unsourced massive random access," *IEEE Wireless Commun. Lett.*, vol. 10, no. 3, pp. 552–556, 2020.

[21] B. Clerckx, Y. Mao, R. Schober, E. A. Jorswieck, D. J. Love, J. Yuan, L. Hanzo, G. Y. Li, E. G. Larsson, and G. Caire, "Is NOMA efficient in multi-antenna networks? a critical look at next generation multiple access techniques," *IEEE Open J. Commun. Soc.*, vol. 2, pp. 1310–1343, 2021.

[22] A. Rech, S. Tomasin, L. Vangelista, and C. Costa, "Partial-information multiple access protocol for orthogonal transmissions," in *Proc. ICUFN*, 2023, pp. 271–276.

[23] A. Rech, S. Tomasin, L. Vangelista, and C. Costa, "Semi-grant-free orthogonal multiple access with partial-information for short packet transmissions," *IEEE Open J. Commun. Soc.*, pp. 1–1, 2023.

[24] A. Rech, S. Tomasin, L. Vangelista, and C. Costa, "Minimum-latency scheduling for partial-information multiple access schemes," in *Proc. IEEE GLOBECOM Wkshps*, 2023. arXiv: 2308.02286.

[25] A. Rech and S. Tomasin, "Coordinated random access for industrial IoT with correlated traffic by reinforcement-learning," in *Proc. IEEE GLOBECOM Wkshps*, 2021, pp. 1–6.

[26] A. Rech, M. Pagin, S. Tomasin, F. Moretto, L. Badia, M. Giordani, J. Gambini, and M. Zorzi, "Downlink TDMA scheduling for IRS-aided communications with block-static constraints," in *Proc. IEEE WCNC*, 2023, pp. 1–6.

[27] A. Rech, L. Badia, S. Tomasin, M. Pagin, M. Giordani, J. Gambini, and M. Zorzi, "Downlink clustering-based scheduling of IRS-assisted communications with reconfiguration constraints," *submitted to IEEE Trans. Wireless Commun.*, 2023. arXiv: 2305.14051.

[28] A. Rech, L. Badia, and S. Tomasin, "Scheduling for downlink OFDMA with IRS reconfiguration constraints," *submitted to IEEE Trans. Veh. Technol.*, 2024. arXiv: 2401.03062.

[29] A. Rech, A. Decurninge, and L. G. Ordóñez, "Unsourced random access with tensor-based and coherent modulations," in *Proc. IEEE PIMRC*, 2023, pp. 1–6.

[30] M. Centenaro, L. Vangelista, S. Saur, A. Weber, and V. Braun, "Comparison of collision-free and contention-based radio access protocols for the Internet of Things," *IEEE Trans. Commun.*, vol. 65, no. 9, pp. 3832–3846, 2017.

[31] S. Riolo, D. Panno, and L. Miuccio, "Modeling and analysis of tagged preamble transmissions in random access procedure for mMTC scenarios," *IEEE Trans. Commun.*, vol. 20, no. 7, pp. 4296–4312, 2021.

[32] P. Popovski, C. Stefanović, J. J. Nielsen, E. de Carvalho, M. Angjelichinoski, K. F. Trillingsgaard, and A.-S. Bana, "Wireless access in ultra-reliable low-latency communication," *IEEE Trans. Commun.*, vol. 67, no. 8, pp. 5783–5801, 2019.

[33] G. Wunder, P. Jung, and C. Wang, "Compressive random access for post-LTE systems," in *Proc. IEEE ICC Wkshps*, 2014, pp. 539–544.

[34] H. Seo, J.-P. Hong, and W. Choi, "Low latency random access for sporadic MTC devices in internet of things," *IEEE Internet Things J.*, vol. 6, no. 3, pp. 5108–5118, 2019.

[35] J. Choi, "On throughput of compressive random access for one short message delivery in IoT," *IEEE Internet Things J.*, vol. 7, no. 4, pp. 3499–3508, 2020.

[36] D. Donoho, "Compressed sensing," *IEEE Trans. Inf. Theory*, vol. 52, no. 4, pp. 1289–1306, 2006.

[37] S.-R. Lee, S.-D. Joo, and C.-W. Lee, "An enhanced dynamic framed slotted ALOHA algorithm for RFID tag identification," in *Proc. EAI MobiQuitous*, 2005, pp. 166–172.

[38] J. Su, Z. Sheng, D. Hong, and G. Wen, "An effective frame breaking policy for dynamic framed slotted ALOHA in RFID," *IEEE Commun. Lett.*, vol. 20, no. 4, pp. 692–695, 2016.

[39] J. Yu, P. Zhang, L. Chen, J. Liu, R. Zhang, K. Wang, and J. An, "Stabilizing frame slotted ALOHA-based IoT systems: A geometric ergodicity perspective," *IEEE J. Sel. Areas Commun.*, vol. 39, no. 3, pp. 714–725, 2021.

[40] Z. Ding, R. Schober, and H. V. Poor, "A new QoS-guarantee strategy for NOMA assisted semi-grant-free transmission," *IEEE Trans. Commun.*, vol. 69, no. 11, pp. 7489–7503, 2021.

[41] N. Jayanth, P. Chakraborty, M. Gupta, and S. Prakriya, "Performance of semi-grant free uplink with non-orthogonal multiple access," in *Proc. IEEE PIMRC*, 2020, pp. 1–6.

[42] J. Ding, M. Feng, M. Nemati, and J. Choi, "Performance analysis of massive MIMO assisted semi-grant-free random access," in *Proc. IEEE CCNC*, 2021, pp. 1–7.

[43] F. Moretto, A. Brighente, and S. Tomasin, "Greedy maximum throughput grant-free random access for correlated IoT traffic," in *Proc. IEEE VTC Fall*, 2021, pp. 1–5.

[44] A. Destounis, D. Tsilimantos, M. Debbah, and G. S. Paschos, "Learn2MAC: Online learning multiple access for URLLC applications," in *Proc. IEEE INFOCOM Wkshps*, 2019, pp. 1–6.

[45] M. Goldenbaum and S. Stanczak, "Robust analog function computation via wireless multiple-access channels," *IEEE Trans. Commun.*, vol. 61, no. 9, pp. 3863–3877, 2013.

[46] W. Liu, X. Zang, Y. Li, and B. Vucetic, "Over-the-air computation systems: Optimization, analysis and scaling laws," *IEEE Trans. Wireless Commun.*, vol. 19, no. 8, pp. 5488–5502, 2020.

[47] G. Zhu, J. Xu, K. Huang, and S. Cui, "Over-the-air computing for wireless data aggregation in massive IoT," *IEEE Wireless Commun.*, vol. 28, no. 4, pp. 57–65, 2021.

[48] A. Munari, "On the value of retransmissions for age of information in random access networks without feedback," in *Proc. IEEE GLOBECOM*, 2022, pp. 4964–4970.

[49] J. F. Paris and A. J. Goldsmith, "Adaptive modulation for MIMO multiplexing under average ber constraints and imperfect CSI," in *Proc. IEEE ICC*, vol. 3, 2006, pp. 1318–1325.

[50] Y. Li and Q. He, "On the ratio of two correlated complex Gaussian random variables," *IEEE Commun. Lett.*, vol. 23, no. 12, pp. 2172–2176, 2019.

[51] S. Wu, "Moments of complex Gaussian ratios," *IEEE Commun. Lett.*, vol. 23, no. 1, pp. 88–91, 2019.

[52] L. P. Kaelbling, M. L. Littman, and A. R. Cassandra, "Planning and acting in partially observable stochastic domains," *Artificial Intelligence*, vol. 101, no. 1, pp. 99–134, 1998.

[53] M. L. Littman, "A tutorial on partially observable markov decision processes," *J. Math. Psychology*, vol. 53, no. 3, pp. 119–125, 2009, Special Issue: Dynamic Decision Making.

[54] L. Rabiner and B. Juang, "An introduction to hidden markov models," *IEEE ASSP Mag.*, vol. 3, no. 1, pp. 4–16, 1986.

[55] B. Alt, M. Schultheis, and H. Koeppl, "POMDPs in continuous time and discrete spaces," in *Advances in Neural Inf. Process. Syst.*, H. Larochelle, M. Ranzato, R. Hadsell, M. Balcan, and H. Lin, Eds., vol. 33, Curran Associates, Inc., 2020, pp. 13 151–13 162.

[56] D. Bertsekas and R. Gallager, *Data networks*. Athena Scientific, 2021.

[57] R. Rivest, "Network control by bayesian broadcast," *IEEE Trans. Inf. Theory*, vol. 33, no. 3, pp. 323–328, 1987.

[58] Y. Jin and T.-J. Lee, "Throughput analysis of NOMA-ALOHA," *IEEE Trans. Mobile Comput.*, vol. 21, no. 4, pp. 1463–1475, 2022.

[59] J. Choi, "Stability and throughput of random access with CS-based MUD for MTC," *IEEE Trans. Veh. Technol.*, vol. 67, no. 3, pp. 2607–2616, 2018.

[60] S. Semper, F. Römer, T. Hotz, and G. DelGaldo, "Sparsity order estimation from a single compressed observation vector," *IEEE Trans. Signal Process.*, vol. 66, no. 15, pp. 3958–3971, 2018.

[61] 3GPP, *Physical channels and modulation*, Technical Report (TR), Version 16.2.0, 2020.

[62] M. L. Littman, "Markov games as a framework for multi-agent reinforcement learning," in *Machine Learning Proc.* W. W. Cohen and H. Hirsh, Eds., San Francisco (CA): Morgan Kaufmann, 1994, pp. 157–163.

[63] I. J. Shapiro and K. S. Narendra, "Use of stochastic automata for parameter self optimization with multimodal performance criteria," *IEEE Trans. Syst. Sci. Cybern.*, vol. 5, no. 4, pp. 352–360, 1969.

[64] P. S. Sastry, V. V. Phansalkar, and M. A. L. Thathachar, "Decentralized learning of Nash equilibria in multi-person stochastic games with incomplete information," *IEEE Trans. Syst., Man, Cybern.*, vol. 24, no. 5, pp. 769–777, 1994.

[65] S. Tadelis, *Game theory: an introduction*. Princeton university press, 2013.

[66] 3GPP, *5G; NR; base station (BS) radio transmission and reception*, TS 38.104 (Rel. 16), 2022.

[67] F. Tariq, M. R. Khandaker, K.-K. Wong, M. A. Imran, M. Bennis, and M. Debbah, "A speculative study on 6G," *IEEE Wireless Commun.*, vol. 27, no. 4, pp. 118–125, 2020.

[68] S. Rangan, T. S. Rappaport, and E. Erkip, "Millimeter-wave cellular wireless networks: Potentials and challenges," *Proc. IEEE*, vol. 102, no. 3, pp. 366–385, 2014.

[69] P. Di Francesco, J. Kibiłda, F. Malandrino, N. J. Kaminski, and L. A. DaSilva, "Sensitivity analysis on service-driven network planning," *IEEE/ACM Trans. Netw.*, vol. 25, no. 3, pp. 1417–1430, 2017.

[70] E. J. Oughton, N. Comini, V. Foster, and J. W. Hall, "Policy choices can help keep 4G and 5G universal broadband affordable," *Techn. Forecasting Soc. Change*, vol. 176, p. 121 409, 2022.

[71] A. Chaoub, M. Giordani, B. Lall, V. Bhatia, A. Kliks, L. Mendes, K. Rabie, H. Saarnisaari, A. Singhal, N. Zhang, *et al.*, "6G for bridging the digital divide: Wireless connectivity to remote areas," *IEEE Wireless Commun.*, vol. 29, no. 1, pp. 160–168, 2021.

[72] D. López-Pérez, M. Ding, H. Claussen, and A. H. Jafari, "Towards 1 Gbps/UE in cellular systems: Understanding ultra-dense small cell deployments," *IEEE Commun. Surveys Tuts.*, vol. 17, no. 4, pp. 2078–2101, 2015.

[73] 3GPP, *5G; NR; integrated access and backhaul (IAB) radio transmission and reception*, TS 38.174 (Rel. 17), 2022.

[74] M. Polese, M. Giordani, T. Zugno, A. Roy, S. Goyal, D. Castor, and M. Zorzi, "Integrated access and backhaul in 5G mmWave networks: Potential and challenges," *IEEE Commun. Mag.*, vol. 58, no. 3, pp. 62–68, 2020.

[75] Y. Yang, S. Zhang, and R. Zhang, "IRS-enhanced OFDMA: Joint resource allocation and passive beamforming optimization," *IEEE Wireless Commun. Lett.*, vol. 9, no. 6, pp. 760–764, 2020.

[76] J. Lee, J. Choi, and J. Kang, "Harmony search-based optimization for multi-RISs MU-MISO OFDMA systems," *IEEE Wireless Commun. Lett.*, vol. 12, no. 2, pp. 257–261, 2023.

[77] Y. Guo, Z. Qin, Y. Liu, and N. Al-Dhahir, "Intelligent reflecting surface aided multiple access over fading channels," *IEEE Trans. Commun.*, vol. 69, no. 3, pp. 2015–2027, 2021.

[78] D. Zhang, Q. Wu, M. Cui, G. Zhang, and D. Niyato, "Throughput maximization for IRS-assisted wireless powered hybrid NOMA and TDMA," *IEEE Wireless Commun. Lett.*, vol. 10, no. 9, pp. 1944–1948, 2021.

[79] H. Al-Obiedollah, H. A. B. Salameh, K. Cumanan, Z. Ding, and O. A. Dobre, "Self-sustainable multi-IRS-aided wireless powered hybrid TDMA-NOMA system," *IEEE Access*, vol. 11, pp. 57 428–57 436, 2023.

[80] Z. Zhang, T. Jiang, and W. Yu, "Learning based user scheduling in reconfigurable intelligent surface assisted multiuser downlink," *IEEE J. Sel. Topics Signal Process.*, vol. 16, no. 5, pp. 1026–1039, 2022.

[81] A. Bansal, K. Singh, B. Clerckx, C.-P. Li, and M.-S. Alouini, "Rate-splitting multiple access for intelligent reflecting surface aided multi-user communications," *IEEE Trans. Veh. Technol.*, vol. 70, no. 9, pp. 9217–9229, 2021.

[82] H. Fu, S. Feng, and D. W. Kwan Ng, "Resource allocation design for IRS-aided downlink MU-MISO RSMA systems," in *Proc. ICC Wkshps*, 2021.

[83] B. Zhuo, J. Gu, W. Duan, X. Gu, G. Zhang, M. Wen, and P.-H. Ho, "Partial non-orthogonal multiple access: A new perspective for RIS-aided downlink," *IEEE Wireless Commun. Lett.*, vol. 11, no. 11, pp. 2395–2399, 2022.

[84] S. Hu, Z. Wei, Y. Cai, C. Liu, D. W. K. Ng, and J. Yuan, "Robust and secure sum-rate maximization for multiuser MISO downlink systems with self-sustainable IRS," *IEEE Trans. Commun.*, vol. 69, no. 10, pp. 7032–7049, 2021.

[85] Q. Wu and R. Zhang, "Towards smart and reconfigurable environment: Intelligent reflecting surface aided wireless network," *IEEE Commun. Mag.*, vol. 58, no. 1, pp. 106–112, 2020.

[86] S. Abeywickrama, R. Zhang, Q. Wu, and C. Yuen, "Intelligent reflecting surface: Practical phase shift model and beamforming optimization," *IEEE Trans. Commun.*, vol. 68, no. 9, pp. 5849–5863, 2020.

[87] Q. Wu and R. Zhang, "Intelligent reflecting surface enhanced wireless network via joint active and passive beamforming," *IEEE Trans. Wireless Commun.*, vol. 18, no. 11, pp. 5394–5409, 2019.

[88] R. Liu, Q. Wu, M. Di Renzo, and Y. Yuan, "A path to smart radio environments: An industrial viewpoint on reconfigurable intelligent surfaces," *IEEE Wireless Commun.*, vol. 29, no. 1, pp. 202–208, 2022.

[89] C. Liaskos, S. Nie, A. Tsioliaridou, A. Pitsillides, S. Ioannidis, and I. Akyildiz, "Realizing wireless communication through software-defined hypersurface environments," in *Proc. IEEE WoWMoM*, 2018.

[90] X. Mu, Y. Liu, L. Guo, J. Lin, and N. Al-Dhahir, "Capacity and optimal resource allocation for IRS-assisted multi-user communication systems," *IEEE Trans. Commun.*, vol. 69, no. 6, pp. 3771–3786, 2021.

[91] ETSI, *Reconfigurable Intelligent Surfaces (RIS); Communication Models, Channel Models, Channel Estimation and Evaluation Methodology*, ETSI GR RIS 003 V1.1.1, 2023.

[92] M. Rossanese, P. Mursia, A. Garcia-Saavedra, V. Sciancalepore, A. Asadi, and X. Costa-Perez, "Designing, building, and characterizing RF switch-based Reconfigurable Intelligent Surfaces," in *Proc. ACM WiNTECH*, Sydney, NSW, Australia, 2022.

[93] G. C. Alexandropoulos, D.-T. Phan-Huy, K. D. Katsanos, M. Crozzoli, H. Wymeersch, P. Popovski, P. Ratajczak, Y. Bénédic, M.-H. Hamon, S. H. Gonzalez, *et al.*, "RIS-enabled smart wireless environments: Deployment scenarios, network architecture, bandwidth and area of influence," *EURASIP J. Wireless Commun. Netw.*, vol. 2023, no. 1, p. 103, 2023.

[94] L. Yezhen, R. Yongli, Y. Fan, X. Shenheng, and Z. Jiannian, "A novel 28 ghz phased array antenna for 5G mobile communications," *ZTE Commun.*, vol. 18, no. 3, pp. 20–25, 2020.

[95] V. Jamali, G. C. Alexandropoulos, R. Schober, and H. V. Poor, "Low-to-zero-overhead IRS reconfiguration: Decoupling illumination and channel estimation," *IEEE Commun. Lett.*, vol. 26, no. 4, pp. 932–936, 2022.

[96] Q.-U.-A. Nadeem, A. Kammoun, A. Chaaban, M. Debbah, and M.-S. Alouini, "Asymptotic max-min SINR analysis of reconfigurable intelligent surface assisted MISO systems," *IEEE Trans. Wireless Commun.*, vol. 19, no. 12, pp. 7748–7764, 2020.

[97] X. Qian, M. Di Renzo, V. Sciancalepore, and X. Costa-Pérez, "Joint optimization of reconfigurable intelligent surfaces and dynamic metasurface antennas for massive MIMO communications," in *Proc. IEEE SAM*, 2022.

[98] Y. Lu, M. Koivisto, J. Talvitie, M. Valkama, and E. S. Lohan, "Positioning-aided 3D beamforming for enhanced communications in mmwave mobile networks," *IEEE Access*, vol. 8, pp. 55 513–55 525, 2020.

[99] X. Tan, Z. Sun, D. Koutsonikolas, and J. M. Jornet, "Enabling indoor mobile millimeter-wave networks based on smart reflect-arrays," in *Proc. IEEE INFOCOM*, 2018.

[100] 3GPP, *5G; NR; physical layer procedures for data*, TS 38.214 (Rel. 16), 2020.

[101] Z.-Q. He and X. Yuan, "Cascaded channel estimation for large intelligent metasurface assisted massive MIMO," *IEEE Commun. Lett.*, vol. 9, no. 2, pp. 210–214, 2020.

[102] J. Rains, anvar tukmanov, Q. H. Abbasi, and M. Imran, "RIS-enhanced MIMO channels in urban environments: Experimental insights," *techrxiv preprint techrxiv.24558475.v1*, 2023.

[103] T. S. Rappaport, S. Sun, and M. Shafi, "Investigation and comparison of 3GPP and NYUSIM channel models for 5G wireless communications," in *Proc. IEEE VTC Fall*, 2017, pp. 1–5.

[104] L. Anchora, L. Badia, E. Karipidis, and M. Zorzi, "Capacity gains due to orthogonal spectrum sharing in multi-operator LTE cellular networks," in *Proc. IEEE ISWCS*, 2012.

[105] A. L. Swindlehurst, G. Zhou, R. Liu, C. Pan, and M. Li, "Channel estimation with reconfigurable intelligent surfaces—a general framework," *Proc. IEEE*, vol. 110, no. 9, pp. 1312–1338, 2022.

[106] P. Zeng, D. Qiao, H. Qian, and Q. Wu, "Joint beamforming design for IRS aided multiuser MIMO with imperfect CSI," *IEEE Trans. Veh. Technol.*, vol. 71, no. 10, pp. 10 729–10 743, 2022.

[107] L. Rokach and O. Maimon, "Clustering methods," in *Data mining and knowledge discovery handbook*, Springer, 2005, pp. 321–352.

[108] S. Lloyd, "Least squares quantization in PCM," *IEEE Trans. Inf. Theory*, vol. 28, no. 2, pp. 129–137, 1982.

[109] F. Murtagh and P. Contreras, "Algorithms for hierarchical clustering: An overview," *Wiley Interdisciplinary Rev.: Data Mining Knowl. Discovery*, vol. 2, no. 1, pp. 86–97, 2012.

[110] L. Kaufman and P. J. Rousseeuw, "Clustering by means of medoids," in *Rep. Fac. Math. Inf.*, vol. 87, 1987.

[111] M. Van der Laan, K. Pollard, and J. Bryan, "A new partitioning around medoids algorithm," *J. Stat. Computat. Simul.*, vol. 73, no. 8, pp. 575–584, 2003.

[112] M. Sabin and R. Gray, "Global convergence and empirical consistency of the generalized Lloyd algorithm," *IEEE Trans. Inf. Theory*, vol. 32, no. 2, pp. 148–155, Feb. 1986.

[113] D. Xu and Y. Tian, "A comprehensive survey of clustering algorithms," *Annals of Data Science*, vol. 2, pp. 165–193, 2015.

[114] 3GPP, *Study on channel model for frequencies from 0.5 to 100 GHz*, Technical Report (TR), Version 16.1.0, 2020.

[115] T. Zugno, M. Polese, N. Patriciello, B. Bojović, S. Lagen, and M. Zorzi, "Implementation of a spatial channel model for ns-3," in *Proc. ACM WNS3*, 2020.

[116] M. Pagin, M. Giordani, A. A. Gargari, A. Rech, F. Moretto, S. Tomasin, J. Gambini, and M. Zorzi, "End-to-end simulation of 5G networks assisted by IRS and AF relays," in *Proc. MedComNet*, 2022, pp. 150–157.

[117] M. Rivera, M. Chegini, W. Jaafar, S. Alfattani, and H. Yanikomeroglu, "Optimization of quantized phase shifts for reconfigurable smart surfaces assisted communications," in *Proc. IEEE CCNC*, 2022.

[118] J. H. Holland, "Genetic algorithms," *Scientific american*, vol. 267, no. 1, pp. 66–73, 1992.

[119] A. Decurninge, I. Land, and M. Guillaud, "Tensor-based modulation for unsourced massive random access," *IEEE Wireless Commun. Lett.*, vol. 10, no. 3, pp. 552–556, 2021.

[120] J. Che, Z. Zhang, Z. Yang, X. Chen, and C. Zhong, "Massive unsourced random access for NGMA: Architectures, opportunities, and challenges," *IEEE Network*, vol. 37, no. 1, pp. 28–35, 2023.

[121] Y. Polyanskiy, H. V. Poor, and S. Verdu, "Channel coding rate in the finite blocklength regime," *IEEE Trans. Inf. Theory*, vol. 56, no. 5, pp. 2307–2359, 2010.

[122] S. J. Nawaz, S. K. Sharma, B. Mansoor, M. N. Patwary, and N. M. Khan, "Non-coherent and backscatter communications: Enabling ultra-massive connectivity in 6G wireless networks," *IEEE Access*, vol. 9, pp. 38 144–38 186, 2021.

[123] V. K. Amalladinne, J.-F. Chamberland, and K. R. Narayanan, "A Coded Compressed Sensing Scheme for Unsourced Multiple Access," *IEEE Trans. Inf. Theory*, vol. 66, no. 10, pp. 6509–6533, 2020.

[124] V. K. Amalladinne, A. K. Pradhan, C. Rush, J.-F. Chamberland, and K. R. Narayanan, "Unsourced random access with coded compressed sensing: Integrating amp and belief propagation," *IEEE Trans. Inf. Theory*, vol. 68, no. 4, pp. 2384–2409, 2022.

[125] A. Fengler, P. Jung, and G. Caire, "SPARCs for unsourced random access," *IEEE Trans. Inf. Theory*, vol. 67, no. 10, pp. 6894–6915, 2021.

[126] V. Shyianov, F. Bellili, A. Mezghani, and E. Hossain, "Massive unsourced random access based on uncoupled compressive sensing: Another blessing of massive MIMO," *IEEE J. Sel. Areas Commun.*, vol. 39, no. 3, pp. 820–834, 2021.

[127] L. Liu and W. Yu, "Massive connectivity with massive MIMO—part I: Device activity detection and channel estimation," *IEEE Trans. Signal Process.*, vol. 66, no. 11, pp. 2933–2946, 2018.

[128] Z. Chen, F. Sohrabi, and W. Yu, "Sparse activity detection for massive connectivity," *IEEE Trans. Signal Process.*, vol. 66, no. 7, pp. 1890–1904, 2018.

[129] J.-C. Jiang and H.-M. Wang, "Massive random access with sporadic short packets: Joint active user detection and channel estimation via sequential message passing," *IEEE Trans. Wireless Commun.*, vol. 20, no. 7, pp. 4541–4555, 2021.

[130] A. Fengler, P. Jung, and G. Caire, "Pilot-based unsourced random access with a massive MIMO receiver in the quasi-static fading regime," in *Proc. IEEE SPAWC*, 2021, pp. 356–360.

[131] M. Gkagkos, K. R. Narayanan, J.-F. Chamberland, and C. N. Georghiades, "FASURA: A scheme for quasi-static massive MIMO unsourced random access channels," in *Proc. IEEE SPAWC*, 2022, pp. 1–5.

[132] K.-H. Ngo, A. Lancho, G. Durisi, and A. Graell i Amat, "Unsourced multiple access with random user activity," *IEEE Trans. Inf. Theory*, vol. 69, no. 7, pp. 4537–4558, 2023.

[133] W. Wang, J. You, S. Liang, W. Han, and B. Bai, "Slotted concatenated coding scheme for asynchronous uplink unsourced random access with a massive MIMO receiver," in *Proc. IEEE PIMRC*, 2022, pp. 246–252.

[134] T. Li, Y. Wu, W. Zhang, X.-G. Xia, and C. Xiao, "A graph-based collision resolution scheme for asynchronous unsourced random access," *arXiv preprint arXiv:2305.13753*, 2023.

[135] P. Comon, "Tensors : A brief introduction," *IEEE Signal Process. Mag.*, vol. 31, no. 3, pp. 44–53, 2014.

[136] T. G. Kolda and B. W. Bader, "Tensor decompositions and applications," *SIAM review*, vol. 51, no. 3, pp. 455–500, 2009.

[137] L. Chiantini, G. Ottaviani, and N. Vannieuwenhoven, "An algorithm for generic and low-rank specific identifiability of complex tensors," *SIAM J. Matrix Anal. Appl.*, vol. 35, no. 4, pp. 1265–1287, 2014.

[138] L. Zheng and D. Tse, "Communication on the grassmann manifold: A geometric approach to the noncoherent multiple-antenna channel," *IEEE Trans. Inf. Theory*, vol. 48, no. 2, pp. 359–383, 2002.

[139] K.-H. Ngo, A. Decurninge, M. Guillaud, and S. Yang, "Cube-split: A structured grassmannian constellation for non-coherent SIMO communications," *IEEE Trans. Wireless Commun.*, vol. 19, no. 3, pp. 1948–1964, 2020.

[140] A. Decurninge, I. Land, and M. Guillaud, "Tensor decomposition bounds for TBM-based massive access," in *Proc. IEEE SPAWC*, 2021, pp. 346–350.

[141] V. Bioglio, C. Condo, and I. Land, "Design of polar codes in 5G new radio," *IEEE Commun. Surveys Tuts.*, vol. 23, no. 1, pp. 29–40, 2021.

[142] J. Gao, Y. Wu, T. Li, and W. Zhang, "Energy efficiency of MIMO massive unsourced random access with finite blocklength," *IEEE Wireless Commun. Lett.*, pp. 1–1, 2023.

[143] L. Sorber, M. Van Barel, and L. De Lathauwer, "Optimization-based algorithms for tensor decompositions: Canonical polyadic decomposition, decomposition in rank-$(L_r, L_r, 1)$ terms, and a new generalization," *SIAM J. Optim.*, vol. 23, no. 2, pp. 695–720, 2013.

List of publications

Journals

[23] A. Rech, S. Tomasin, L. Vangelista, and C. Costa, "Semi-grant-free orthogonal multiple access with partial-information for short packet transmissions," *IEEE Open J. Commun. Soc.*, pp. 1–1, 2023.

[144] L. Stefanini, A. Rech, D. Ramaccia, S. Tomasin, A. Toscano, F. Moretto, and F. Bilotti, "Multibeam scanning antenna system based on beamforming metasurface for fast 5G NR initial access," *IEEE Access*, vol. 10, pp. 65 982–65 995, 2022.

Conferences

[22] A. Rech, S. Tomasin, L. Vangelista, and C. Costa, "Partial-information multiple access protocol for orthogonal transmissions," in *Proc. ICUFN*, 2023, pp. 271–276.

[24] A. Rech, S. Tomasin, L. Vangelista, and C. Costa, "Minimum-latency scheduling for partial-information multiple access schemes," in *Proc. IEEE GLOBECOM Wkshps*, 2023. arXiv: 2308.02286.

[25] A. Rech and S. Tomasin, "Coordinated random access for industrial IoT with correlated traffic by reinforcement-learning," in *Proc. IEEE GLOBECOM Wkshps*, 2021, pp. 1–6.

[26] A. Rech, M. Pagin, S. Tomasin, F. Moretto, L. Badia, M. Giordani, J. Gambini, and M. Zorzi, "Downlink TDMA scheduling for IRS-aided communications with block-static constraints," in *Proc. IEEE WCNC*, 2023, pp. 1–6.

[29] A. Rech, A. Decurninge, and L. G. Ordóñez, "Unsourced random access with tensor-based and coherent modulations," in *Proc. IEEE PIMRC*, 2023, pp. 1–6.

[116] M. Pagin, M. Giordani, A. A. Gargari, A. Rech, F. Moretto, S. Tomasin, J. Gambini, and M. Zorzi, "End-to-end simulation of 5G networks assisted by IRS and AF relays," in *Proc. MedComNet*, 2022, pp. 150–157.

[145] A. Rech, F. Moretto, and S. Tomasin, "Maximum-rate optimization of hybrid intelligent reflective surface and relay systems," in *Proc. IEEE SPAWC*, 2021, pp. 516–520.

[146] L. Stefanini, A. Rech, D. Ramaccia, S. Tomasin, F. Moretto, A. Toscano, and F. Bilotti, "Beamforming metasurface for antenna systems in 5G/6G environments," in *Proc. EuCAP*, 2023, pp. 1–4.

Preprints

[27] A. Rech, L. Badia, S. Tomasin, M. Pagin, M. Giordani, J. Gambini, and M. Zorzi, "Downlink clustering-based scheduling of IRS-assisted communications with reconfiguration constraints," *submitted to IEEE Trans. Wireless Commun.*, 2023. arXiv: 2305.14051.

[28] A. Rech, L. Badia, and S. Tomasin, "Scheduling for downlink OFDMA with IRS reconfiguration constraints," *submitted to IEEE Trans. Veh. Technol.*, 2024. arXiv: 2401.03062.

Paper [22] won the **Best Paper Award**.
Paper [26] won the **Best Workshop Paper Award**.